CHARACTERIZATION AND QUANTIFICATION OF BIOLOGICAL SURFACES USING CLUSTER TOF-SIMS WITH THE EVENT-BY-EVENT BOMBARDMENT/DETECTION MODE

A Dissertation

by

LI-JUNG CHEN

Submitted to the Office of Graduate Studies of
Texas A&M University
in partial fulfillment of the requirements for the degree of

DOCTOR OF PHILOSOPHY

May 2012

Major Subject: Chemistry

CHARACTERIZATION AND QUANTIFICATION OF BIOLOGICAL SURFACES

USING CLUSTER TOF-SIMS WITH THE EVENT-BY-EVENT

BOMBARDMENT/DETECTION MODE

Copyright 2012 Li-Jung Chen

CHARACTERIZATION AND QUANTIFICATION OF BIOLOGICAL SURFACES USING CLUSTER TOF-SIMS WITH THE EVENT-BY-EVENT BOMBARDMENT/DETECTION MODE

A Dissertation

by

LI-JUNG CHEN

Submitted to the Office of Graduate Studies of
Texas A&M University
in partial fulfillment of the requirements for the degree of

DOCTOR OF PHILOSOPHY

Approved by:

Chair of Committee,	Emile A. Schweikert
Committee Members,	James D. Batteas
	Robert C. Burghardt
	Gyula Vigh
Head of Department,	David H. Russell

May 2012

Major Subject: Chemistry

ABSTRACT

Characterization and Quantification of Biological Surfaces Using Cluster ToF-SIMS with the Event-By-Event Bombardment/Detection Mode. (May 2012)

Li-Jung Chen, B.S., National Chiao Tung University (Taiwan, Hsinchu)

M.S., National Tsing Hua University (Taiwan, Hsinchu)

Chair of Advisory Committee: Dr. Emile A. Schweikert

Cluster ToF-SIMS (time-of-flight secondary ion mass spectrometry) operated in the event-by-event bombardment/detection mode has been applied to: 1) evaluate and screen the manufacturing quality of step-wise prepared micropatterned biointerfaces; 2) quantify the binding density of Au nanoparticles (AuNPs)-antiCD4 conjugates selectively attached on the cell surface; 3) elucidate the biological interaction of proteins and molecules by quantifying the fractional coverage of immobilized biomolecules; 4) enhance the accuracy of secondary ion identification of specific molecules.

Briefly, our method consists of recording the secondary ions, SIs, individually emitted from a single projectile impact ($C_{60}^{1,2+}$, Au_{400}^{+4}). From the set of individual mass data, we select events where a specific SI was detected. The selected records reveal the SIs co-ejected from the nanovolume impacted by an individual cluster projectile from an emission area of 10-20 nm in diameter and an emission depth of 5-10 nm.

The approach for quantifying the number of AuNPs or that of specific nanodomains is via the concept of the fractional coverage. The latter is the ratio of the effective number of projectile impacts on a specified sampling area (N_e) to the total number of impacts (N_0). The methodology has been validated with the determination of the number of antibody-AuNP conjugates on a cell, i.e. the number of disease related antigens on a cell via their specific binding sites with the AuNP-labeled antibodies. The number of AuNP-antibodies measured, ~42000 per cell, is in good agreement with literature results.

The fractional coverage concept was also used to quantify several variants of biointerfaces. An example is the quantification of biotin and avidin immobilization as a function of the composition of silane substrates. The data collected in the event-by-event bombardment/detection mode expands the scope and quality of analytical information. One can identify SIs co-emitted with two specified SIs (double coincidence mass spectrometry) to inspect a specific stratum of a biointerface.

A further refinement is the selection of events meeting a double coincidence emission condition. This mode enables the identification of nano-object of a few nm in size, which eliminates (anticoincidence) interferences from substrates.

DEDICATION

To

my beloved family,

dad, mom, and grandma,

the Chen's and Chang's,

most of all,

to Chi-Yuan and Alvin.

ACKNOWLEDGEMENTS

I would like to take this opportunity to express my sincere gratitude to the Schweikert research group for their help over these years. Also, I would like to thank my committee members, Dr. Batteas, Dr. Burghardt, and Dr. Vigh for their advices.

In particular, the sincerest thank to my advisor, Dr. Schweikert, whose enthusiasm toward science always inspires me to move forward. His advice, guidance, patience, encouragement, and extensive knowledge are decisive to finish this work. Special thanks also go to Dr. Verkhoturov, whose enthusiastic and energetic attitude toward research always stimulate my brain cells. I am grateful to work with him and appreciate his advice, passion, and intuitive insightfulness to the nature of a work. I would like to extend my gratitude to the Revzin's research group in UC Davis: Dr. Revzin, Sunny, and Dr. Seo, for their expertise in preparing biological samples and constructive contributions to this study, I am thankful to have a great experience to collaborate with them.

Also, I owe my sincere thanks to all staffs in the center for chemical characterization and analysis: Dr. James, Dr. Raulerson, and Ms. Melton, for their help and support.

Thanks also go to my friends, colleagues and those I have encountered in my career, especially: Zhen, Veronica, Marcus, Francisco, Michael, Daniel, Chao-Kai, Fan, and Aaron who are always helpful in many ways.

I would like to thank the grants for supporting this research: the National Science Foundation grant to EAS and the National Institutes of Health grant to Revzin.

The deepest gratitude to my beloved family: my grandmother, my parents, my sisters and brother, my husband, and my lovely son for providing unconditional love, support, and encouragement to help me through the intertwined paths of graduate study and motherhood.

TABLE OF CONTENTS

Page

ABSTRACT iii

DEDICATION v

ACKNOWLEDGEMENTS vi

TABLE OF CONTENTS viii

LIST OF FIGURES x

LIST OF TABLES xiii

CHAPTER

I INTRODUCTION 1

Static SIMS 4
Cluster Primary Ions 5
Coincidence Measurements in Secondary Ion Mass Spectrometry 7
Current Quantitative Analysis of Biological Surfaces 9
Present Study 11

II INSTRUMENTATION AND METHODOLOGY 12

C_{60} Effusion Source Mass Spectrometer 12
Au Liquid Metal Ion Source Mass Spectrometer 15
Wien Filter 17
Time of Flight Mass Analyzer 18
Detectors and Detection Electronics 20
Signal Processing 26
Event-by-Event Bombardment Detection Mode 27
Correlation Coefficient 30
Quantitative Methodology 31
Double Coincidence Mass Spectrometry 35

CHAPTER Page

III CHARACTERIZATION AND QUANTIFICATION OF BIOLOGICAL MICROPATTERNS USING CLUSTER SIMS 37

Introduction 37
Experimental Section 38
Results and Discussion 41
Conclusion 56

IV CHARACTERIZATION AND QUANTIFICATION OF NANOPARTICLE-ANTIBODY CONJUGATES ON CELLS USING C60 TOF SIMS IN THE EVENT-BY-EVENT BOMBARDMENT/DETECTION MODE 59

Introduction 59
Experimental Section 61
Results and Discussion 63
Conclusion 74

V QUANTITATIVE LABEL-FREE CHARACTERIZATION OF AVIDIN-BIOTIN ASSEMBLIES ON SILANIZED GLASS 76

Introduction 76
Experimental Section 78
Results and Discussion 80
Conclusion 94

VI CONCLUSIONS 97

REFERENCES 100

APPENDIX 106

VITA 118

LIST OF FIGURES

FIGURE		Page
I-1	Comparison of spatial resolutions and sensitivities for various analytical techniques	2
I-2	Comparison of sampling or profiling depths of various analytical techniques	3
II-1	Schematic diagram of the C_{60} SIMS instrument	21
II-2	Schematic illustration of the C_{60} effusion source and the copper reservoir	22
II-3	Schematic illustration of the Au-LMIS ToF-mass spectrometer	23
II-4	Schematic diagram of time of flight mass analyzer in C_{60} instrument	24
II-5	Schematic diagram of C_{60} mass spectrometer: (a) start and (b) stop detector	25
II-6	Schematic illustration of coincidental ion mass spectrum	29
II-7	Schematic illustration of the coincidental ion mass spectrum and double coincidental ion mass spectrum constructed with SIs co-emitted with selected ions originating from specified layers	36
III-1	Schematic illustration of the fabrication of protein attached micropatterns	39
III-2	Schematic illustration of the fabrication processes for samples 1-6	45
III-3	The comparison flows of fabricating collagen micropatterns	46
III-4	The negative ion mass spectra of before and after O_2 plasma treatment to remove PEG silane	47
III-5	The optical microscopic image of ITO patches and PR micropattern	48
III-6	The negative ion mass spectra of sample 5 and 6	49

FIGURE Page

III-7 The negative ion mass spectrum of sample 7 50

III-8 The negative ion mass spectrum of sample 9 50

III-9 The negative ion mass spectrum of sample 10 52

III-10 The coincidence ion mass spectrum of sample 10 with selected ion CNO^- 53

III-11 The schematic illustration of single C_{60}^+ projectile impact on the interfacial area between ^{15}N-Glycien/PBS and PR residues 53

III-12 The negative ion mass spectra of ^{15}N-glycien/PBS deposited on 100 μm diameter circle patterned surface bombarded with C_{60}^+ 54

IV-1 Secondary ion mass spectrum of AuNPs-antiCD4 on Molt-3 cell micropatterned surfaces analyzed with 26 keV C_{60}^+ ToF-SIMS. 64

IV-2 Secondary ion mass spectra of anti-CD4 on silane glass slide (red) and silane on glass slide (black) impacted with 26 keV C_{60}^+ primary ions .. 65

IV-3 SEM images of AuNPs-antiCD4 labeled on cell micropatterned surfaces 67

IV-4 (a) Schematic illustration of C_{60}^+ impacted on a AuNPs-antiCD4 labeled cell surface; (b) individual events records 68

IV-5 (a) Original secondary ion mass spectrum of AuNPs-antiCD4 labeled on Molt-3 cells; (b) Coincidental ion mass spectrum of co-emitted ions with Au^-;(c) Coincidental ion mass spectrum of co-emitted ions with $AuCN^-$ (m/z 223), inserted spectrum represents coincidental intensity of ion at m/z 120; (d) Coincidental ion mass spectrum of co-emitted ions with silane fragment at m/z 179 70

IV-6 (a) Secondary ion mass spectrum of AuNPs-antiCD4 on glass impacted with 43 keV C_{60}^{2+} primary ions; (b) Coincidental ion mass spectrum of co-emitted ions with $AuCN^-$ (m/z 223) for AuNPs-antiCD4 on acrylated silane modified glass 72

V-1 Depth of emission of individual C_{60} projectiles impacts on: (a) NHS-$(PEG)_{12}$-biotin modified on NH_2 silane surface; (b) avidin immobilized on NHS-$(PEG)_{12}$-biotin modified NH_2 silane surface 81

FIGURE Page

V-2 Secondary ion mass spectra: (a) biotin immobilized on the amino silane modified glass surface; (b) avidin attached on the biotin immobilized amino silane modified glass surface 82

V-3 Secondary ion mass spectra of avidin and biotin linker attached, respectively, on acryl, amino, and amino/acryl mixed silanes 85

V-4 Schematic of irregular coating of avidin and biotin on: (a) acryl silanized glass surface; (b) mixed (acryl and amino silanes) silanized surface 87

V-5 Coincidental spectra with coemitted secondary ions with ion at m/z 422 from biotin-$(PEG)_{12}$-NHS linker. (a) Biotin-$(PEG)_{12}$-NHS on NH_2 silane; (b) Avidin+biotin-$(PEG)_{12}$-NHS on NH_2 silane 89

V-6 Diagram of coemitted secondary ions from an avidin+biotin-$(PEG)_{12}$ NHS+NH_2 silane on glass surface..... 91

V-7 (a) Single coincidental ion mass spectrum with ion at m/z 183 from the biotin-$(PEG)_{12}$-NHS linker of sample avidin+biotin linker on NH_2 silane. (b) Double coincidental ion mass spectrum with two selected coincidental ions at m/z 183 (biotin linker) and m/z 91 (avidin) originate from sample avidin + biotin linker on NH_2 silane 92

LIST OF TABLES

TABLE		Page
III-1	Yields of InO^- and PEG 223 of samples 1-3, 5-6	48
III-2	The number of effective impact and fractional coverage (K) of ^{15}N-labeled glycine/PBS deposited on 100 μm diameter patterns before and after the removal of PR	58
III-3	The number of effective impacts on the overlapping area and the interfacial fractional coverage (K_I) between: ^{15}N-glycine and PBS, PR and PBS, and ^{15}N-glycine and PR before and after the removal of PR.....	58
IV-1	The quantitative results of AuNPs-antiCD4 on cell micropatterns.....	75
V-1	SI yields (%) of avidin+ biotin on various silanes run with 26 keV C_{60}^+ and 43 keV C_{60}^{+2} bombardment	84
V-2	The comparison of the binding densities of complex from samples: avidin with biotin-$(PEG)_{12}$-NHS linker, biotin-$(PEG)_{12}$-NHS linker, and avidin on various silanes	96

CHAPTER I

INTRODUCTION

Secondary ion mass spectrometry (SIMS) is a surface sensitive analytical technique which provides versatile chemical and molecular information (Figure I-1).[1] SIMS utilizes energetic primary ions to impact surfaces. The interrogated surface emits secondary species including electrons, photons, neutrals, and charged ions. The electrons and charged ions produced are steered by magnetic and/or electric fields and recorded with selected types of analytical detectors/analyzers. The resulting emission of secondary ions reveals compositional information about the surface. A comparison of the analytical depths is shown in Figure I-2; SIMS probes only the topmost layers of a molecular surface with a sampling depth on the nanometer scale.[1] By using a focused beam of projectiles, it is possible to obtain chemical images of the surface with a spatial resolution in the submicron range. Significant developments in SIMS imaging coupled with enhancements of molecular ion yields have facilitated the application of SIMS in biomedical research.

SIMS does not require matrix, fluorescent, or isotopic labeling, which eliminates sample preparation and allows direct characterization of native biological species to be performed.[2-4] The main challenge for the SIMS analysis to date is deciphering analyte-specific secondary ion emissions from complex biosurfaces. The application of the

---

This dissertation follows the style of *Analytical Chemistry*.

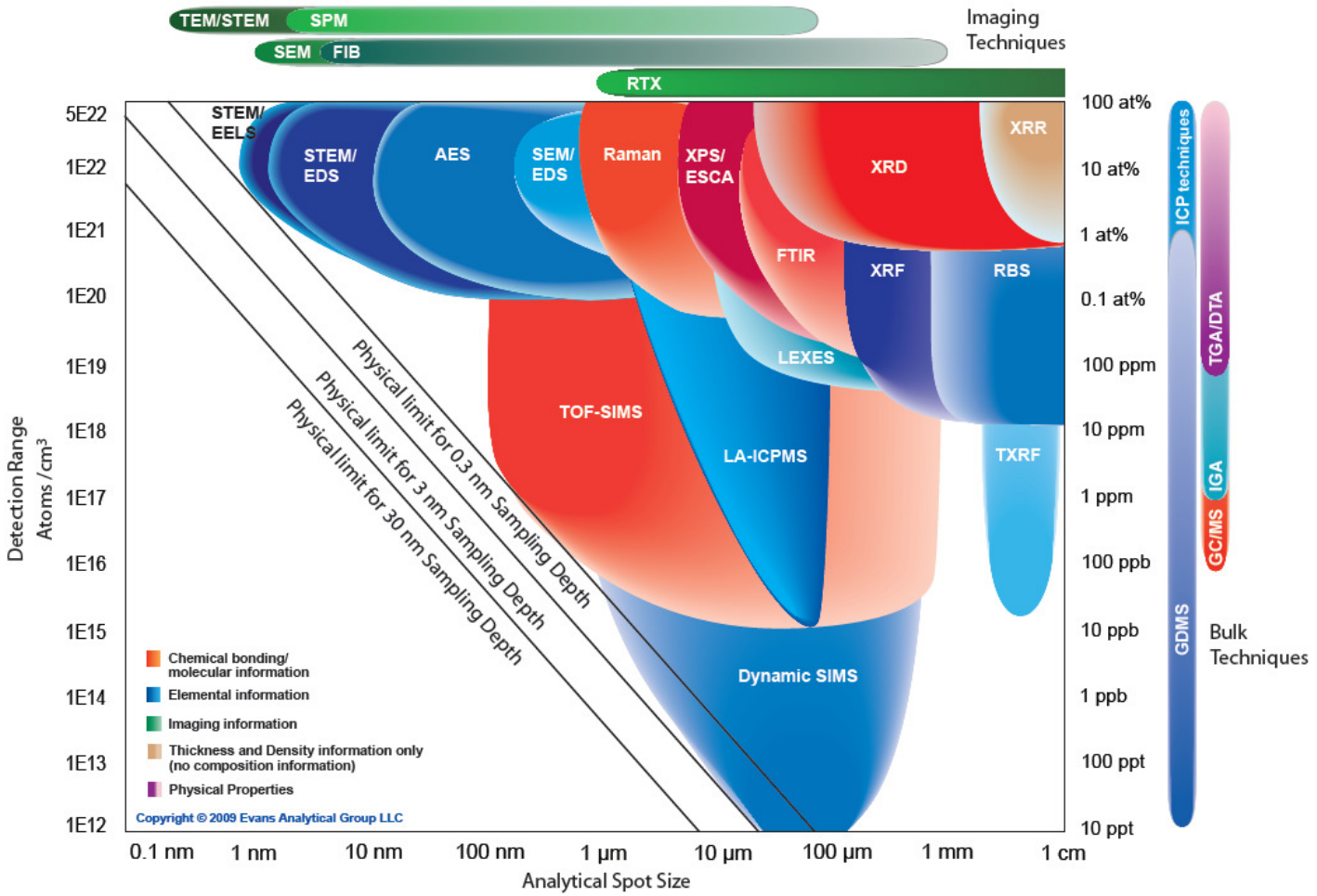

Figure I-1 Comparison of spatial resolutions and sensitivities for various analytical techniques (The image is copyright of Evans Analytical Group, reprinted with permission from reference.[1])

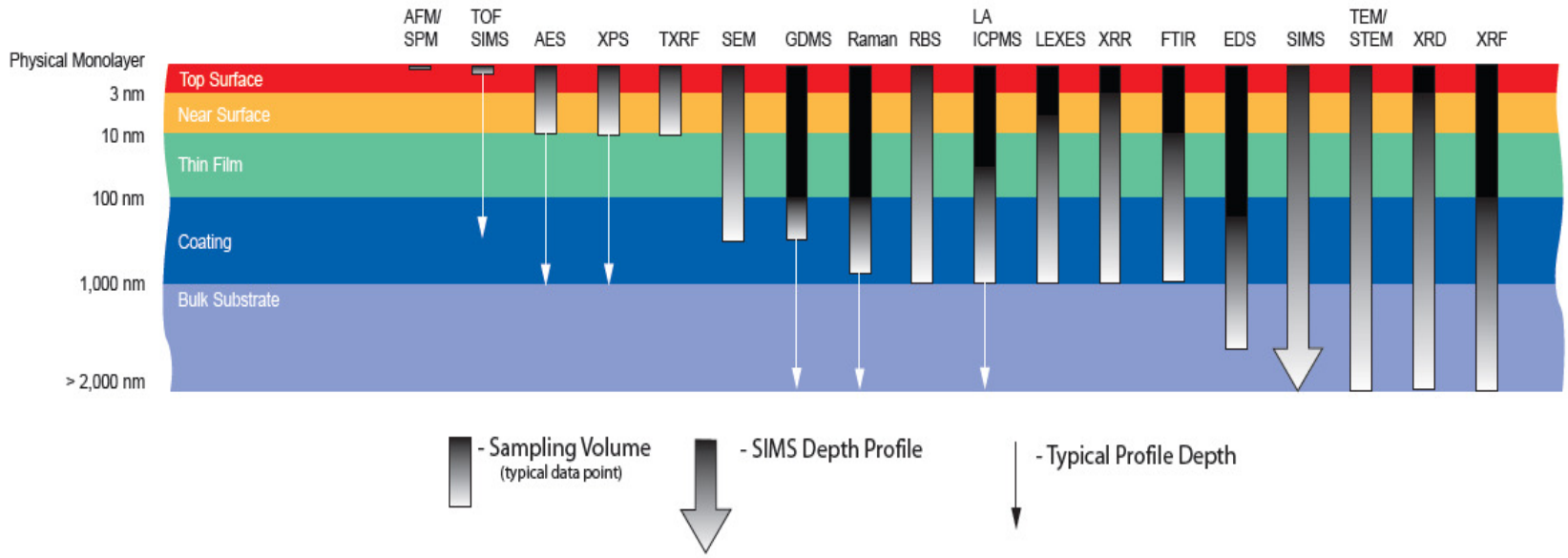

Figure I-2 Comparison of sampling or profiling depths of various analytical techniques. (The image is copyright of Evans Analytical Group, reprinted with permission from reference.[1])

event-by-event bombardment/detection approach enables quantitative analysis without the need for external standardization.

A significant development of SIMS analysis addressed in this dissertation is the quantification of the amount of attached biomarkers on cell surfaces. In this work, we explore the feasibility of determining the number of specific antigens, whose amount may reflect the status of a disease. The methodology developed here allows also to evaluate the performance of micropatterned biointerfaces. Such assemblies are critical for studying and controlling the orientation of biological molecules such as antibodies, proteins, microphages and cells. The micropatterns can further be used for single cell positioning, which in term opens new possibility for studying biological interactions such as a cytokine-release.

Before proceeding with a more detailed description of the objectives of the present work, the features of SIMS are examined below with emphasis on the characteristics related to the goals of this studies: a) the development of a quantitation methodology to determine the fractional coverage of selectively attached biological molecules on micropatterned surfaces and cells, and b) the enhancement of the accuracy of secondary ion identification from a complex sample.

Static SIMS

Static SIMS refers to a low sputtering rate of the surface, which limits the dose of primary ion to less than 10^{12} ions/cm^2. Static SIMS is considered a non-destructive technique because less than 1% of the surface is damaged during analysis. The low fluence of energetic projectiles perturbs only the topmost atomic/molecular layers of the

surface. When the fluence of primary ions bombardment is adjusted to statistically below ~1000 ions/s, each single projectile impact is isolated in time and space. The condition with respect to extremely low probability of repeated impacts is termed a "super static regime", with which the dose of primary ions is less than 10^{10} ions/cm^2. In this operating condition, the low probability of projectile ions impacting on the same spot ensures that most of the sample analyte remains undisturbed. Thus, the quantity and quality of molecular information can be retained.

At present, static SIMS imaging resolution is limited by low secondary ion (SI) yields. Thus, the challenge for static SIMS is to increase the emissions of intact molecular ions, i.e., the quantity of available molecules emitted from a small probing area. Significant enhancement of molecular ion yields and advantages of using polyatomic (cluster) primary ions are discussed below.

Cluster Primary Ions

A first report of the enhancement of sputtered silver or copper ions with light polyatomic/diatomic ion bombardment (e.g. H_2^+, H_3^+, D_2^+, D_3^+) appeared in 1960.[5-6] In 1989, a ion yield enhancement (~10–25-fold) was reported when using a SF_6 polyatomic ion (cluster) bombardment as compared to Cs^+ ions, which have a similar atomic mass.[7] In the same year, Blain et al. also reported a molecular ion enhancement factor of ~50 using keV CsI clusters ($(CsI)_mCs^+$) to bombard an organic target of phenylalanine.[8] The essential observations are: 1) the yield increases nonlinearly with the number of cluster ion constituents; 2) ion sputtering yields an increase proportional to the square of the projectile velocity/momentum.

On the basis of the same impact velocity, the enhancement factor (κ) can be calculated, as the ratio of the yield of ions under cluster (i.e., polyatomic) bombardment to the yield of ions under atomic projectile bombardment is shown as below:[9]

$$\kappa = \frac{Y_{A_n}(E)}{nY_A(E/n)} \qquad \text{Eq. I-1}$$

where $Y_{A_n}(E)$ is the yield of ions under cluster bombardment (A_n), with n constituent, of A atoms, impacted with a kinetic energy of E, and $Y_A(E/n)$ is the yield of ions under atomic projectile A impacted with kinetic energy of E/n.

It should be noted that the ~keV impact energy of the projectile is higher than the binding energy (1–10 eV) of the impacting cluster. Upon striking the target surface, cluster primary ions disintegrate into n constituent atoms. Each atom retains a portion of the original kinetic energy carried by the cluster primary ion.

In 1996, VanStipdonk et al. reported that polyatomic C_{60}^+ projectiles (at 20 keV) produce a phenylalanine molecular yield ~17 times higher than atomic projectiles (Cs^+ and Ga^+) do at the same impact energy.[10] In 2003, Vickerman's group developed a $C_{60}^{1,2+}$ effusion source operated with a total impact energy of ~10–15 keV that greatly increases the secondary ion yields in the mass range (at m/z 400–2500, gramicidin A, PET, and PS2000) compared to the atomic Ga^+, Au^+, and Au_3^+ ion sources.[11-12] The measurement operated with doubly charged C_{60} primary ions, which generate twice the impact energy and give secondary ion yields 2.4 times higher (at m/z 400–2500) than singly charged C_{60} under the same acceleration potential. The low damage from the C_{60} projectile bombardment/sputtering has enabled the C_{60} source to be applied to depth

profiling and imaging. In our laboratory, a similar C_{60} effusion source was built to produce both singly and doubly charged C_{60} primary ions.[13-14] Massive Au clusters with sizes of Au_n^{q+} (n=1–1000, q=1–10) produced by a liquid metal ion source (LMIS) were introduced by Tempez et al. in 2004.[15-16] A molecular ion yield enhancement of gramicidin bombarded with Au_{400}^{+4} was reported as ~1000 times higher than that obtained with Au^+. A high energy massive gold cluster source equipped with a time-of-flight (ToF) mass spectrometer has been developed by Della Negra at the Institut de Physique Nucléaire d'Orsay and custom-built in the Schweikert laboratory at Texas A&M University. The Au instrument is composed of a Au-LMIS (20 keV) coupled to a Pegase acceleration platform (100 keV) to generate Au_{400}^{+4} projectiles with impact energies of up to 130 qkeV when the target is negatively biased at 10 keV. Fernandez-Lima has reported a ~100-fold yield enhancement of lipid-related secondary ions with 520 keV Au_{400}^{+4} as compared to Au_3^+ (130 keV) and C_{60}^{+2} (43 keV).[17]

Coincidence Measurements in Secondary Ion Mass Spectrometry

The enhanced SI yields produced by massive projectile impacts make it practical to run experiments in the event-by-event bombardment/detection mode. In this approach, the ionized ejecta (from an area of 10-20 nm and a depth of 5-10 nm) are mass-analyzed and recorded separately from each impact. The mass spectral data from each probed site can be examined for the occurrence of one or two selected ions. These data reveal further co-emitted ions, i.e. ions originating from molecules located within 10-20 nm of a selected moiety. The first application of the coincidence technique in mass spectrometry was reported by LeBeyec et al. in 1983. They suggested possible

colocalization identification, introduced the concept of a correlation coefficient for co-ejected molecules which reside within the 5–10 nm diameter crater with a single projectile impact.[18] In the early 1990s, coincidence measurements were applied to studies of dissociative photoionization processes for photons and photoelectrons in mass spectrometry.[19-24] Few SIMS research groups have utilized the coincidence technique coupled with ToF-SIMS analysis. The Schweikert research group has utilized the coincidence concept in versatile applications, including measurements of the chemical microhomogeneity of surfaces comprising mixtures of polystyrene and NaF crystals,[25] the differentiation of simultaneously emitted ejecta from mixtures of phenylalanine and deuterated phenylalanine molecules under atomic and polyatomic gold projectile impacts,[26] and studies of the fragmentation–recombination process of gold projectiles and fragments originating from labeled ^{13}C- and ^{15}N-glycine within the perturbed nanovolume domain.[27] Schenkel et al. used coincidence measurements to study a secondary ion enhancement of peptide (gramicidin S) in the interaction with 2, 5-dihydroxybenzoic acid matrix within a nanodomain scale.[28] This dissertation will discuss experiments operated in the event-by-event bombardment/detection mode incorporating efficient $C_{60}^{1,2+}$ (26, 43 keV) and Au_{400}^{+4} (520 keV) projectile impacts to facilitate quantitative analysis of complex biological targets.

More recently, coincidence ion mass spectrometry (CIMS) has been used to quantitatively analyze nano-objects,[29-32] monitor the occurrence of electrons, photons, and secondary ions emitted in coincidence,[33] and perform surface imaging/mapping of co-emitted electrons and secondary ions.[34-35] In our laboratory, we use time-to-digital

converter (TDC) based signal processing electronics to record electrons and ions as start and stop signals respectively. Consecutive events with simultaneously emitted ions are separated and stored in time and space.[25,36] The principle of the coincidence technique is discussed in detail in the following chapter.

Current Quantitative Analysis of Biological Surfaces

This section describes several surface analytical tools that have been utilized to quantify the amount of immobilized biomolecules including fluorescence microscopy,[37] scanning electron microscopy (SEM),[38] surface plasmon resonance (SPR),[39] and x-ray photoelectron spectroscopy (XPS).[3]

Recently, quantification of biomolecules immobilized on surfaces has been achieved by SIMS and fluorescence microscopy.[4,40] Nevertheless, the need for dyes and biomarker labeling always involves complicated sample pretreatments. Also, the overlap of different types of biomarkers in the fluorescence images can reduce the accuracy of identification and localization of analyte species.

SEM is capable of probing the morphology and features of objects of sizes raging from a few hundred to a few nanometers. The instability of biomolecules under high fluence of electron dose has limited the feasibility of using SEM to image nanoparticle–biomolecule conjugates in a cellular environment.[38,41-42] A practical solution is to use a gentle beam at low acceleration energy (< 2 keV), but this suffers a reduction in imaging resolution. Additionally, the secondary electrons or backscattered electrons emitted from a target of interest may be shielded by upper layer species, resulting in incorrect measurements when counting specimen amounts. Also, SEM resolution limits its use for

the characterization of nanoparticles with sizes smaller than 5 nm for a cellular environment.

SPR has been used by Campbell's research group to quantify the surface coverage of immobilized biomolecules by converting the adsorption-induced changes in refractive index and the wavelength shifts of the interface into the coverage of adsorbed streptavidin.[39] The SPR quantitative analysis is based on the adsorption kinetics between the coverage of biotin and streptavidin.[39] The necessity for a change in the refractive index limits the types of detectable molecules. The use of near infrared incident light has also limited the spatial resolution of SPR imaging to a few micrometers.

XPS has been utilized by Castner's group to characterize the surface coverage of DNA/alkylthiol monolayers.[43-44] XPS quantitative analysis shows the elemental composition from the outmost layer of ~10 nm of DNA microarray surfaces. In this case, the XPS quantitation uses radiometric ^{32}P labeling to correlate molecular densities of DNA monolayers with the DNA hybridization efficiency. The use of an x-ray probe limits XPS imaging to a submicron-scale lateral resolution due to difficulties in x-ray focusing.

ToF-SIMS has been combined with ellipsometry, fluorescence microscopy, or SEM to quantitatively determine the surface density of immobilized biomolecules or biomarkers on biosurfaces.[4,45] Before molecular imaging of ToF-SIMS at the nanometer scale can be achieved, a quantitative analysis of the surface density of immobilized molecules or the amount of labeled biomarkers on the biosurfaces is essential for disease-related research. The challenge in current ToF-SIMS biomolecular quantification

remains to differentiate types of molecules while retaining their quantitative information from a complex biosurface.

Present Study

This dissertation deals with the application of cluster ToF-SIMS with CIMS measurement to: 1) evaluate and screen the manufacturing quality of micropatterned biointerfaces prepared stepwise; 2) quantify the binding density of Au nanoparticles (AuNPs)-antiCD4 conjugates selectively attached on the cell surface; 3) elucidate the biological interaction of proteins and molecules through the quantification of the fractional coverage of immobilized biomolecules; 4) enhance the accuracy of secondary ions identification of specific molecules. Biological samples, including AuNP-antiCD4 on cells, biological micropatterns, and avidin-biotin assemblies, which are described in this dissertation, were prepared stepwise in a collaborative endeavor by the Revzin research group at UC-Davis.

CHAPTER II

INSTRUMENTATION AND METHODOLOGY

This chapter describes the instruments used in this study: C_{60} effusion source and Au liquid metal ion source mass spectrometers. Also, the methodology developed to conduct quantitative nano-analysis of biointerfaces is introduced in detail below.

C_{60} Effusion Source Mass Spectrometer

A schematic of custom-built C_{60} source coupled with time of flight mass analyzer is shown in Figure I-1. The C_{60} ToF-SIMS instrument was custom-built in our laboratory. The C_{60} primary ion source is operated under a vacuum of ~ 5×10^{-6} torr with a 60 L/s turbo pump (Pfeiffer Vacuum Inc.) and backed by a 3.7 L/s (8 ft^3/min (CFM)) two-stage rotary vane mechanical pump (Varian Inc.). The primary ion leg is isolated from the secondary ion leg with a gate valve.

An electron impact ionization C_{60} source is used to produce positively charged C_{60} primary ions. To generate C_{60}^{q+} (q= 1, 2) primary ions, a neutral C_{60} powder (Sigma Aldrich, Milwaukee, WI) is placed in a copper reservoir (seen in Figure II-2.) and heated up to the sublimation temperature (~450 °C, 3.9 Amp). The gaseous C_{60} effuses from the orifice of the copper reservoir into a cylindrical electrode and is ionized by the electron impacts, from a heated tungsten wire (0.004 inch in diameter, Alfa Aesar). About 80% of the surface area of the cylindrical electrode (stainless steel tube) is replaced and wrapped with a tungsten wire mesh (0.01 inch in diameter, Alfa Aesar). A semi-circle

tungsten filament (~2 cm in length and 0.004 inch in diameter) is placed ~5 mm away from the grid mesh of the cylindrical electrode. A gradient potential (- 90 V, floating voltage with the filament transformer) is applied between the tungsten wire and the ground grid mesh to accelerate electrons from the filament toward the cylindrical electrode. The gaseous C_{60} vapor inside the electrode is ionized by the impact of thermal electrons that penetrate into the cylindrical electrode with the same velocity. The electron impact ionization process produces a range of various C_{60} cations.

The charged C_{60} primary ions are extracted with a potential gradient (0.5 kV) between the C_{60} effusion source (16 kV) and the extraction plate (15.5 kV). The cations are focused and accelerated toward ground with a pair of electrostatic lenses. A mixture of C_{60} ions is produced and mass selected for specific primary ions with a Wien filter (discussion in the following section). The selected C_{60}^{+} primary ions are then steered toward an off-center aperture (~1mm in diameter) to deflect other ions and prevent the impact of neutrals (C_{60} and contaminant ions remains in the production of source) on the target.

Figure II-1 shows the trajectory of selected C_{60}^{+} primary ions is deflected to pass through the aperture while the trajectory of neutrals, which are not manipulated by the electric and magnetic fields, remains in a straightforward path.

The main chamber of C_{60} ToF-SIMS is maintained at ~2×10^{-6} torr with an oil diffusion pump (760 L/s, BOC Edwards Vacuum, Tewksbury, MA) backed with a two-stage rotary vane mechanical pump (5 L/s, Alcatel Vacuum Product, Hingham, MA). The sample inlet chamber is isolated from the main target chamber with a gate valve and

is maintained with a mechanical pump under a vacuum ~5×10^{-2} torr during sample introduction. To generate 26 keV C_{60}^+ impact energy, a negative bias of 10 keV is applied on the target sample while the effusion source is applied with 16 keV.

After passing through the off-center aperture, the C_{60}^+ primary ions are steered with a set of horizontal and vertical plates toward the sample target. Once the C_{60} projectiles impact the sample target, it generates emission of secondary ions, neutrals, photons, and electrons. The resulting electrons are deflected by a magnetic field (< 100 Gauss) toward a start detector that is composed of chevron formation microchannel plates (MCPs) assembly with a single anode detector. The detected signal is used as a start signal. The resulting secondary anions are accelerated within a potential gradient region (-10kV, 0.9525 cm) toward a ground grid (90% transmission, attached in front of the time-of-flight tube). The next, secondary ions travel in a field-free time-of-flight tube (92.9 cm in length) with the same velocity and are detected by an 8-anode detector as stop signals. The 8-anode detector is comprised of 8 separated segments copper plates assembled with a dual MCPs assembly. The 8-anode detector can record up to 8 ions with the same time of flight striking on the MCPs. The distribution of detected secondary ions on the 8-anode detector can be monitored via the data acquisition program. The even distribution of secondary ions (centering) on the 8-anode is optimized by adjusting the voltages applied on the steering plates that changes the positions of C_{60}^+ primary ions impacts. The maintenance of an effusion C_{60} source is described in detail elsewhere. [46-47]

Au Liquid Metal Ion Source Mass Spectrometer

The vacuum in the Au primary ion chamber leg is maintained at less than 1×10^{-6} torr with a turbo pump (Adixen, ATP400, Alcatel Vacuum Technology France) with a pumping speed of 400 L/s and backed by a dry primary mechanical pump composed of 5 roots type stages (Adixen, ACP28, Alcatel Vacuum Technology France). The Au Liquid Metal Ion Source (Au-LMIS) ToF mass spectrometer schematic is illustrated in Figure II-3.[46] The LIMS is comprised of a tungsten reservoir, tightly wound coil (8-10 turns), and a tungsten needle of 0.2 mm in diameter and 20 mm in length. The tungsten needle is electrolytically etched with the tip of ~90° and placed in the middle of the reservoir. The reservoir and needle is dip-filled with a Au/Si eutectic (97 % Au, 3 % Si by mass fraction, Academy Precious Metals, Albuquerque, NM). To generate Au primary ion emission, the source is heated until it melts (363 ℃). An extraction potential (6.9-7.4 kV) is applied between the needle tip and the source electrode to facilitate the formation of Taylor cone, in which the Au clusters are emitted from the needle tip. The distance between the needle filament and the extraction electrode is ~ 0.5 mm. The fabrication of Au-LMIS is detailed in the reference.[49-50]

The Au-LMIS was developed at the Institut de Physique Nucléaire d'Orsay (IPN in Orsay, France) and the mass spectrometer is assembled in the Schweikert research group at Texas A&M University. The Au-LMIS is floated to 20 kV relative to the platform, providing primary ions with 120 qkeV total kinetic energy at the exit of the platform. Massive gold projectiles are further accelerated to 130 qkeV when impacting on a negatively biased target at 10 kV. The LMIS generates a range of gold primary ions ($1 \leq$

$n \leq 1000$; $1 \leq q \leq 10$). The mixture of Au primary ions is focused by an einzel lens. The beam current of the gold primary beam measured with a farady cup (seen in Figure II-3), without pulsing, is of ~200 nano Amp. After focusing, the specified primary ions are mass-selected by the Wien filter (discussion in the following section).

After the mass selection, the primary ions are deflected to pass through a collimator, with a range of variable aperture sizes (5 mm, 1 mm, 500 μm, and 200 μm). The primary ions are deflected with voltages applied on the primary ion deflector plates to pass through another collimator (500 μm or 200 μm slit), and then enter a pulsing system. The pulsing system comprises of a set of horizontal and vertical pulsing plates (from –1 kV to +1 kV) at the repetition rate of 3 kHz. The purpose of the pulsing is to: 1) reduce the beam current; 2) provide start signal for the acquisition of primary ion time-of-flight to verify mass to charge ratios of various primary ions.

After the pulsing, the primary ions are deflected to pass through the pulsing exit aperture (variable: 200 μm, 500 μm, and 5mm) to impact on a -10kV biased target. The projectile fluence can be adjusted to a desired value by defocusing primary ions or adjusting the extraction current which changes the extraction voltage. The emission current of Au_{400}^{+4} projectiles measured at the target with a current meter is ~ few nano Amp. To ensure a single projectile impact, a fluence of 1000 primary ions per second is set for Au primary ions operation. The resulting electrons are deflected with a magnetic field to be detected with MCPs as start signals. The generated secondary ions are accelerated with -10kV toward a ground grid and then enter a field-free linear or reflectron time-of-flight analyzer. The secondary ion detector is comprised of an 8-anode

copper plate coupled with a dual MCPs assembly. The secondary ion distribution is monitored and centered by changing the voltages of horizontal and vertical steering plates.

Wien Filter

A mixture of Au_n^{q+} ($1 \le n \le 400$; $1 \le q \le 4$) or C_{60}^{q+} (q= 1, 2) projectiles can be mass-selected with a Wien filter. The Wien filter used in C_{60} mass spectrometer is composed of a permanent magnet of 1 Tesla perpendicularly crossed with a variable electric field (a pair of electric plates) to select projectile of interest. Instead, an electromagnet is used in the Au instrument. The variable potential applied on the electric plates enables to select the velocities of passed ions. The equations critical to the Wien filter operation are as follows:

$$\vec{F} = q(\vec{E} + \vec{v} \times \vec{B}) \qquad \text{Eq. II-1}$$

$$q\frac{V_d}{d} = q\nu B \qquad \text{Eq. II-2}$$

$$\nu = \frac{V_d}{dB} \qquad \text{Eq. II-3}$$

where ν is an ion's velocity (m/s), V_d (volt) is the potential applied to the electric plates, d (m) is the distance between electric plates and B is the permanent magnetic field strength (Tesla). When ν is expressed using the mass (m) and kinetic energy (E_K) of primary ions, the relationship between potential V_d (volts) and m (kg) of a desired ion is shown as follows for a given mass, magnetic field and kinetic energy:

$$\sqrt{\frac{2E_K}{m}} = \frac{V_d}{dB} \qquad \text{Eq. II-4}$$

Time of Flight Mass Analyzer

Figure II-4 shows the schematic illustration of the time of flight analyzer used in the 26 keV C_{60} ToF-SIMS. The emitted secondary ions are analyzed with a time-of-flight mass analyzer based on the mass and velocity of an ion. The time required for the arrival of ions at the detector was determined by mass-to-charge ratios. The total required time is the sum of time spent in the acceleration, drift, and deceleration regions. The principle of the time-of-flight is listed as follows:

$$t_{total} = t_a + t_{dr} + t_d \qquad \text{Eq. II-5}$$

t_a :

$$F = ma = qE = q(\frac{V_a}{d_a})$$

$$a = \frac{qV_a}{md_a}$$

$$x(t) = \frac{1}{2}q(\frac{V_a}{md_a})t_a^{\,2} = d_a$$

$$t_a = \sqrt{\frac{2md_a^{\,2}}{qV_a}}$$

t_{dr} :

$$E_k = \frac{1}{2}m\nu_{dr}^{\,2} = qV_a$$

$$\nu_{dr} = \sqrt{\frac{2qV_a}{m}} = \frac{d_{dr}}{t_{dr}}$$

$$t_{dr} = \sqrt{\frac{md_{dr}^2}{2qV_a}}$$

$$t_d: \quad x(t) = v_{dr}t_d + \frac{1}{2}q(\frac{V_d}{md_d})t_d^{\,2} = \sqrt{\frac{2qV_a}{m}}t_d + \frac{1}{2}q(\frac{V_d}{md_d})t_d^2 = d_d$$

$$t_d = \frac{-b \pm \sqrt{b^2 - 4ac}}{2a} \quad \text{, where } a = \frac{1}{2}\frac{qV_d}{md_d}, b = \sqrt{\frac{2qV_a}{m}}, c = -d_d$$

$$t_{total}: \quad t_{total} = t_a + t_{dr} + t_d = \sqrt{\frac{2md_a^{\,2}}{qV_a}} + \sqrt{\frac{md_{dr}^2}{2qV_a}} + \left(\frac{\sqrt{2m}d_d(-\sqrt{V_a} \pm \sqrt{V_a + V_d})}{\sqrt{q}V_d} \right) \quad \text{Eq. II-6}$$

where t_a, t_{dr} and t_d are times spent in the acceleration, drift, and deceleration regions respectively; m is the mass of the secondary ion; q is the valence of the secondary ion; V_a is the voltage applied in the acceleration region; V_d is the voltage applied in the deceleration region; d_a, d_{dr}, and d_d are the lengths of acceleration, field-free drift, and deceleration regions respectively; v_{dr} is the velocity in the drift region.

The mass calibration is based on the total time of arrival to the mass-to-charge ratio:

$$t_{total} = \sqrt{\frac{m}{q}}C_1 + C_2 \quad \text{Eq. II-7}$$

where C_1 is a constant value, determined by the flight lengths and the applied voltage biases, and C_2 is determined by the speed of the timing electronics (< 1channel number). The mass calibration can be experimentally determined as follows:

$$m/q = \left(\frac{t_{total} - C_2}{C_1} \right)^2 \quad \text{Eq. II-8}$$

In practice, C_1 and C_2 can be obtained with more than two ions with known mass-to-charge ratio. For example, H_1 and C_2H^- anions are abundant in the negative mass spectrum and can be used to determine C_1 and C_2.

The mass resolution, the ability of a mass spectrometer to resolve two mass spectral peaks is defined as follows:

$$R = \frac{m}{\Delta m} = \frac{t}{2\Delta t} = \frac{Ch^{\#}}{2\Delta Ch^{\#}} \qquad \text{Eq. II-9}$$

where m is the value of the center of the peak at mass m; Δm is the value of the full width at half maximum (FWHM) read from the peak at mass m; $Ch^{\#}$, the channel number, is proportional to the arrival time of secondary ions. The time resolution of a TDC used in this study is 400 ps per channel. The mass resolution in this study is ~600 at m/z 74.

Detectors and Detection Electronics

The signals of secondary electrons and ions are detected with micro-channel plates (MCP) assembled with single and multi-anode detectors (seen in Figure II-5(a)-(b)). The MCP (Photonis, Pittsfields, MA) is a lead-doped glass electron multiplier with ~10 μm diameter channels arranged at 12° in parallel. The outside diameter of the MCPs for secondary ion detectors is 50 mm with the active area ~40 mm in diameter and a thickness of 0.46 mm. The chevron MCPs amplify signals from charged particle (ions, electrons, neutrals) impacts. The first plate generates a gain of electrons to the number up to ~10^3 and a gain of ~10^6 electrons is eventually achieved across two microchannel plates. Figure II-5(a) shows the SI (stop) detector is composed of MCPs assembly with an 8-anode detector that allows for the detection of up to 8 isobaric ions per event. The 8 segment anode is made of a copper printed circuit plate with each segment separated via a copper wire to prevent cross talk between two anodes. A newly modified anode which

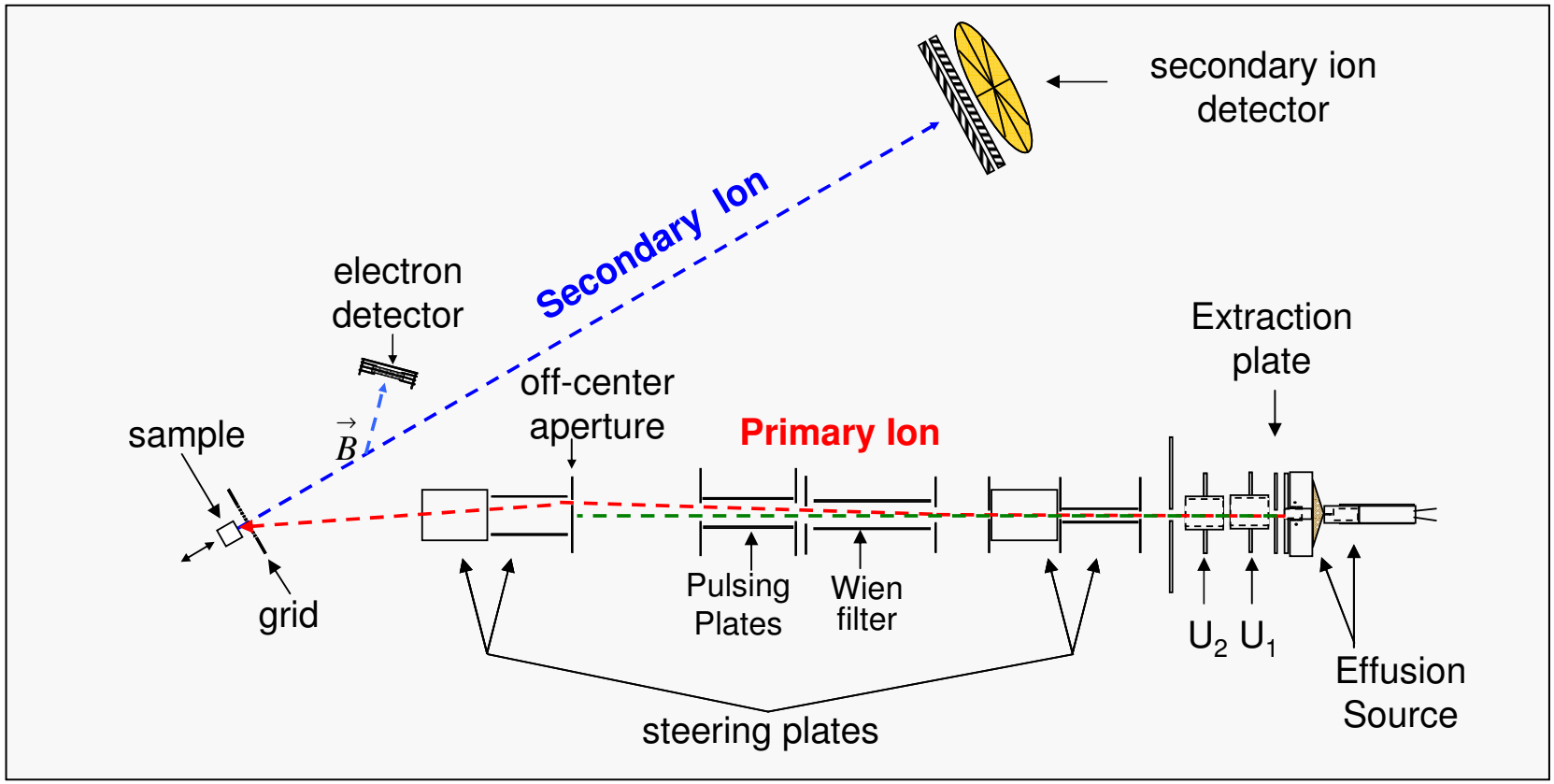

Figure II-1 Schematic diagram of the C_{60} SIMS instrument.[47]

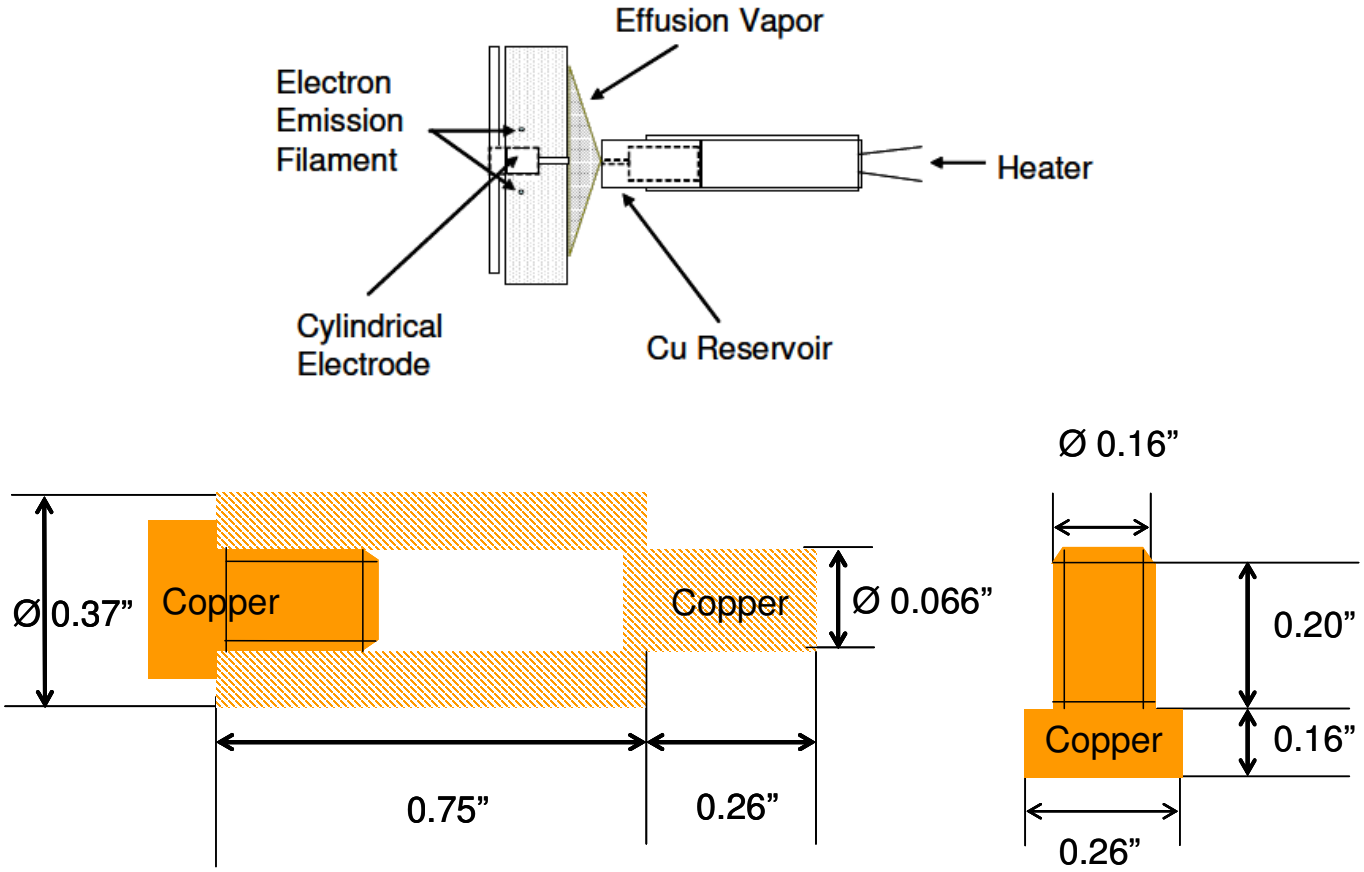

Figure II-2 Schematic illustration of the C_{60} effusion source [48]and the copper reservoir. (not drawn to scale)

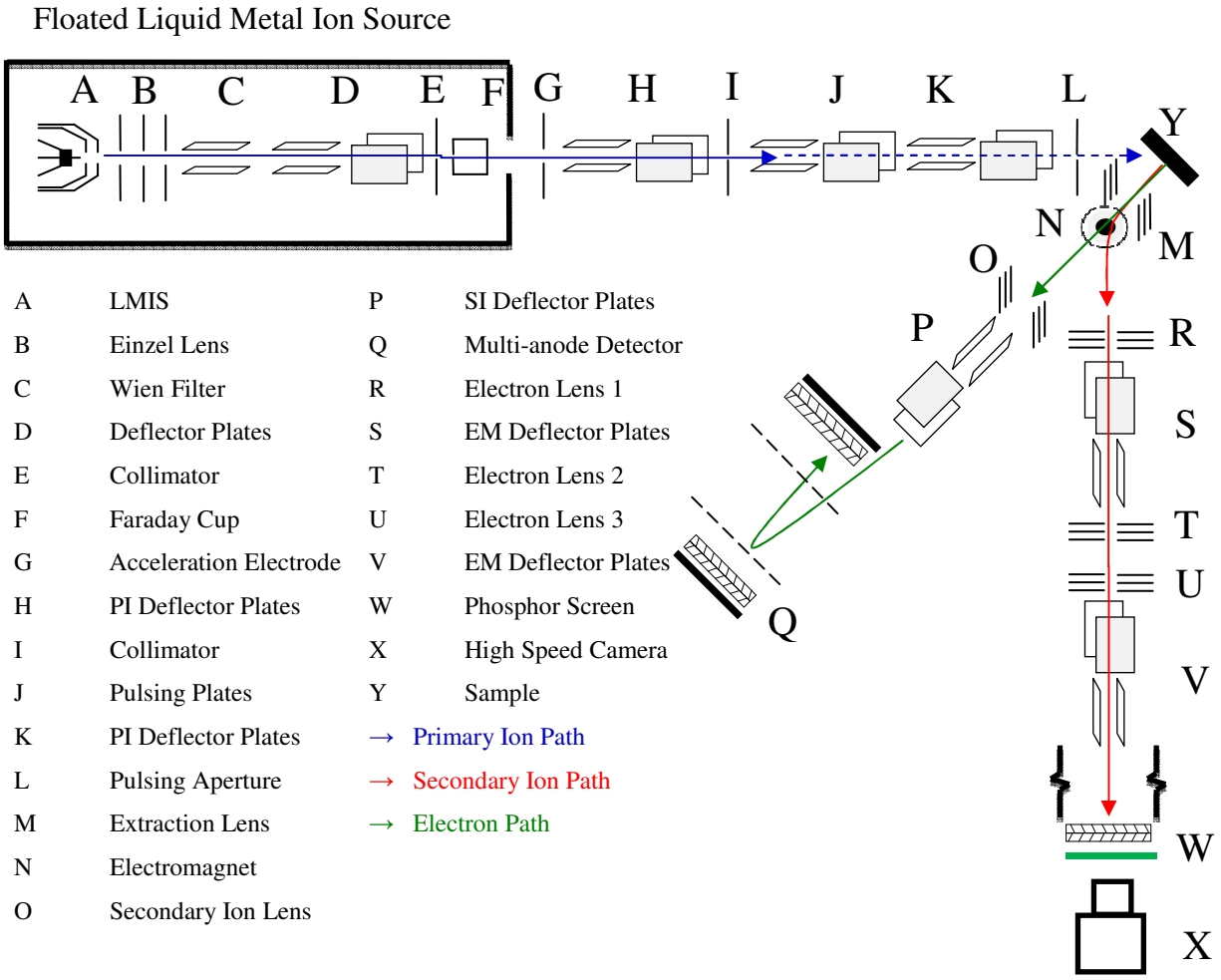

Figure II-3 Schematic illustration of the Au-LMIS ToF-mass spectrometer.[46]

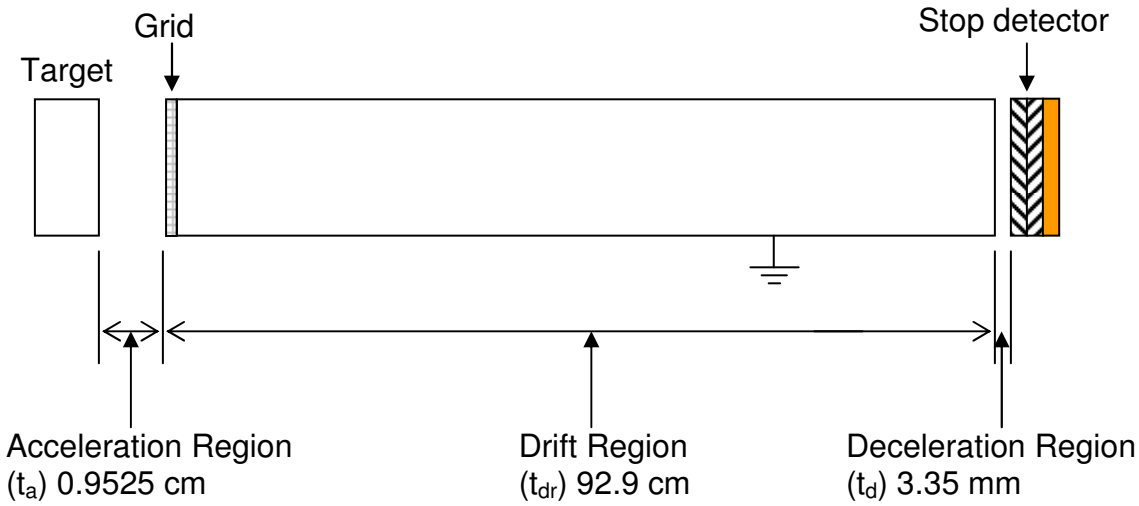

Figure II-4 Schematic diagram of time of flight mass analyzer in C_{60} instrument (not drawn to scale).

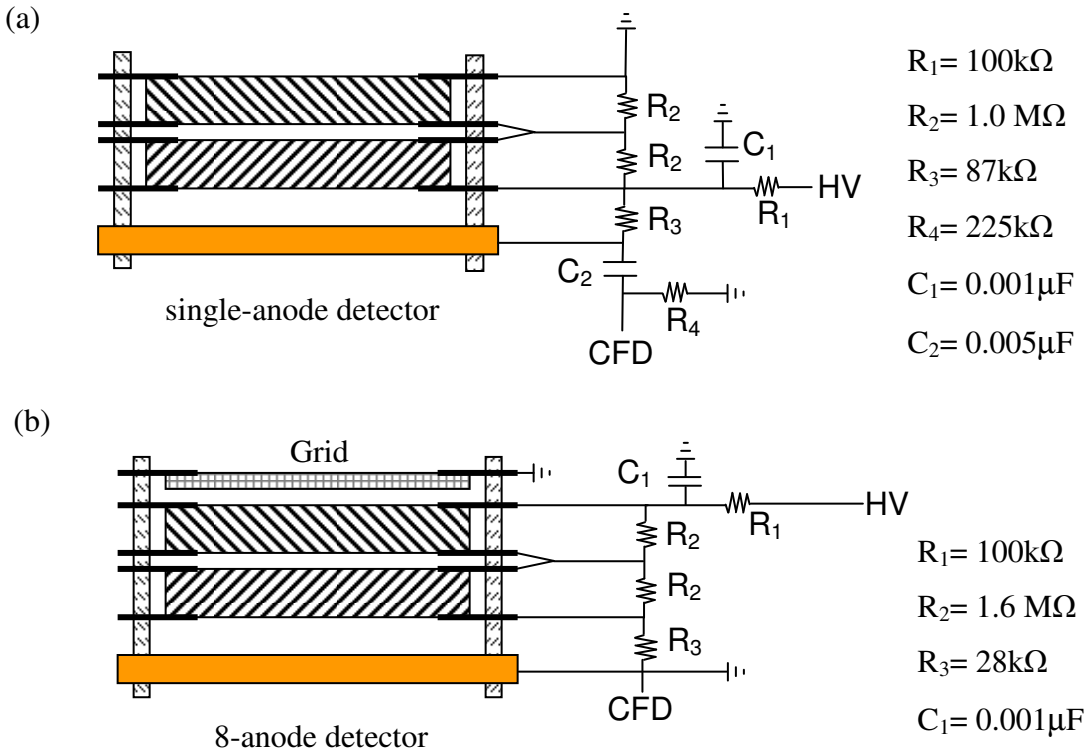

Figure II-5 Schematic diagram of C_{60} mass spectrometer: (a) start and (b) stop detector. (not drawn to scale).

was installed to the C_{60} instrument is with the active area of the total surface of ~95%.

The massive/cluster projectile impacts generate multiple secondary ion emissions. With a single anode, the detector is incapable of recognizing multiple ions striking the MCP assembly with the same time of flight. An eight-segment anode used here can enhance the detection efficiency and decrease the loss of signal. Thus, the optimization of the secondary ion distribution on the 8-anodes is important to ensure that each anode registers equal amounts of ions and the detector therefore achieves the maximum detection capability. The factors that affect the detection efficiency of the SI detector involve the following variables: the transmission efficiency of two grids (90% × 90%), the active area of the MCPs (64%) and the detection efficiency of MCPs (expected range varies from 30 to 80% depending on the type of ions). This results in a detection efficiency of ~40%.[49]

Signal Processing

a. CFD (Constant Fraction Discriminator)

The electron cascade is collected by the anode. The output signal from the start detector is processed with a quad CFD (Tennelec, Meriden, CT). The output secondary ions signals from the stop detector are transmitted into an octal CFD (Ortec, Oak Ridge, TN). The CFD is used to eliminate the ringing signal due to different arrival times and amplitudes (amplitude/signal walk) by setting minimum input pulse amplitude on the CFD threshold. Thus, the discriminator can enhance the time resolution with a fixed trigger threshold, walk or Z/C adjust and constant width. CFD also converts the negative signal (analog signal) to a NIM (Nuclear Instrumentation Module), logic pulse (square

wave). A detailed discussion of the CFD has been described elsewhere.[50]

b. TDC (Time to Digital Converter)

The electron signal output from the CFD is inputted into the start input port of the TDC (Ins. Phys. Nucl., Orsay, France) triggering the acquisition of secondary ion signals from the outputs of the octal CFD as stop signals. The TDC registers the appearance time of stop signals relative to the start with a time resolution of 250 or 400 picoseconds per channel. Also, the TDC converts the logic pulse (square wave) from the CFD into to a digital signal. The data is stored on a PC and processed with the Total Matrix of Events (TME©) software. The schematic of the TME© is shown as Figure II-6. All co-emitted secondary ions produced from a single projectile impact are stored in the row space of a matrix. A conventional secondary ion mass spectrum is obtained with the accumulation of the total events of ions. Also the TME© facilitates to unravel SIs co-emitted with a selected ion. The concept and application of the co-emitted/co-localized secondary ions is widely used in the following chapters.

Event-By-Event Bombardment Detection Mode

As noted earlier, we run a sequence of single projectile impacts in a stochastic fashion on the sample surface. Each projectile is set ~10^{-3} s apart (fluence: 1000 ions/s). The operation of primary ions in the static regime with the dose ≤ 10^{12} ions/cm^2 ensures projectiles stochastically bombard on the target surface without striking on the same spot twice. Each primary ion impact on the target surface leaves a nanovolumetric crater. The molecules residing inside the crater are fragmented and ejected together during each projectile impact. The co-ejected secondary ions from each projectile impact are

resolved separately at time and space as a singular “event”. An event is defined as, with a single projectile impact, the detection of the resulting electrons as a start signal and the detection of resulting secondary ions. Figure II-6 shows that the total secondary ion mass spectrum, similar to a conventional mass spectrum, is an accumulation of all events with the ion co-emission information inherently retained. Typically for any give test, several million impact events were recorded. The coincidence counting technique combined with ToF-SIMS was introduced in our laboratory in 1990.[25] Park et al. reported several requirements for the coincidence counting technique, which include: 1) the impacted region should be small to spatially distinguish the components of sample from one another. 2) each component of the sample must generate a distinct secondary ion signal to allow chemical distinction from one another. In the case of samples bombarded by the 26 keV C_{60}^+ projectiles, the volume from which secondary ions are emitted is ~10^3 nm^3. In the operation of the event-by-event bombardment/detection mode, one can identify spatially co-located molecules from the nanodomains with a singular projectile impact via the coincidental ion mass spectrum. Accordingly, the coincidence ion mass spectrum of co-emissions is unraveled from an accumulation of secondary ions with a set time-of-flight window on a specific ion of interest (seen in Figure II-6). Once one can identify specific fragments of various molecules from a complex surface, the measurement of coincidental emission intensity of two specified ions allows for a variety of applications in the quantification of immobilized species. In this dissertation, the concept of coincidental emissions is applied to quantify the fraction of covered species on the sampling area. Before addressing the concept of the quantitative analysis, the correlation

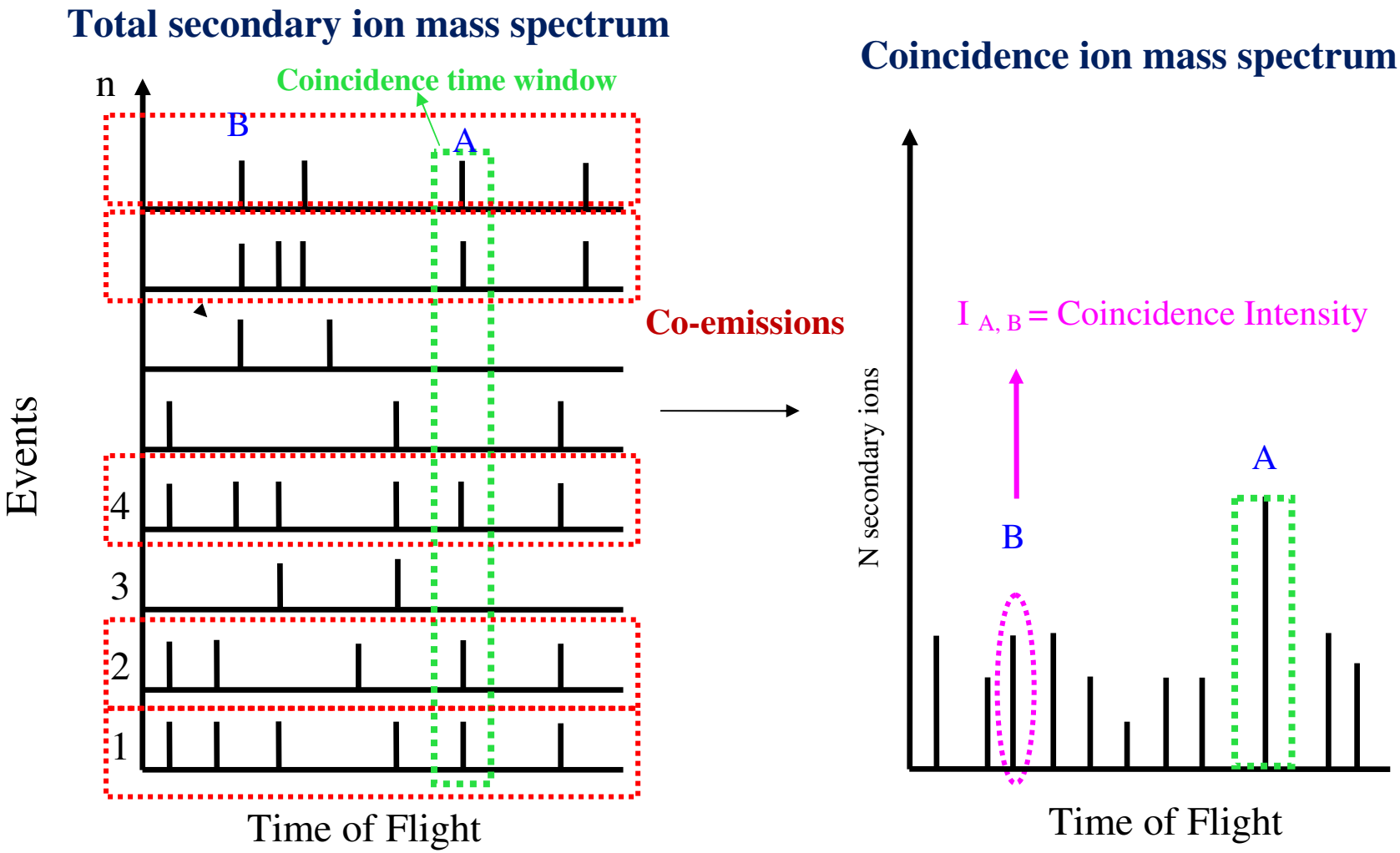

Figure II-6 Schematic illustration of coincidental ion mass spectrum.

coefficient is defined below.

Correlation Coefficient

The concept of a correlation coefficient using coincidentally detected signals is widely applied in the field of nuclear science.[51] We apply the correlation coefficient to determine the extent of the correlation in secondary ion co-emissions, originating from co-located molecules in a nanovolumetric regime, with a single projectile impact.[32,52] A forward description of the correlation coefficient follows:

The yield of detected ions A is computed as in Eq. II-10:

$$Y_A = \sum_{x_A} \frac{x_A N(x_A)}{N_{total}} = \sum_{x_A} x_A P(x_A) = \frac{I_A}{N_{total}} \qquad \text{Eq. II-10}$$

where x_A is the number of detected ions A in a single event ($0 \le x_A < 8$), $N(x_A)$ is total number of events when ions A was detected, N_{total} is the total number of projectile impacts sent to bombard the target surface, $P(x_A)$ is the probability distribution of detected ions A per single projectile impact, I_A is the measured peak area under ion A. The secondary ion yield is expressed as the measured peak area under ion A.

$$Q_{AB} = \frac{\sum_{x_A}\sum_{x_B} x_A x_B P(x_A x_B)}{\sum_{x_A} x_A P(x_A) \sum_{x_B} x_B P(x_B)} = \frac{Y_{A,B}}{Y_A Y_B} \qquad \text{Eq. II-11}$$

where $P(x_A x_B)$ is probability distribution of ions A and B detected simultaneously in a single event, $P(x_A)$ or $P(x_B)$ is probability distribution of detecting ions A or B in a single event, $Y_{A,B}$ is the coincidental yield of simultaneously detected ions A and B. Y_A and Y_B are the SI yields of detected ions A and B respectively. The correlation

coefficients correlated to the spatial homogeneity of chemical species are summarized as follows:

$Q = 1$, the emission of two coincidental ions A and B originated from a nanovolume is uncorrelated, i.e., when ions A and B are emitted independently, the probability of the co-emission is equal to the product of each individual emission/detection probability.

$Q > 1$, the emission of ions A and B is correlated, i.e., the emission of ion A enhances the emission of ion B.

$Q < 1$, the emission of ions A and B is anti-correlated, i.e., the emission of ion A suppresses the emission of ion B.

Quantitative Methodology

The concept of the fractional surface coverage is applied in this study to identify the number of immobilized molecules on the cellular surfaces and the physical assemblies of complex biointerfaces. The quantitative methodology, fractional surface coverage, is in terms the ratio of the number of effective impacts on specified species to the total number of projectile impacts sent to bombard the target surface. As described in Eq. II-1, the probability distribution of detected ions A in a single event, $P(x_A)$, is obtained with the total number of projectile impacts sent to the target. However, in the test case of an inhomogeneous surface, e. g. the surface is partially covered by AuNPs. Thus, in the test case of a complex surface, one should use the number of effective impacts on the AuNPs covered area to correct the formula of the SI yield. Recalling that we operate the cluster ToF-SIMS within the static regime condition, i.e. we send each individual projectile to

stochastically bombard on the target surface, without repeating impacts on the same spot. The calculation of the number of effective impacts (N_e) is described below.

a. Number of effective impacts (N_e) on one component (fractional surface coverage)

When the correlation coefficient is equal to 1 as shown in Eq. II-12, the emission/detection of one secondary ion is independent from the other coincidental secondary ion. Also the probability of the co-emissions of two ions is equal to the product of individual probability of an ion emission. To better understand the fractional surface coverage of each component on a complex surface, the N_0 (or N_{total}) in the calculation of the yield of detected secondary ion (seen in Eq. II-10) is replaced with N_e , which represents the effective number of impacts on the specified component. When SIs A and B are emitted independently from the same component, the correlation coefficient is equal to 1. The above Eq. II-11 can be computed as Eq. II-12. As a result N_e simplifies to $\frac{I_A I_B}{I_{A,B}}$, as shown in Eq. II-16.

$$Q_{AB} = \frac{\sum_{x_A}\sum_{x_B}\frac{x_A x_B N(x_A x_B)}{N_e}}{\sum_{x_A}\frac{x_A N(x_A)}{N_e}\sum_{x_B}\frac{x_B N(x_B)}{N_e}} = \frac{Y_{A,B}}{Y_A \times Y_B} = 1 \qquad \text{Eq. II-12}$$

recalling that $Y_{A,B}$ is the coincidental yield of simultaneously detected ions A and B, Y_A and Y_B are the SI yields of detected ions A and B respectively. The coincidental yield $Y_{A,B}$ is:

$$Y_{A,B} = \frac{I_{A,B}}{N_e} \qquad \text{Eq. II-13}$$

where N_e is the effective number of impacts on a specific specimen; $I_{A,B}$ is the number of co-emitted ions A and B, recorded in the coincidental mass spectrum.

The SI yields of ion A and B are computed as follows:

$$Y_A = \frac{I_A}{N_e} \qquad \text{Eq. II-14}$$

$$Y_B = \frac{I_B}{N_e} \qquad \text{Eq. II-15}$$

where I_A and I_B are the peak areas of ions A and B, respectively measured in the total secondary ion mass spectrum from the same component.

Using equations from II-12 to II-15 one can calculate N_e **:**

$$N_e = \frac{I_A I_B}{I_{A,B}} \qquad \text{Eq. II-16}$$

Once one obtains the effective number of impacts on the specified component (N_e), for a practical application, we use the coverage coefficient, K, to express the fractional coverage of components on the surface:

$$K = \frac{N_e}{N_0} \times 100\% \qquad \text{Eq. II-17}$$

b. Number of effective impacts ($N_e(I, II)$) on two components (interfacial surface coverage)[53]

When more than one type of molecules are co-localized in the emission nanodomain of a single projectile impact, a mathematic formula can be developed to

calculate the interfacial surface coverage of two selected components I and II. Two distinct ions (A (I) and B (II)), originating from two co-localized molecules I and II respectively, are selected to calculate the effective number of impacts on the interface of two components. Before one can obtain $N_e(I,II)$, the respective values of $N_e(I)$ and $N_e(II)$ must be calculated first, as noted above in Eq. II-12 and Eq. II-16. Therefore, $N_e(I,II)$ can be computed as in Eq. II-19:

$$Q_{A(I)B(II)} = 1 = \frac{\frac{I_{A(I),B(II)}}{N_e(I,II)}}{\frac{I_{A(I)}}{N_e(I)} \times \frac{I_{B(II)}}{N_e(II)}} \qquad \text{Eq. II-18}$$

$$N_e(I,II) = \frac{I_{A(I),B(II)}}{I_{A(I)} I_{B(II)}} \times N_e(I) \times N_e(II) \qquad \text{Eq. II-19}$$

where $N_e(I)$ and $N_e(II)$ are the number of effective impacts on species I and II, $I_{A(I),B(II)}$ is the coincidence intensity of ion A (from I) co-emitted with ion B (from II) measured in the coincidental ion mass spectrometry, $I_{A(I)}$ is the peak area of ions A (from I) measured in the total secondary ion mass spectrum, $I_{B(II)}$ is the peak area of ions B (from II) measured in the total secondary ion mass spectrum.

Interfacial fractional coverage then becomes:

$$K_I = \frac{N_e(I,II)}{N_0} \times 100\% \qquad \text{Eq. II-20}$$

Double Coincidence Mass Spectrometry

The concept of double coincidence mass spectrometry is applied in this dissertation (Chapter V) to identify co-emissions of secondary ions with two specified secondary ions. Figure II-7 shows a schematic illustration of single coincidence ion and double coincidence ion mass spectrum extracted from a secondary ion mass spectrum of a complex surface. Each single projectile impact on the samples surface generates secondary ion co-emissions resolved from a nanodomain. The irregularity of the physical dimension and the chemical composition of the complex surface, results in multiple secondary ion emissions originating from various constituents of the assemblies. Individual single projectile impacts are recorded and stored separately at time and space as "events". The test case of the avidin-biotin assembly involves two layers (red and blue layers) with the thickness of ~10 nm recalling that the depth of emission is 5-10 nm, any substrate signals observed in the total secondary ion mass spectrum must be due to the irregularities in the avidin-biotin assembly. To identify secondary ions originating from the avidin and biotin assemblies only, a time-of-flight window is selected for a specified secondary ion originating from the biotin (blue layer) to extract co-emissions with biotin fragments. Subsequently, another time-of-flight window of a specified ion from the avidin (red layer) is set in the previous coincidence ion mass spectrum to identify the events which contain ions co-emitted from both biotin and avidin. The double coincidence method extensively identifies avidin-bioitin domain eliminating interfering contributions from the substrate present in the single coincidence ion mass spectrum.

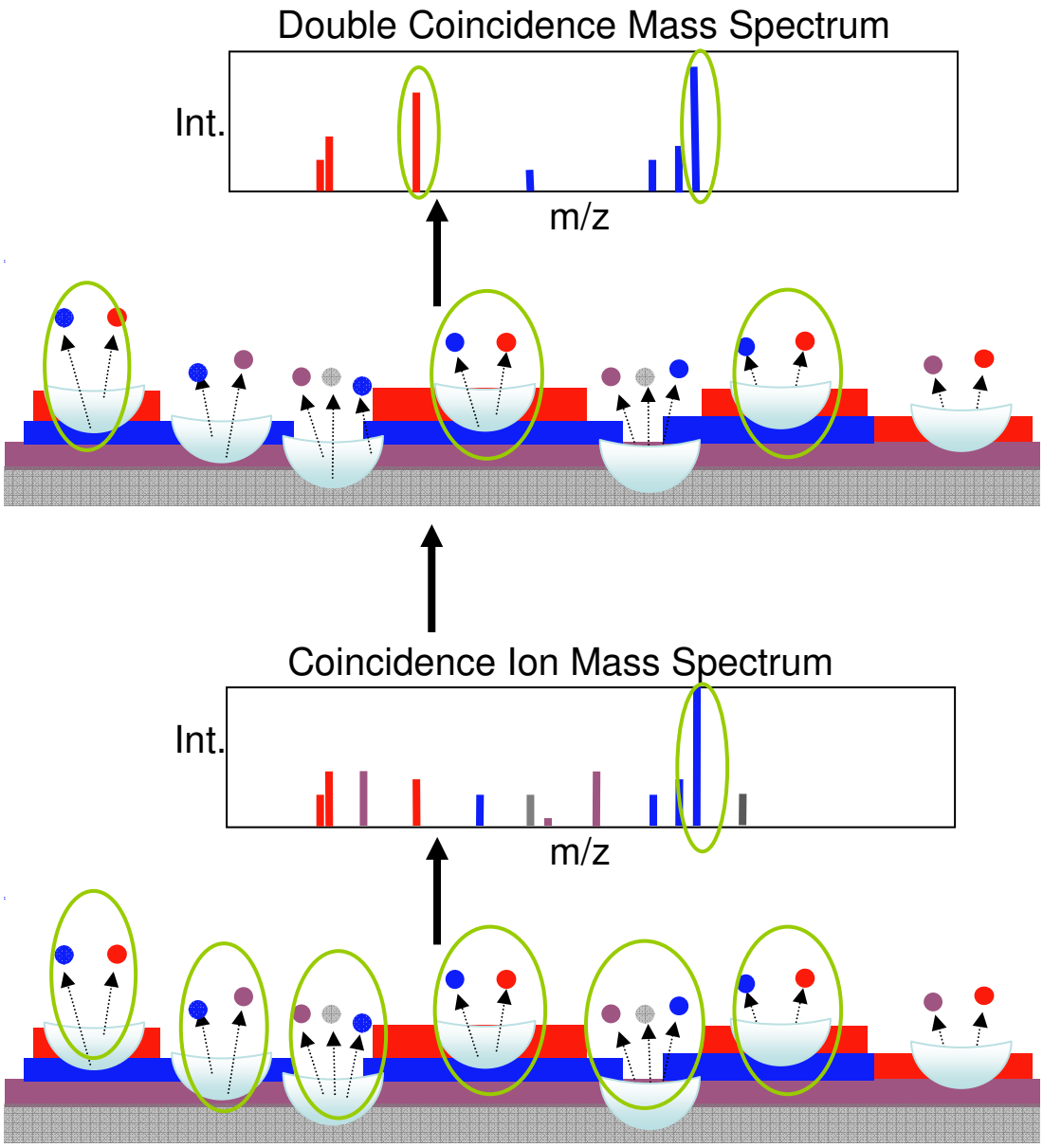

Figure II-7 Schematic illustration of the coincidental ion mass spectrum and double coincidental ion mass spectrum constructed with SIs co-emitted with selected ions originating from specified layers.

CHAPTER III

CHARACTERIZATION AND QUANTIFICATION OF BIOLOGICAL MICROPATTERNS USING CLUSTER SIMS *

Introduction

Micropatterned surfaces are used widely for tissue engineering, cell biology, high throughput-screening and biosensors.[54-56] Processes for fabricating micropatterned surfaces are often complex, involving multiple steps and reagents. Cross-contamination between the steps may lead to sub-optimal performance of the surface: for example, lack of specificity of a biosensor or toxicity of a cell culture substrate.

Most commonly, characterization of biological micropatterns involves immunofluorescence staining and/or imaging by electron or atomic force microscopy. While informative, these approaches provide limited information about chemical species present on the micropatterned surface. On the other hand, secondary ion mass spectrometry, SIMS, may be used to analyze chemical composition of the surface without the need for fluorescent or isotopic tags.[2-4,57] Moreover, imaging SIMS provides a view of micropatterned surfaces based on contrasts in ion intensity; however, this method obtains a total mass spectrum of micropatterned surfaces relying on statistical analysis to characterize local surface composition.[56-58]

---

* Parts of this chapter were reprinted with permission from *Surface and Interface Analysis*, Volume 43, pages 555-558, Li-Jung Chen, Sunny S. Shah, Stanislav V. Verkhoturov, Alexander Revzin, Emile A. Schweikert,"Characterization and quantification of biological micropatterns using cluster SIMS." Copyright [2010] John Wiley & Sons, Ltd.

Our laboratory has been developing cluster ToF-SIMS operating in an event-by-event bombardment-detection mode.[25,59] In this approach, a single projectile impact results in a hemispherical "crater" of ~10 nm in diameter and mass spectra of impacts are detected one-at-a-time.[25,32,52,60] This mode allows the detection of co-emitted ions from individual projectile impacts, since each single impact emission is resolved in time and space.

In the present study, we demonstrate the application to the characterization of biological micropatterns. This approach offers a novel means of quantitative, location-specific analysis of biological micropatterns.

Experimental Section

The fabrication of micropatterns were prepared by the Revzin research group.[58] The surface micropatterning approach employed here was partly based on previously described procedures.[57-58] The micropattern of interest is designed as a biological model that mimics the microcellular environment, and enables a selective attachment of collagen onto a surface of indium tin oxide, ITO, (Delta Technologies, Stillwater, MN).

a. Preparation of Micropatterns

The photolithographic technique was carried out to create micropatterns. The schematic illustration of micropattern fabrication is summarized in Figure III-1. The ITO glass was functionalized with poly (ethylene glycol), PEG, ~5 nm thick self-assembled silane. A layer of photoresist (AZ 5214-E), PR, ~several μm thick was lithographically patterned on top of the PEG-modified surfaces. The PEG silane not protected by PR was removed by exposure to O_2 plasma (300 W for 5 minutes). The micropatterned surface

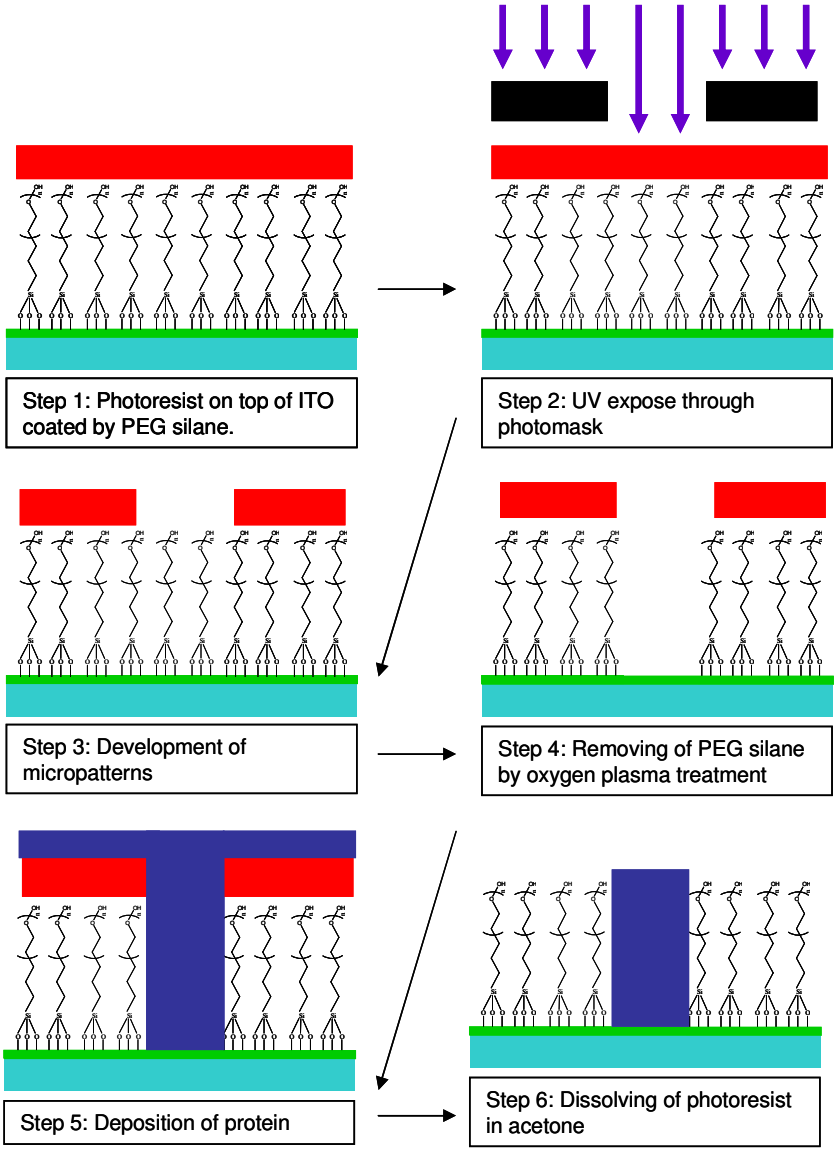

Figure III-1 Schematic illustration of the fabrication of protein attached micropatterns.

was then incubated of collagen (I) (Sigma Aldrich, St. Louis, MO). Lastly, PR was removed by immersion of micropatterned surface into the acetone solvent. The micropatterned surface consists of 100 μm diameter circular patches with the center distance ~250 μm. After the removal of PR, the thickness of the PEG patches is~ 5 nm, and the remaining area is coated with PR with the thickness of ~ several micrometers. The last two steps are to incubate the ITO slides with the biomaterials on the entire patterned surface, and then remove PR by the sonication with acetone.

Figure III-2 and Figure III-3 show detailed flows of fabricating collagen micropatterns. Figure III-2 shows sample 1 is bare indium tin oxide (ITO) glass. Sample 2 is functionalized with the poly ethylene glycol (PEG) silane on the top of ITO. Sample 3 is treated with oxygen plasma to remove functionalized PEG silane. Sample 4 is spin-coated with PR. Sample 5 is sonicated in acetone to remove PR. Sample 6 is incubated with collagen and then rinsed with water.

In comparison, two strategies are carried out to examine the quality of collagen micropatterns (seen in Figure III-3). The circular micropattern is ~100 μm diameter while the distance of two patches center is ~250 μm. In sample 7, circular patches are functionalized with PEG silane while the remaining area is PR. Sample 8 is after the O_2 plasma treatment to remove PEG silane from the circular patches and is followed by the incubation of acetone to remove PR. In strategy 1 (seen in Figure III-3), sample 9 was incubated with collagen after the removal of PEG and PR. In strategy 2, sample 10 is incubated with collagen after the removal of PEG, and then sonicated in acetone to remove PR. Sample 9 was incubated with collagen after the removal of PEG and PR. As

a comparison, sample 10 was incubated with collagen after the removal of PEG from circular patches but before the removal of PR. Sample 10 was sonicated with acetone to remove PR.

b. Preparation of ^{15}N-glycine labeling micropatterned

A ^{15}N-glycine coated micropattern was prepared as follows. 0.112 M of ^{15}N-labeled glycine was dissolved in 1x phosphate buffer saline (PBS) which is composed of 137 mM NaCl, 2.7 mM KCl, 10mM phosphate buffer (Na_2HPO_4 and KH_2PO_4). A solution of 100 μL ^{15}N-glycine was deposited on the entire micropatterned surface while the circular patch is ITO glass and the remaining area is PR. To obtain the ^{15}N-glycine circular patches, the ^{15}N-glycine-coated slide was sonicated with acetone for ~30 mins.

c. Instrumental

The micropatterns were examined with with 26 keV cluster C_{60}^+ ToF-SIMS instruments operated in the event by event bombardment/detection mode (described in Chapter II). As a proof of concept, the immobilized extents of samples after steps 3 and 6 in Figure III-1 were also examined with the quantitative approach. The fractional coverage of collagen or ^{15}N-glycine incubated on the micropatterne samples before and after the removal of PR were investigated with the quantitative approach. The measurements of the interfacial coverage between ^{15}N-glycine and PR were also conducted with the quantitative methodology.

Results and Discussion

a. Characterization of the Micropatterning Quality in Stepwise Processes

Samples 1-10 prepared stepwise were examined with ToF-SIMS. Figure III-5 shows

optical images of sample 7 that is with ~100 μm diameter circular patches when patches are ~250 μm apart. Table III-1 lists the yields of negative ions of samples 1-3 and 5-6. The absence of ions at m/z 223 (PEG-CH_3SiO_2) in sample 3 suggests the complete removal of PEG silane. However, the decrease in the yield of m/z 131 (InO^-) implicates that the ITO layer was over-etched with the O_2 plasma treatment. Figure III-6 shows the absence of PR fragments in sample 5 indicating a complete PR removal, in term resulting in increases of SI yields at m/z 223 (PEG-CH_3SiO_2) and at m/z 131 (InO^-). Figure III-6 shows a distinct CN^- (m/z 26) peak originating from the collagen that deposit on the PEG silane. Secondary ions related to collagen were also found at m/z 42 (CNO^-) and 50 (C_3N^-). These results confirm the attachment of collagen on the PEG silane.

The negative ion mass spectrum (Figure III-7) of sample 7 shows the presence of SIs originating from PR at m/z 107 ($CH_2C_6H_4OH^-$) and 227 ($C_{15}H_{15}O_2^-$), while ions at m/z 223 (PEG-CH_3SiO_2) and 297 (PEG-H) are from PEG. Sample 8, after the removal of PEG and PR, was composed of ITO patches (~100μm in diameter) and functionalized PEG silane in the remaining area. SI yields of Y_{InO^-}, Y_{PR107}, $Y_{PR\ 227}$, $Y_{PEG\ 223}$ and $Y_{PEG\ 297}$ indicate the presence of ITO, PR, and PEG. The yields of $Y_{PEG\ 223}$ and $Y_{PEG\ 297}$ are higher in sample 8 than sample 7. Clearly, the removal of PR resulted in more SI emissions from PEG. However, PR-related peaks were still present in the spectrum due to incomplete removal of PR. A low SI yield of Y_{InO^-} indicates that the O_2 plasma treatment (PEG removal process) overetched the ITO layer.

To identify the most suitable micropattern fabrication process, we may compare the

yields of collagen among samples 6, 9, and 10. Sample 9, collagen was expected to adsorb on the ITO patches area with PEG resisting collagen adsorption. However, the prominent CN^- peaks in sample 6 (Figure III-6) and sample 9 (Figure III-8) show that there is some collagen adsorption on top of PEG silane. The lower CN^- yield of sample 9 indicates a smaller deposited amount of collagen than of sample 6 (2.16×10^{-2} vs. 8.63×10^{-2} respectively). This is likely due to the PR residues on top of PEG that can partially impede the deposition of collagen. Also, the ITO defect found in sample 8 likely lowered the amount of collagen adsorbed on the micropatterned surface.

Figure III-9 summarizes the data obtained from probing ~2 million nanovolumes on the micropatterned surface (sample 10). The collagen was expected to selectively attach onto the circular patches. Multiple secondary ions CN^-, CNO^- and C_3N^- corresponding to collagen SIs were also found in the spectrum. The lower yield of the collagen characteristic ions compared to that of sample 9 is due to the efficient removal of PR after sonication in acetone. The concept of coincidental ion emission was further applied to examine the chemical homogeneity of patterned surfaces.[25] An important observation is that virtually no PR ions were co-emitted with CNO^- (seen in Figure III-10). This test confirmed the efficiency of the PR removal from the micropatterned surface.

b. Quantification of the Fractional Coverage of Collagen Micropatterns

The question at hand was what percentages of the overall probed area (~250 μm × 250 μm) are covered by PR and by PEG respectively? The quantitative methodology can used to characterize the fabrication quality of micropatterns and the incubated amount of collagen on the micropatterned surface. The methodology for a quantitative estimate of

the coverage of a given species has been described previously in Chapter II. In test case 7, the spectrum of ions in coincidence with m/z 107 ($CH_2C_6H_4OH^-$) from PR (not shown) contains other PR related peaks. Conversely a spectrum of ions in coincidence with m/z 223 (PEG-$C_3H_7SiO_2^-$) from PEG resembles the spectrum from PEG alone (not shown).

Briefly, we assume that two co-emitted ions, A and B originating from the same compound (in the present case from emitted PR or PEG) have a correlation coefficient, $Q_{A,B}$, of unity. The effective number of impacts on a specific specimen, N_e (given in Eq. II-16), does not depend on ionization probabilities and detection efficiencies of ions A and B. Thus, for surface objects which are larger than the size of the emission volume,[15] the fractional coverage can be calculated using coincidental method. Knowledge of the ionization probabilities of the co-emitted ions is not required.

The fractional coverage K for PR is obtained from the fragment ions at m/z 107 ($CH_2C_6H_4OH^-$) and 227 ($C_{15}H_{13}(OH)_2^-$). For the sample shown in step 3 of Figure III-1 the value of K was 83 ± 1%. A similar calculation of K as the fractional coverage of PEG yielded a value of ~ 17%. The mask applied for producing the micropattern had a circular patch of 100μm in diameter (the area which PEG can be detected) set in a square of 250 μm × 250μm covered by PR, except for the nominal 100μm diameter patch of PEG in the square's center. Based on the mask dimensions, approximately 87% of the square still has been covered by PR. The difference between the nominal coverage and the experimentally determined value may be due to imperfect transfer between the photomask and the PR layer.

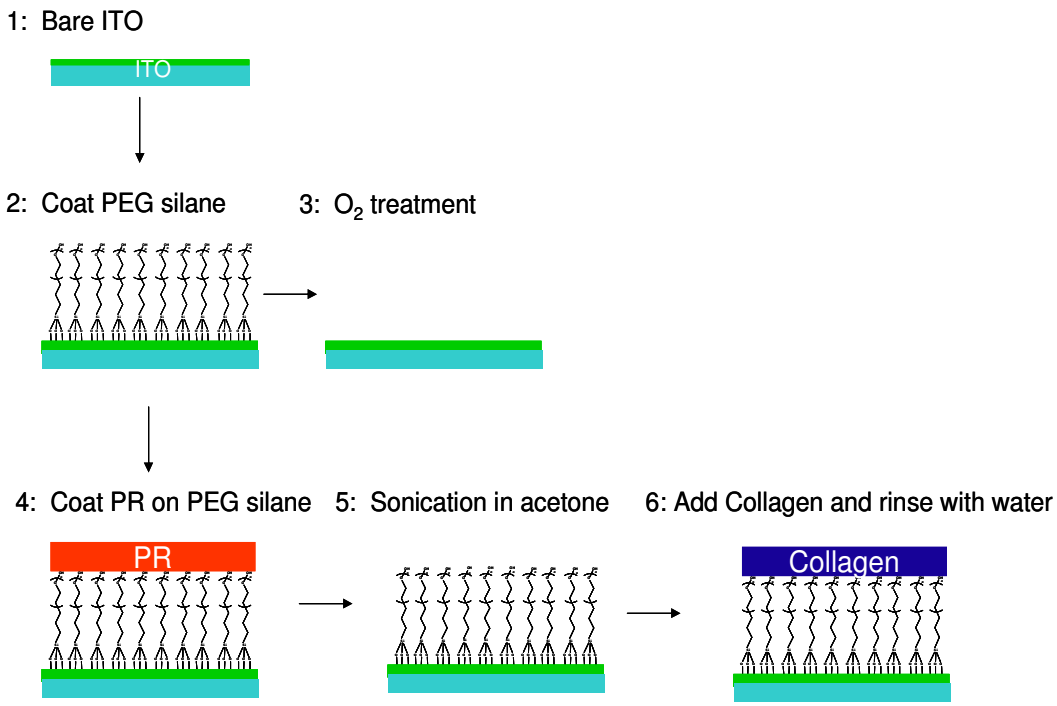

Figure III-2 Schematic illustration of the fabrication processes for samples 1-6.

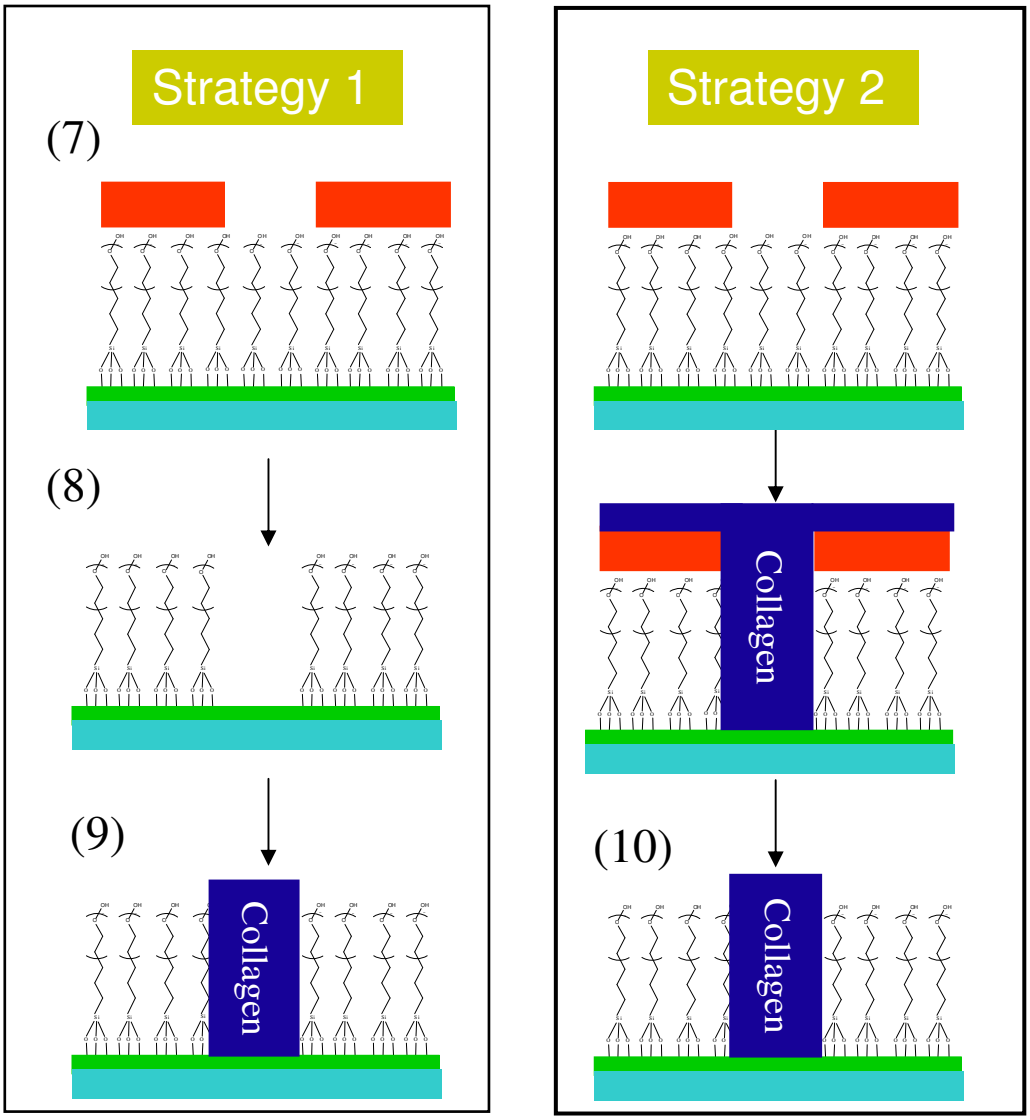

Figure III-3 The comparison flows of fabricating collagen micropatterns.

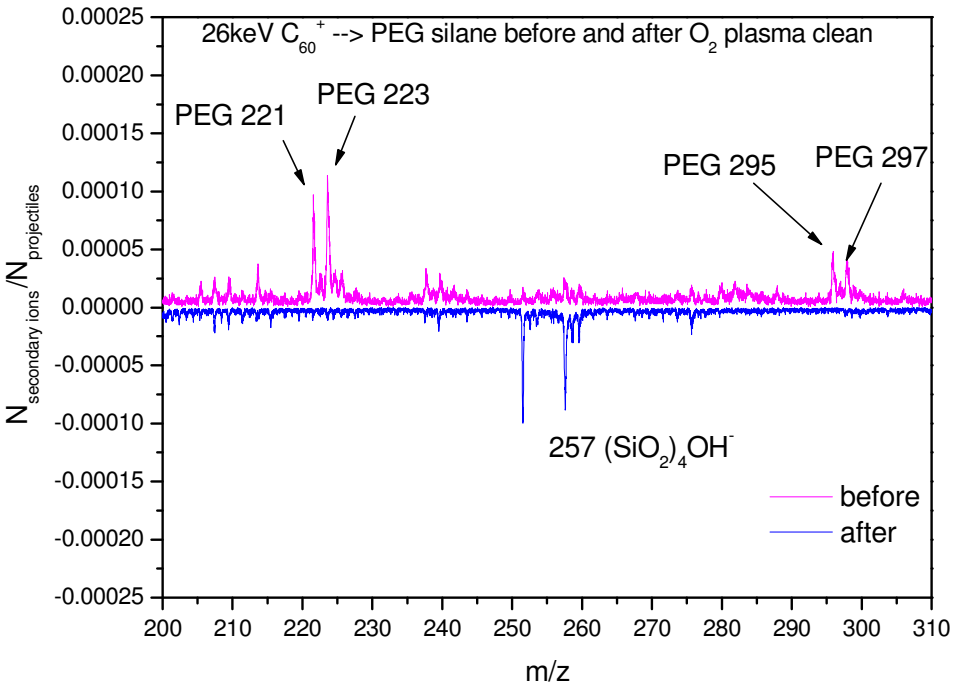

Figure III-4 The negative ion mass spectra of before and after O_2 plasma treatment to remove PEG silane.

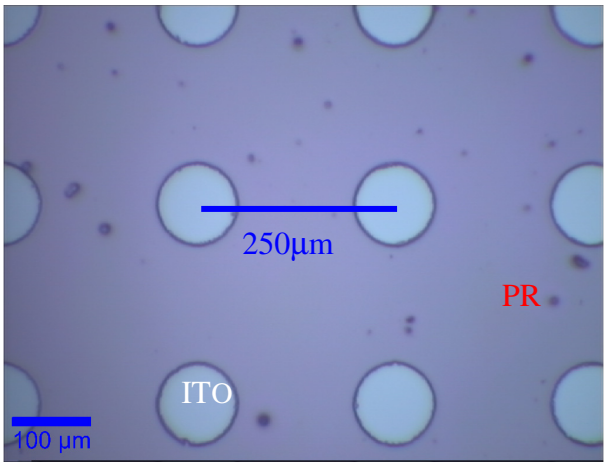

Figure III-5 The optical microscopic image of ITO patches and PR micropattern. The circle area is after the removal of PEG silane with 100 µm in diameter and the remaining area is composed of PR (the distance of two patches is about 250 µm).

Table III-1 Yields of InO^- and PEG 223 of samples 1-3, 5-6		
Sample	Y_{InO^-} (m/z =131)	Y_{PEG} (m/z = 223)
1	1.11×10^{-3}	*
2	2.60×10^{-4}	2.70×10^{-3}
3	1.95×10^{-4}	*
5	1.75×10^{-4}	4.51×10^{-4}
6	2.91×10^{-3}	1.13×10^{-3}
* indicates the absence of the peak		

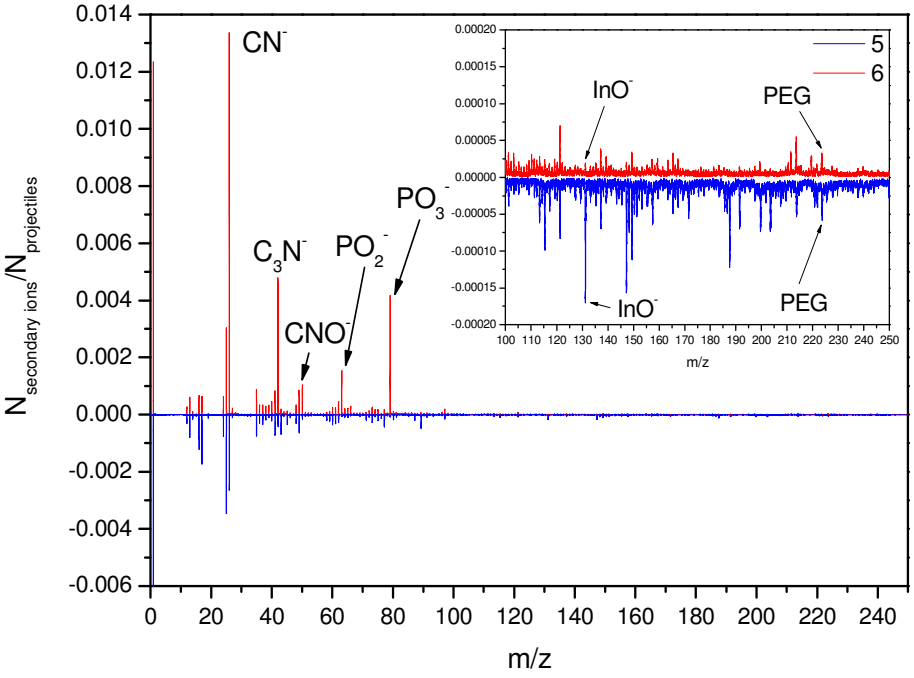

Figure III-6 The negative ion mass spectra of sample 5 and 6. Sample5: Use developer to remove PR on the top of PEG silane, and sample 6: incubate collagen on sample 5.

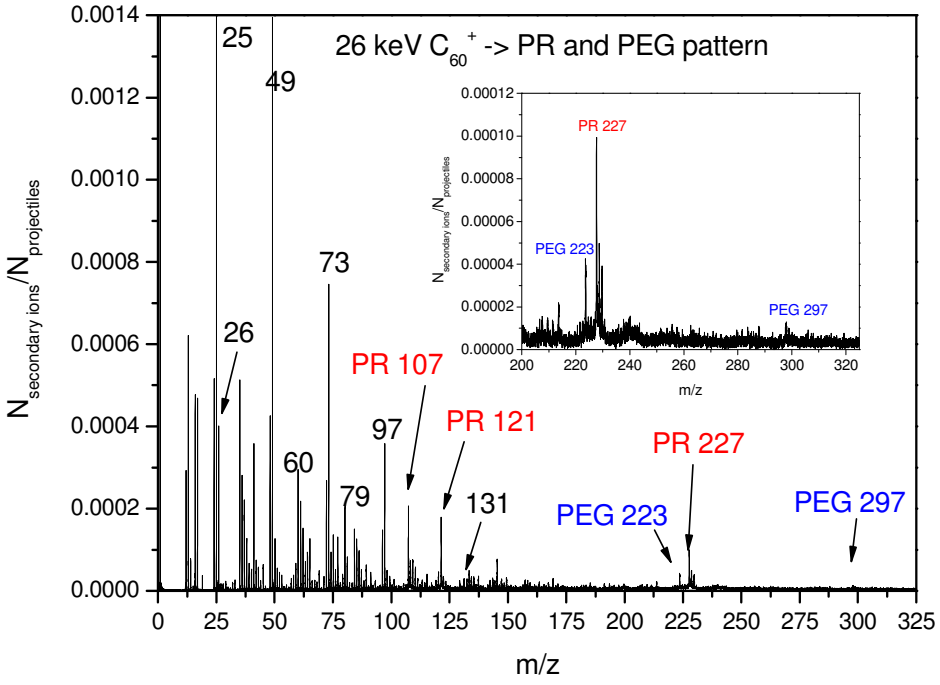

Figure III-7 The negative ion mass spectrum of sample 7.

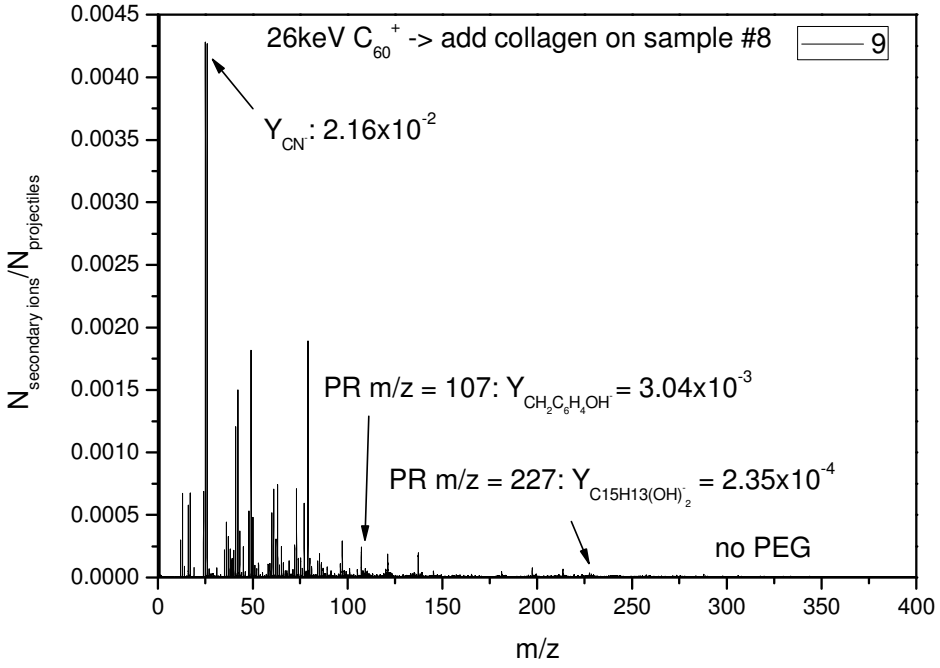

Figure III-8 The negative ion mass spectrum of sample 9.

The validity of culturing cells on ITO surfaces depends on the clean removal of PR from the cell-adhesive, collagen-containing patches because PR residues may be toxic to cells. We tested the presence of collagen in the cell culturing patches via detection of CN^-, CNO^- and C_3N^-. The fractional coverage in the "collagen islands" of the total micropatterned surface was determined to be 19 ± 1%. This value was obtained using the co-emission of CN^- and CNO^- (Figure III-10). The fractional coverage of collagen should be the same as the fractional coverage of PEG obtained earlier. There is reasonable agreement between the values of 19% and 17% for collagen and PEG respectively which validates the collagen adsorption procedure.

c. Quantification of the Interfacial Fractional Coverage of Mixtures

The above studies focused on the quantification of fractional coverage for individual species. To determine the effective number of impacts on mixed species. ^{15}N labeled glycine was used to in lieu of collagen on the micro-patches. The ^{15}N labeled molecules facilitated the examination of quantitative analysis and avoided mass interference with CN^- from $C_2H_2^-$ due to contamination.

As shown in Figure III-11, isotopically labeled ^{15}N-glycine/PBS (0.84mg/ml) was incubated on 100 μm in diameter circular patches that provide specific ^{15}N-labeled secondary ions. Figure III-12 shows that the abundant ions at m/z 27 ($^{12}C^{15}N^-$) and 75 (^{15}N-Gly^-) are ^{15}N-glycine characteristic ions while m/z 165, 181 are from PBS, and ions at m/z 107 and 169 are indicative of PR residues presence. The $^{12}C^{15}N^-$ coincidence ion mass spectrum (CIMS) is obtained when one extracts all the events corresponding to $^{12}C^{15}N^-$ emission. Table III-2 shows that the number of effective impacts divided by the

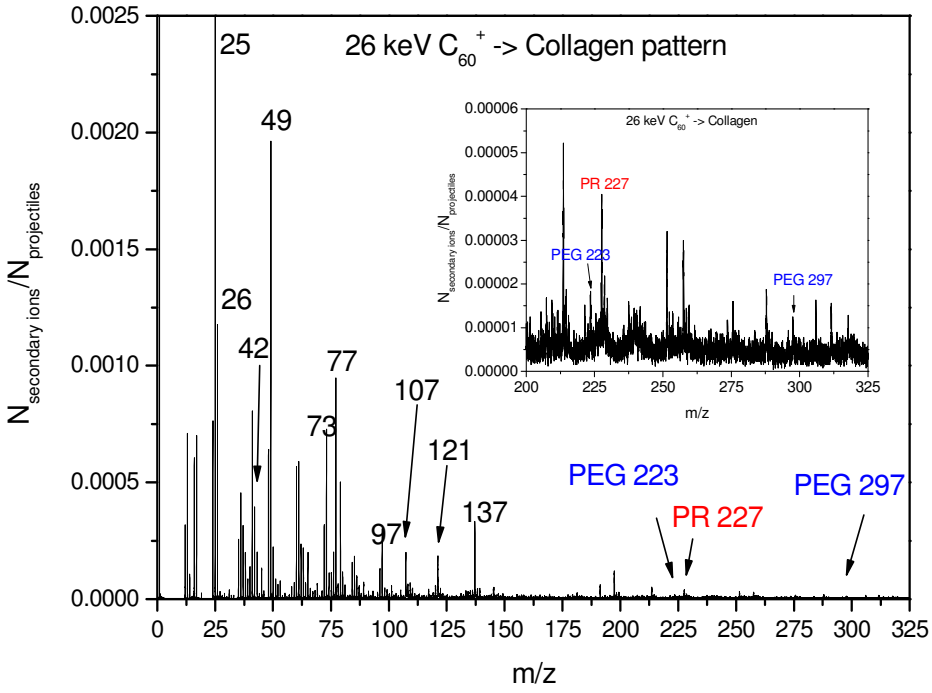

Figure III-9 The negative ion mass spectrum of sample 10.

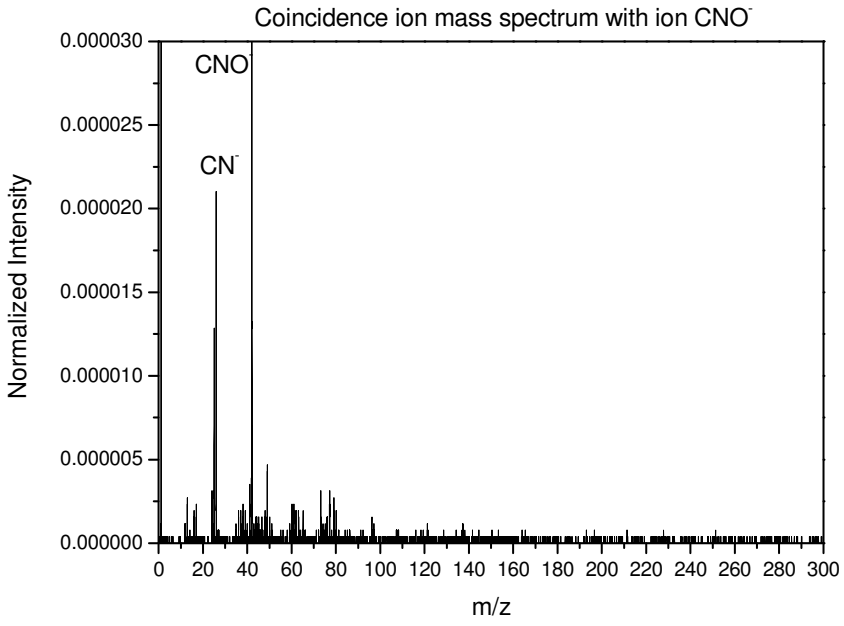

Figure III-10 The coincidence ion mass spectrum of sample 10 with selected ion CNO^-.

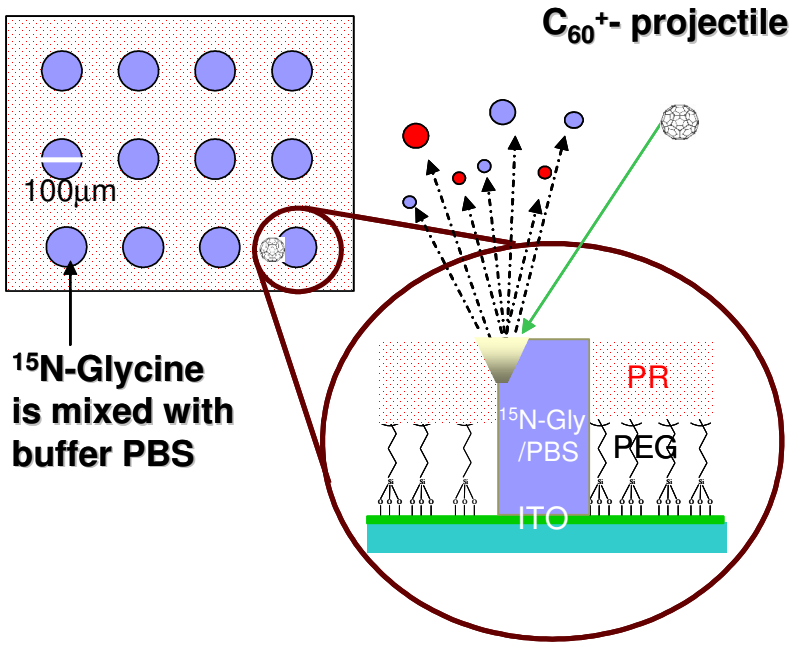

Figure III-11The schematic illustration of single C_{60}^+ projectile impact on the interfacial area between ^{15}N-Glycien/PBS and PR residues.

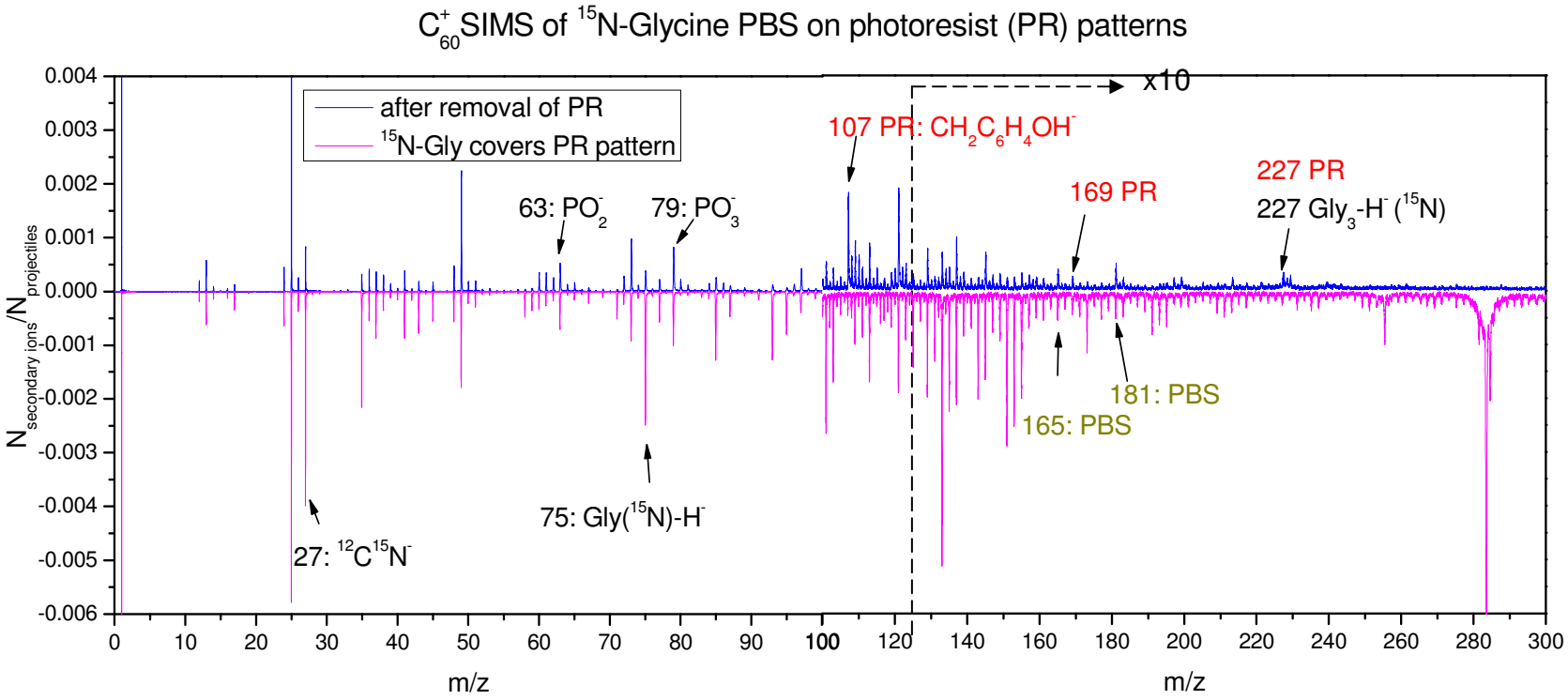

Figure III-12 The negative ion mass spectra of ^{15}N-glycien/PBS deposited on 100μm diameter circle patterned surface bombarded with C_{60}^{+}

number of total impacts on the ^{15}N-glycine ($100\ \% \times N_e / N_{total}$) is about 64% which indicates that ^{15}N-glycine covers 64% of the entire micropatterned surface, while PBS and PR cover 33% and 30% respectively.

In the $^{12}C^{15}N$- CIMS, the presence of ions from PBS and PR allows one to calculate the interfacial surface coverage between ^{15}N-glycine and PBS, and ^{15}N-glycine and PR. The coincidence yield of m/z 165 (PBS) in the $^{12}C^{15}N$-CIMS indicates that ions at m/z 165 and $^{12}C^{15}N^-$ at m/z 27 are co-emitted from a nanovolume of 10 nm in diameter. As shown in Table III-3, the effective number of impacts percentage of the interfacial area of ^{15}N-glycine and PBS is about 31% of the total surface which indicates that most of ^{15}N-glycine analytes were well mixed with PBS buffer at a molecular level. Table III-3 also shows that the interfacial fractional coverage, as described in Chapter II (Eq. II-20), between PR and PBS is ~22% of the total patterned surface while that of ^{15}N-glycine and PR is ~25%.

The effective number of impacts on complex components was also used to examine the fractional coverage of molecules immobilized on the ^{15}N-glycine micropatterned surface after the removal of PR. Before the PR was removed, it covered 87% of the sampling area. Figure III-12 shows the negative ion mass spectra before and after sonication in acetone to remove PR. Theoretically the coverage of the ^{15}N-glycine on 100 μm diameter circular patches should be ~13% of the total patterned surface.

Table III-2 shows that the experimental coverage of ^{15}N-glycine is ~20% of the total surface sampled after the removal of PR. The discrepancy arises likely from ^{15}N-glycine on top of the remaining PR residues because a PR coverage of ~25% was still

present after the PR removal process. Further, a "fractal" overlapping coverage of ^{15}N-glycine and the remaining PR is likely to be a second explanation for the larger coverage of ^{15}N-glycine (20%) than the expected value (13%).

The interfacial fractional coverage of mixed species was obtained by selecting ions at m/z 165 (PBS) and 27 ($^{12}C^{15}N^-$ from ^{15}N-glycine). The interfacial fractional coverage of ^{15}N-glycine and PBS was about ~7% of the sampling area, which indicates that most of the PBS covered surface (~9% of sampling area after the removal of PR) was well-mixed with glycine. Interestingly, after the removal of PR, the interfacial coverage of PR and glycine was only~ 3% of the sampling area while the ^{15}N-glycine covered ~20% and PR covered ~25% of the sampling area respectively. The small interfacial fraction between PR and glycine indicates that only a small portion of the PR was co-localized with ^{15}N-glycine. This result confirms that PR remained mostly in the area outside the patches while ^{15}N-glycine is immobilized inside those.

Conclusion

This study demonstrates that C_{60}^+ ToF SIMS operated in the event by event bombardment detection mode allows for a direct examination of the fabrication quality for micropatterns. The coincidence mass spectrometry methodology is well-suited for testing micropatterned surfaces. It provides a qualitative test of the chemical integrity of surface patches. The test case presented here illustrates the key role of event-by-event bombardment-detection SIMS for validating surface engineering procedures. By monitoring each fabrication stage, a suitable process was determined for the selective attachment of collagen on the micropatterned surface. The concepts of the fractional

coverage and the interfacial fractional coverage of two complex species allows one to qualitatively evaluate the immobilized species on the micropatterned surfaces and determine the mixing extent of complex species.

Table III-2. The number of effective impact and fractional coverage (K) of ^{15}N-labeled glycine/PBS deposited on 100 μm diameter patterns before and after the removal of PR.

Specimen	Coincidence ions (m/z)	Before PR removal		After PR removal	
		N_e	K	N_e	K
^{15}N-gly	75, 27	1276795	64 %	467653	20 %
PR	107, 169	595255	30 %	597090	25 %
PBS	181, 165	669138	33 %	205214	9 %

N_e is as described in Eq. II-16, N_0 is the total number of impacts,

$K=(N_e / N_0) \times 100\%$

Table III-3. The number of effective impacts on the overlapping area and the interfacial fractional coverage (K_I) between: ^{15}N-glycine and PBS, PR and PBS, and ^{15}N-glycine and PR before and after the removal of PR.

Interfacial species	Coincidence ions (m/z)	Before PR removal		After PR removal	
		$N_e(I,II)$	K_I	$N_e(I,II)$	K_I
$N_{e\ \mathrm{gly,PBS}}$	27, 165	614268	31 %	161487	7 %
$N_{e\ \mathrm{PR,\ PBS}}$	107,165	433085	22 %	82779	3 %
$N_{e\ \mathrm{gly,\ PR}}$	27,107	501562	25 %	73979	3 %

$N_e(I,II)$ is as described in Eq. II-19,

$K_I= (N_e(I,II) / N_0) \times 100\%$

CHAPTER IV

CHARACTERIZATION AND QUANTIFICATION OF NANOPARTICLE-ANTIBODY CONJUGATES ON CELLS USING C_{60} TOF SIMS IN THE EVENT-BY-EVENT BOMBARDMENT/DETECTION MODE *

Introduction

Gold nanoparticles, AuNPs, are attractive for tagging biomolecules.[38,61-65] They are usually biocompatible and readily detectable with microscopic and chemical analysis techniques.[38,63-66] Nevertheless, boundaries are set to their detectability by their size and shape. [64,66-68] We present here a mass spectrometric method which provides enhanced information about the bonding of the NP, can determine the number of NPs in a given area of interest, and has the prospect of detecting NPs of dimension below those accessible by the scanning electron microscope (SEM). The mass spectrometric analysis uses ToF-SIMS with C_{60} as projectiles. The experiments are run in the event-by-event bombardment/detection mode which allows to identify molecules co-located within a ~10nm diameter, i.e., the emission area from an individual C_{60} impact.[60]

The novel capabilities are illustrated with the characterization of antibody-AuNP conjugates binding to immune cells. The test case involves anti-CD4 conjugated with

---

* Parts of this chapter were reprinted with permission from *International Journal of Mass Spectrometry*, Volume 303, pages 97-102, Li-Jung Chen, Sunny S. Shah, Jaime Silangcruz, Michael Eller, Stanislav V. Verkhoturov, Alexander Revzin, Emile A. Schweikert,"Characterization and quantification of nanoparticle-antibody conjugates on cells using C_{60} ToF SIMS in the event-by-event bombardment/detection mode." Copyright [2011] Elsevier.

AuNPs which are site-specific nanoprobes for recognizing CD4 antigen on surfaces of T-cells and monocytes.[61-62,64-65,69-71] Levels of CD4 antigen expression are particularly important in T-cells where this antigen provides an entry point for HIV.[72-74] To date AuNP-antiCD4 nanoprobes have been detected and localized by the transmission electron microscope (TEM) and the SEM. However, the instability of nanoparticle-biomolecule conjugates under the high electron dose of the TEM or SEM limits the microscopic detection.[38,41-42]

SIMS in the event-by-event bombardment/detection mode offers the ability to detect the proximity of a nanoparticle probe to the amino acid sites of an antibody. In general, AuNPs are covalently or hydrophobically attached to the target antibody to site specifically label proteins. Cysteine, a sulfur-terminal amino acid, can form strong thiolate bonds with AuNPs. Schenkel et al. utilized SIMS with coincidence counting to study the bonding of peptide and proteins and their non-covalent interactions.[28] We have previously reported a methodology to quantify the surface coverage of Ag NPs on a glycine matrix and the surface coverage of micropatterned species.[29,32,54] The event-by-event bombardment/detection mode allows the identification of co-emitted SIs with an ion of interest. A coincidental ion mass spectrum can be obtained by summing all these coincidental events. The quantification of a surface fractional coverage has been determined in terms of the ratio of the number of effective impacts on a specimen (Ne) to the total numbers of primary ions sent to a target surface (N_0).

We demonstrate below the application of ToF-SIMS in the event-by-event bombardment/detection mode to: a) evaluate the quantity of spherical NPs conjugated

with antiCD4 attached on a cell;[75] b) examine the binding sites between antibody molecules and NPs.

Experimental Section

a. Materials

3-acryloxypropyl trichlorosilane was purchased from Gelest, Inc. (Morrisville, PA). 10x phosphate buffered saline (PBS) without calcium and magnesium was purchased from Sigma Aldrich (Saint Louis, MO). Formalin was purchased from Fischer Scientific. Purified mouse anti-human CD4 (13B8.2) was purchased from Beckman-Coulter (Fullerton, CA). Colloidal gold (30 nm) conjugated monoclonal antibody to Human T-cell helper (AuNP/anti-CD4 conjugate) was purchased from EY Laboratories (San Mateo, CA). RPMI 1640 cell medium was purchased from VWR (West Chester, PA). Fetal bovine serum (FBS), penicillin, and streptomycin were purchased from Invitrogen (Carlsbad, CA). Molt-3 T-lymphocyte line was purchased from American Type Culture Collection (ATCC).

b. Preparation of T-cell Binding Surfaces

Glass substrates were first modified with 3-acryloxypropyl trichlorosilane to promote antibody adsorption according to previously reported procedures.[76-77] Briefly, glass slides were treated in an oxygen plasma chamber (YES-R3, San Jose, CA) at 300W for 5 min. The substrates were then incubated in 2 mM solution of 3-acryloxypropyl trichlorosilane diluted in anhydrous toluene for 1 hr. Silanized slides were then rinsed in fresh toluene, dried under nitrogen, dehydrated at 100 ºC for 2 hrs., and stored in a desiccator prior to use. To prepare areas for T-cell capture, 0.2 mg/ml

purified mouse anti-CD4 antibody dissolved in 1xPBS solution with 0.005% Tween-20 was printed onto silanized glass slides using a MicroCaster hand-held microarrayer system (Whatman Schleicher&Schuell). Similarly, 10 μg/ml AuNP/anti-CD4 conjugate antibody containing 0.005% Tween-20 was also printed.

c. Formation of Gold Nanoparticle Labeled Cellular Micropatterns

Molt-3 cells were maintained in RPMI 1640 media with 10% (v/v) fetal bovine serum (FBS), 100 μg/ml penicillin and 100 μg/ml streptomycin at 37 ºC in a humidified atmosphere with 5% CO_2. The cells were spun down at 1200 rpm for 3 min. and then suspended in 1x PBS to a final concentration of 5 x 10^6 cells/ml. The cells were seeded onto anti-CD4 antibody arrayed substrates. After one hour incubation at 37 ºC, substrates were washed with 1x PBS solution to remove unattached cells. Substrates with patterned adherent T-cells were then fixed with 4% formalin solution for 15 min. followed by three washes in 1x PBS solution. Finally, substrates were incubated with 10 μg/ml AuNP/anti-CD4 conjugate antibody for 1 hr. followed by washing in 1x PBS to remove unattached gold particles.

d. ToF-SISM Analysis

The samples were on glass substrates modified with anti-CD4 Abs and incubated with CD4 antigen-expression T-cell line (Molt-3). Molt-3 cells captured on the glass surfaces were incubated with AuNPs/anti-CD4 conjugates. They were analyzed with a sequence of individual $C_{60}^{1,2+}$ projectiles at total energies of 26 and 43 keV respectively. To obtain statistically valid data, the experiments were run with a total of ~10^6 single impacts each spaced ~10^{-3} s apart, over a sampling area (800 μm diameter) covering

~3000 cells. In the conventional secondary ion mass spectrum, antibodies and cell receptors produce similar characteristic peaks. AuNP labeling was used to impart signature mass peaks to antiCD4 molecules. AuNPs generated specific negative Au and Au adduct ions in the secondary ion mass spectrum that allowed to identify the AuNPs-antiCD4 in a complex biological system. We also employed the SEM to visualize the presence of AuNPs (~30 nm in diameter) on the cell surfaces.

e. SEM

The AuNPs and cells were analyzed by the scanning electron microscope (SEM; Jeol-7500F Cold Field Emission). SEM operated on gentle beam mode (l kV) was used to image the morphology and shape of cells (×700 magnification) and AuNPs (×70,000 magnification) under vacuum (~10^{-5} torr).

Results and Discussion

a. Secondary Ion Mass Spectrum and SEM images of AuNPs-antiCD4 on Cells

The secondary ion mass spectrum of the AuNPs-atniCD4 conjugates immobilized on cells is shown in Figure IV-1. Similar to conventional SIMS, the cumulative SIs mass spectrum shows the chemical information of the complex surfaces. The negative ions in the mass range from m/z 30 to 120 are labeled as peaks suggested to originate from amino acid residue side chains, i.e., indicating the presence of antibodies (shown in Figure IV-1(a)). A corroborating indication of these peaks arising from amino acids is the increase in their intensities when comparing the immobilized antiCD4 to the silane background (shown in Figure IV-2). The palmitate ($C_{16}H_{31}O_2^-$) and oletate ($C_{18}H_{33}O_2^-$) ions originate from the topmost layer of cell surfaces that are composed of the cellular

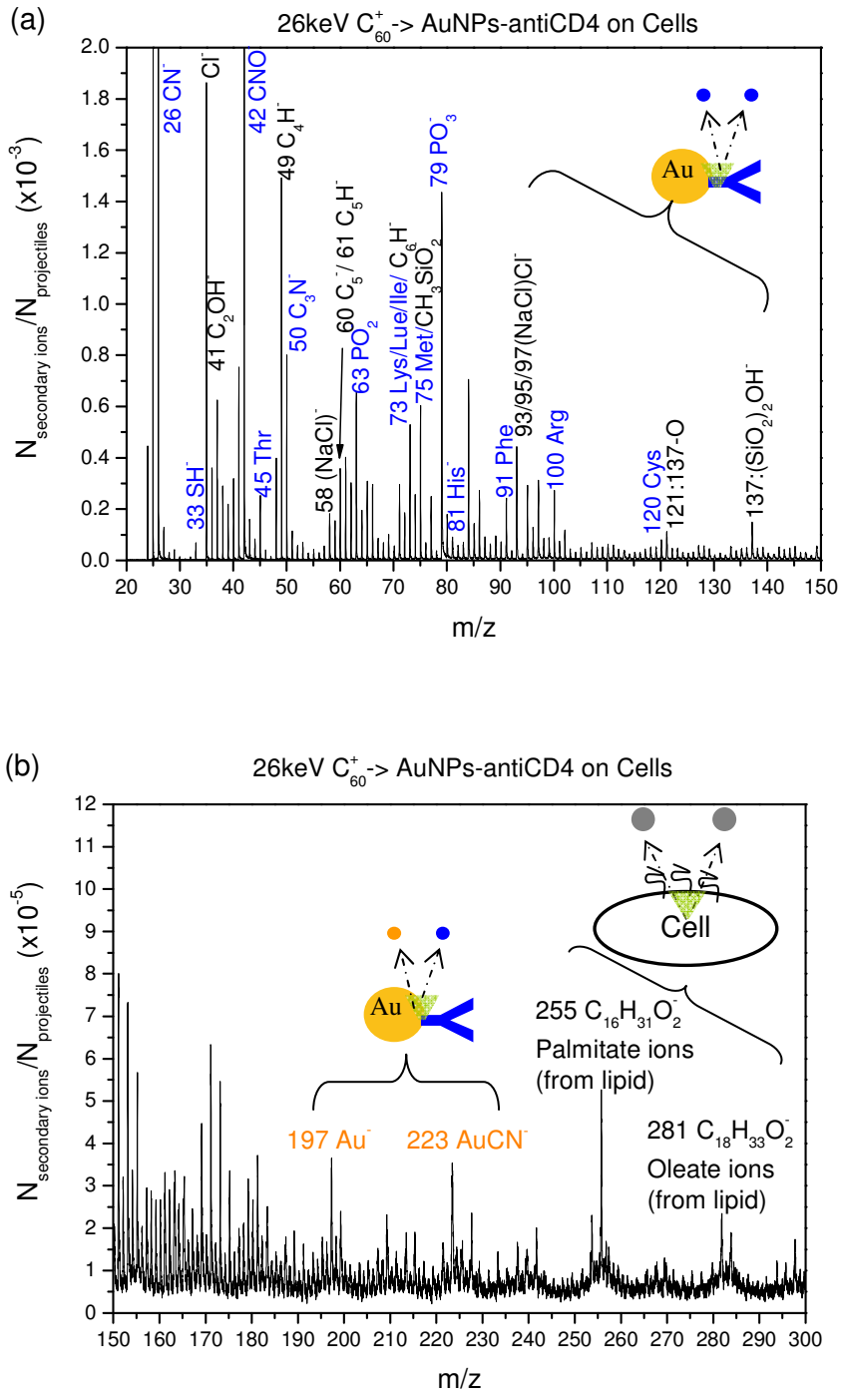

Figure IV-1 Secondary ion mass spectrum of AuNPs-antiCD4 on Molt-3 cell micropatterned surfaces analyzed with 26 keV C_{60}^+ ToF-SIMS. (a) m/z 30-150; (b) m/z 150-300.

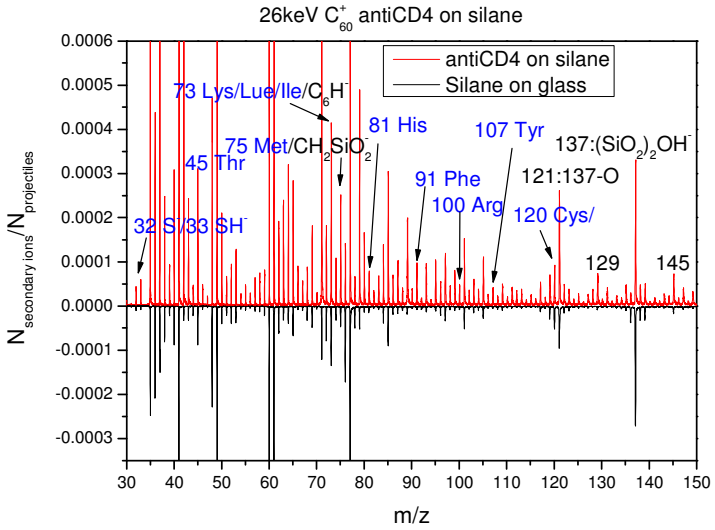

Figure IV-2 Secondary ion mass spectra of anti-CD4 on silane glass slide (red) and silane on glass slide (black) impacted with 26 keV C_{60}^{+} primary ions.

lipid membranes (Figure IV-1(b)). The peaks at m/z 197 (Au^-) and 223 ($AuCN^-$) are AuNP adducts emitted from the AuNPs labeled on antibodies (anti-CD4) bound to the cell receptor sites. These unique signals corresponding to AuNPs at m/z 197 (Au^-) and 223 ($AuCN^-$) confirms the successful immobilization of AuNPs-antiCD4 to cells.

The presence of AuNPs immobilized on the cell was also verified with SEM images. As shown in Figure IV-3(a), the morphology of Molt-3 cells (~9 μm diameter) cultured on microcasted anti-CD4 surfaces (800x1200 μm^2) were investigated by the SEM.[78-79] The SEM images show that cell morphology remains intact in the vacuum environment (~10^{-6} torr). Figure IV-3(b) shows the attachment of AuNPs with size ~30 nm in diameter conjugated with anti-CD4 on the Molt-3 cell surfaces. The blurred image of AuNP-antiCD4 on cells indicates the difficulty in using the SEM to image AuNPs of 30 nm in the cellular environment. The high electron dosage of the SEM technique causes the AuNP-antiCD4 conjugates to become unstable and decompose.[38,42]

b. Coincidental Ion Mass Spectra of AuNPs-antiCD4 on Cells or Silane Modified Glass

The schematic illustration of applying the event-by-event bombardment/detection mode to probe the cellular surface is shown in Figure IV-4(a). The random C_{60} projectiles statistically impact either the cell rich region or the AuNPs-antiCD4 area. As shown in Figure IV-4(b), the first event illustrates a single C_{60}^+ primary ions impact on the lipid membrane region and the detection of co-emitted SIs from a lipid resolved nanovolume of 5-10 nm in depth and 10 nm in diameter.[60] The second event expresses the projectiles impact on the co-located AuNPs and anti-CD4. The third event shows the

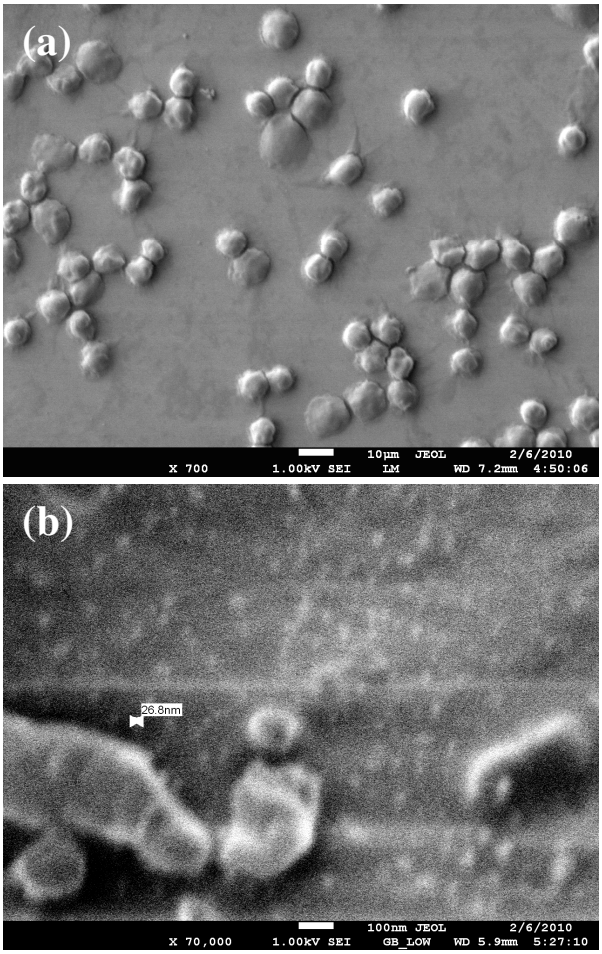

Figure IV-3 SEM images of AuNPs-antiCD4 labeled on cell micropatterned surfaces. (a) Molt-3 cells (~9 µm in diameter), scale bar: 10 µm; (b) AuNPs- antiCD4 attached on Molt-3 cell, scale bar: 100 nm.

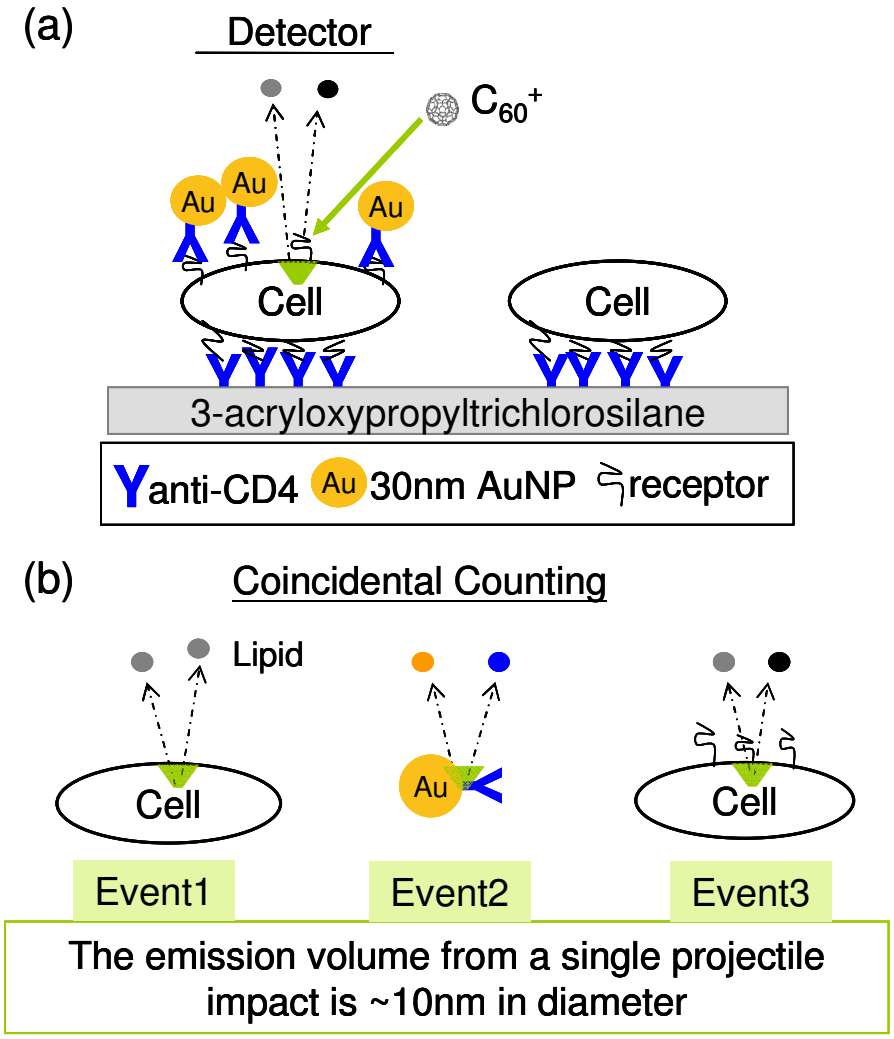

Figure IV-4 (a) Schematic illustration of C_{60}^{+} impacted on a AuNPs-antiCD4 labeled cell surface; (b) individual events records.

SIs were resolved from both antigen and cell lipid membrane area. All individual events are isolated and recorded at time and space that allows one to extract and construct coincidental mass spectrum with events of co-emitted ions with a selected ion.[25]

In the secondary ion mass spectrum, the Au adduct $AuCN^-$ at m/z 223, indicates the recombination of ions Au and CN from AuNP-antiCD4 within the impacted nanovolume. Figure IV-5(b) and (c) indicate the possibility of identifying amino acids related peaks for the antiCD4 when examining co-emitted ions with Au adducts, $AuCN^-$ (m/z 223) or Au^- (m/z 197). The co-emissions of Au adducts and amino acid SIs arises from the spatial co-location of antiCD4 and AuNPs. A further examination of co-emitted ions with a silane background peak at m/z 179 shows the absence of those amino acids peaks, confirming the specific identities of antiCD4 related ions (shown in Figure IV-5(d)). A peak at m/z 120 may be due to deprotonated cysteine suggesting the closeness of cysteine and AuNP recalling that the emission volume is $\leq 10^3$ nm^3 (shown in Figure IV-5(b) and (c)). In addition, the side chains corresponding to characteristic amino acid residues are observed in the coincidental spectra co-emitted with Au^-. Their proximity suggests that the binding sites for AuNPs on the antiCD4 are the sulfur-terminal cysteine and co-existing amino acid residues.

A similar result was obtained with the test case of AuNPs-antiCD4 deposited on a glass surface. The cumulative secondary ion spectrum and the mass spectrum of the coincidental secondary ions with $AuCN^-$ (at m/z 223) are shown in Figure IV-6. In Figure IV-6(a), the negative SI at m/z 120 may be attributed again to the deprotonated

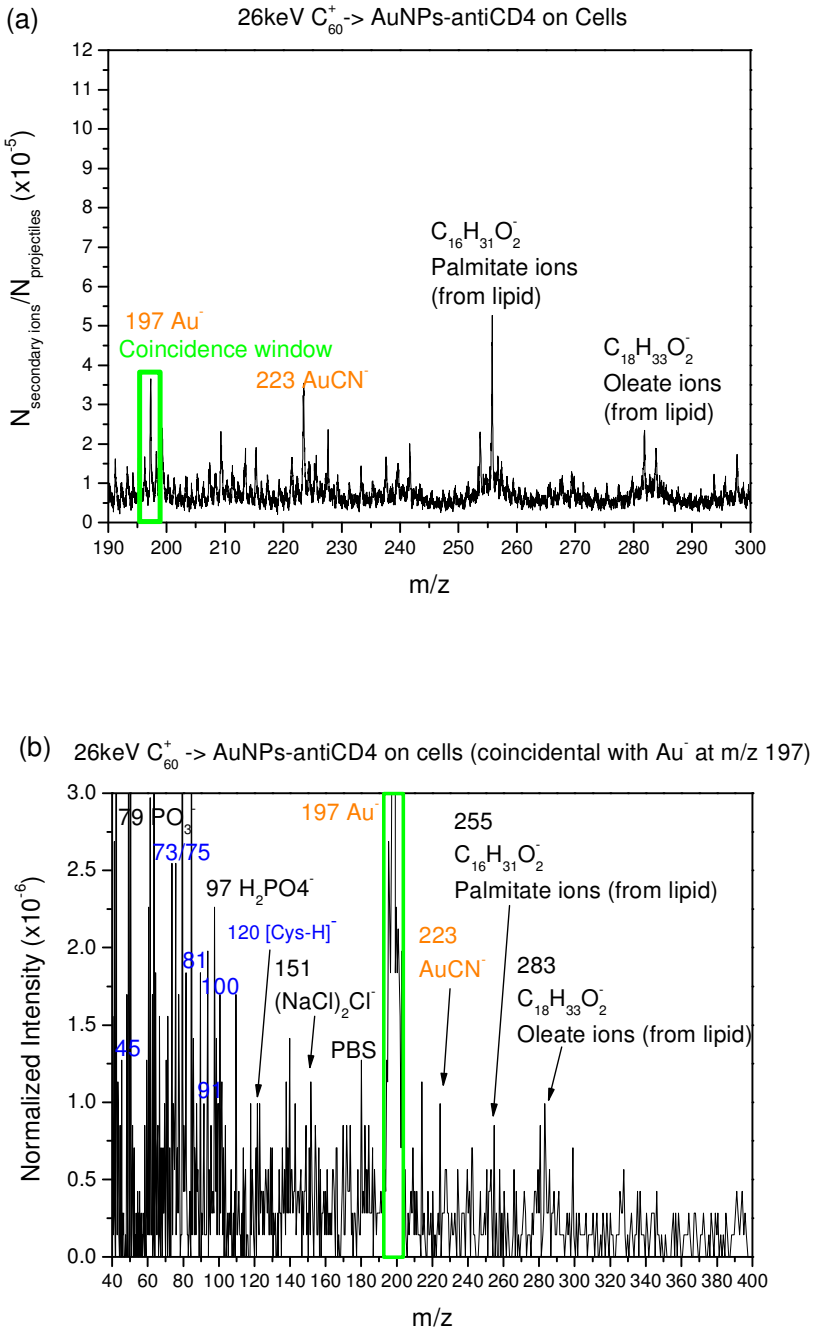

Figure IV-5 (a) Original secondary ion mass spectrum of AuNPs-antiCD4 labeled on Molt-3 cells; (b) Coincidental ion mass spectrum of co-emitted ions with Au^-; (c) Coincidental ion mass spectrum of co-emitted ions with $AuCN^-$ (m/z 223), inserted spectrum represents coincidental intensity of ion at m/z 120; (d) Coincidental ion mass spectrum of co-emitted ions with silane fragment at m/z 179.

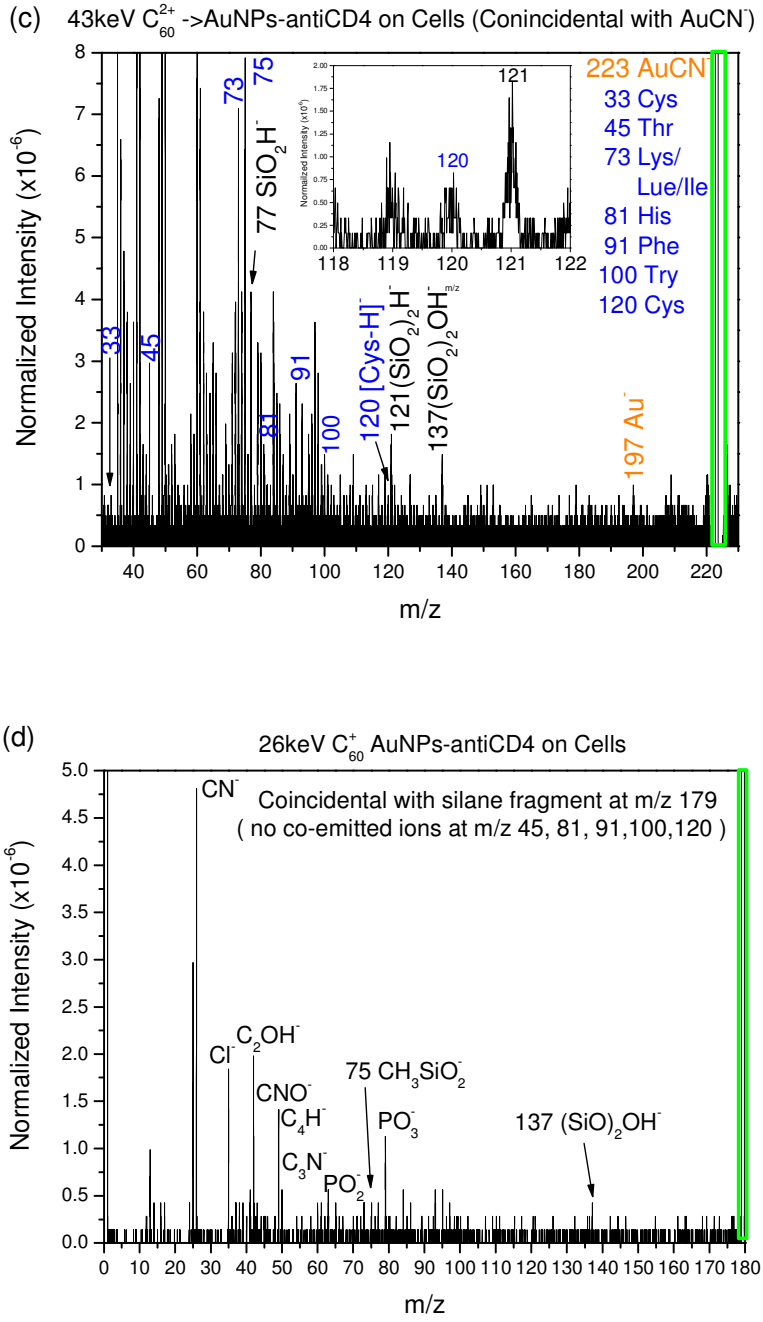

Figure IV-5 Continued

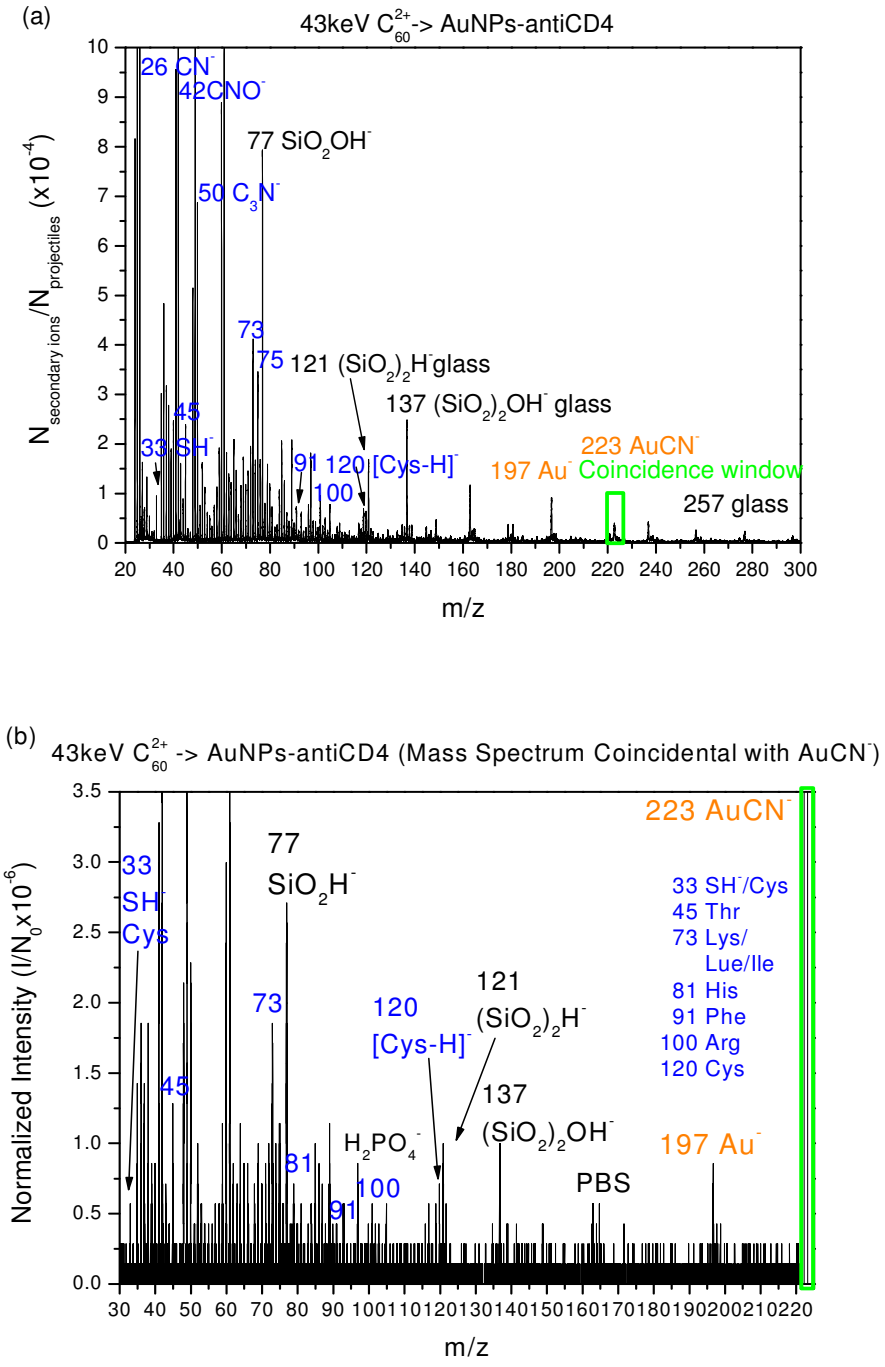

Figure IV-6 (a) Secondary ion mass spectrum of AuNPs-antiCD4 on glass impacted with 43 keV C_{60}^{2+} primary ions; (b) Coincidental ion mass spectrum of co-emitted ions with $AuCN^-$ (m/z 223) for AuNPs-antiCD4 on acrylated silane modified glass.

cysteine. The SIs co-emitted with $AuCN^-$ (m/z 223) are shown in Figure IV-6(b). Ions at m/z 30-100 are tentatively assigned to various amino acid residue side chains of antiCD4. SIs Au^- and $AuCN^-$ originate from AuNPs. The co-emitted SIs illustrates the feasibility of using coincidence ion mass spectrometry to probe the binding site of complexes conjugates.

c. Quantitative analysis of AuNPs-antiCD4 conjugates on cells

To identify the number of complex species on the cell surface we applied a methodology that has been previously described for determining the fractional coverage of immobilized biomolecules on micropatterned surfaces.[53] The fractional coverage is the ratio of the effective number of projectile impacts on a specified sampling area (N_e) to the total number of impacts (N_0) as described in chapter II (Eq. II-16) and the fractional coverage is calculated with the Eq. II-17.

As listed in Table IV-1 , we determined the fractional coverage of membrane lipid to be ~ 23% of the cell micropatterned surface using the co-emitted ions $C_{16}H_{31}O_2^-$ and $C_{18}H_{33}O_2^-$ from lipids. The fractional coverage of the AuNPs was found to be ~21% based on the co-emitted Au^- and $AuCN^-$ ions as shown in Figure IV-5(b). The AuNP coverage indicates the binding density of AuNPs labeled anti-CD4 on the cell receptor sites. The percentage of each specimen allowed us to calculate their densities in the sampling area. The sampling area is about 800 μm in diameter. Within this area, 21% of the patterned surface is covered with AuNPs-antiCD4 conjugates. It should be noted that the cell surface is partially covered by the 30 nm size AuNPs (Figure IV-4(a)), thus the effective impacts on the cell surface were reduced by the presence of AuNPs. Thus to

calculate the number of cells within the sampling area, the fractional coverage of AuNPs needed to be taken into account. As a result, the total cell coverage was found to be ~44% of the sampling area. The data corresponding to the number of cells or AuNPs are listed in Table IV-1. The number of cells in the sampling area was ~3430 while the number of AuNPs was 1.45×10^{8}. The resulting number of AuNPs per cell was about 42274 which is in a good agreement with the literature result measured by flow cytometry.[80-81]

Conclusion

This study illustrates the ability of SIMS in the individual impact mode to: a) validate the immobilization of AuNP labeled anti-CD4 on cell surfaces; b) quantify the coverage of molecules expressed on the cell surface. This method has several promising features for analysis of bio-nanomaterials and cells. Coincidence SIMS may be used to analyze nanoparticles that fall below the detection limit of standard electron microscopy, and should thus be applicable for studies on size dependent binding of nanoparticle-antibody conjugates.[29] As demonstrated by this work, SIMS may also be used to quantify the density of cell surface antigens. Beyond analysis of numbers, SIMS also provide chemical composition of the cell surface molecules and may in the future be used to analyze changes in composition (e.g. mutations) of cell surface receptors. We envision mass spectroscopy of cell surfaces to have future applications in cancer research, immunology and the study of infectious diseases.

Table IV-1 The quantitative results of AuNPs-antiCD4 on cell micropatterns.

Detected Species	Co-emitted Secondary Ions	Fractional Coverage	Numbers in Sampling Area
AuNPs-antiCD4 conjugates	Au^- and $AuCN^-$	21%	AuNPs~145 million
Cell lipid membrane	$C_{16}H_{31}O_2^-$ and $C_{18}H_{33}O_2^-$	23%	Cells~3430
Cell	Au + Lipid membrane	44%	AuNPs Per Cell~42274

CHAPTER V

QUANTITATIVE LABEL-FREE CHARACTERIZATION OF AVIDIN-BIOTIN ASSEMBLIES ON SILANIZED GLASS *

Introduction

The avidin-biotin interaction is one of the most common strategies for conjugating biomolecules like enzymes, antibodies or chemokines onto surfaces and carries high significance for cell/tissue engineering and biosensing applications.[82-86] Notably, the biotinylated molecules can be immobilized on a silanized surface and hence fashioned in micropatterns.[87-88] Our laboratories have been interested in employing silanized glass or indium tin oxide (ITO, or tin-doped indium oxide) substrates for cell micropatterning and immunosensor development.[54,59,80-81] In the past, we have relied on physical adsorption of antibodies in designing micropatterned immunoassays for cytokine detection; however, these immunosensors were insufficiently sensitive compared to standard enzyme linked immunosorbent assay (ELISA). We hypothesize that improvement in performance of these biosensors may be achieved by oriented attachment of antibodies onto surface via avidin-biotin interactions. In the present paper,

---

* Parts of this chapter were reprinted with permission from *Analytical Chemistry*, Volume 83, pages 7173-7178, Li-Jung Chen, Jeong Hyun Seo, Michael Eller, Stanislav V. Verkhoturov, Sunny S. Shah, Alexander Revzin, Emile A. Schweikert, "Quantitative label-free characterization of avidin-biotin assemblies on silanized glass." Copyright [2011] American Chemical Society.

we focus on characterizing the avidin layer assembled on glass as this layer represents an important building block in construction of biosensing surfaces.

Another important parameter investigated in this paper is the effect of silane composition on the quality/density of the assembled avidin-biotin layer. In the past, we have made extensive use of hydrogel micropatterning in designing surfaces for cell cultivation and biosensing.[79,89-90] In this micropatterning strategy, acrylated silanes are used for anchoring gel structures onto glass substrates. While providing an excellent coupling layer for gel attachment, acrylated silanes can only be used for physical and not covalent adsorption of biomolecules. One way to enhance functionality of the surface is to create a bifunctional silane layer containing end groups for gel and protein attachment.[91] The development of silanized surfaces for miropatterning of both proteins and hydrogels is the future goal. In the present paper, we compared avidin-biotin assembly on a bifunctional layer of amine- and acryl-terminated silane molecules to avidin-biotin attachment on monofunction silanes containing either acryl or amine terminal groups.

Relevant testing can be accomplished with fluorescent microscopy or imaging mass spectrometry where the avidin is either tagged with a dye or isotopically labeled.[40,87] We present here a label-free method for the quantification of the avidin-biotin complex and examine also its immobilization density vs. the silane functionality used for surface attachment. Our approach relies on time-of-flight secondary ion mass spectrometry, ToF-SIMS, with C_{60} as projectiles. The experiments are run in the event-by-event bombardment-detection mode, where the ionized ejecta from a single projectile

impact are recorded individually.[25,92] It has been shown experimentally and by molecular dynamics simulations that the impact of one C_{60} of a few tens of keV generates secondary ion (SI) emission from an area of ~ 10 nm in diameter and a depth of 5-10 nm.[60] To obtain statistically valid information on such a nanovolume, we run a sequence of single C_{60} impacts in stochastic fashion on a sampling area and, subsequently, compile the individual SI records and investigate similarities. The result is spatially refined molecular information in a nonimaging mode. The performance of event-by-event ToF-SIMS is illustrated below.

Experimental Section

a. Materials

Glass slides (75 × 25 mm^2) were obtained from VWR (West Chester, PA). (3-Acryloxypropyl) trimethoxysilane and N-(2-aminoethyl)-3-aminopropyl trimethoxysilane were purchased from Gelest, Inc. (Morisville, PA). 2-Hydroxy-2-methylpropiophenone (photoinitiator), dimethylsulfoxide (DMSO), and anhydrous toluene (99.9%) were purchased from Sigma-Aldrich (Saint Louis, MO). *N*-Hydroxysuccinimide (NHS)-dPEG®12-biotin was purchased from Quanta Biodesign, Ltd. (Powell, OH). NeutrAvidin® was purchased from Invitrogen (Carlsbad, CA).

b. Surface Preparation

The glass slides were immersed for 10 min into piranha solution (Caution: piranha solution is a vigorous oxidant, potentially explosive and should be used with proper protection equipment) consisting of a 1:1 ratio of 95% (v/v) and 35% (w/v) sulfuric acid. The glass slides were then thoroughly rinsed with deionized (DI) water, dried with

nitrogen, and stored under in class 10 000 cleanroom until further use. For silane modification, the glass slides were treated with oxygen plasma (YES-R3, San Jose, CA) at 300 W for 5 min and then immersed in silane solution. Three types of silanizations were performed; glass substrates were immersed in: (1) 0.1% v/v (3-acryloxypropyl) trimethoxysilane (acryl silane), (2) 0.1% v/v (2-aminoethyl)-3-aminopropyl trimethoxysilane (NH_2 silane), and (3) a mixture of (3-acryloxypropyl) trimethoxysilane and (2-aminoethyl)-3-aminopropyl trimethoxysilane prepared at 0.2% v/v. All silanes were prepared in anhydrous toluene and were reacted with surfaces for 5 h in a glovebag filled with nitrogen. After silanization reaction, slides were rinsed with fresh toluene, dried under nitrogen, and baked at 100 °C for 1 h. The silane-modified glass slides were stored in a desiccator before use.

As a first step in biofunctionalization, surfaces were treated in 250 mM NHS-dPEG12-biotin prepared in 1:1 mixture of DMSO and phosphate buffered saline (PBS) for 1 h, in which the NHS ester group can react with the surface NH_2 group by nucleophilic attack and produce a stable amide bond (-NH-CO-, Figure V-1(a))[93]. Subsequently, surfaces were rinsed with PBS buffer and distilled water to remove unreacted linker and then incubated in 1mg/mL of neutravidin for 1 h (neutravidin can easily interact with biotin on the surface, Figure V-1(b)).

c. Cluster $C_{60}^{1,2+}$ ToF-SIMS

The secondary ion mass spectrometry measurements were carried out with a custom-built secondary ion mass spectrometer coupled with time of flight mass analyzer (ToF-SIMS) with total impact energy on the target sample of 26 keV and 43 keV.[35,47,94]

As shown in Figure V-1, the size of the avidin-biotin complex is well suited for a chemical mapping study by using ToF-SIMS in the event-by-event bombardment/detection mode. The compound thickness of avidin-biotin and silanes layers was ~10-12 nm whereas the sampling depth of cluster ToF-SIMS was 5-10 nm (~10 nm in diameter hemispherical nanovolume).

SIMS analysis was used to characterize surface composition at each step in the surface modification: after silane assembly, biotin-PEG-NHS attachment and avidin conjugation. The first test case is the glass surface modified with an amino silane. Then the biotin with the functional group the $(PEG)_{12}$-NHS linker was immobilized on the amino silane with the leaving group succinimide NHS. Lastly, the avidin was immobilized on a biotin-$(PEG)_{12}$-NHS linker.

Results and Discussion

A key performance parameter in the biosensing application is the effect of silane composition on the density of the attached avidin-biotin complex. Figure V-2 shows the secondary ion mass spectra of biotin-$(PEG)_{12}$-NHS linker (biotin linker or BL) on amino silane (Figure V-2(a)) and avidin immobilized on a biotin-$(PEG)_{12}$- NHS modified amino silane (Figure V-2(b)), respectively. The mass spectra show that the negative ions at m/z 91 ($[CH_2C_6H_5]^-$, side chain of phenylalanine) and m/z 107 ($[CH_2C_6H_4OH]^-$, side chain of tyrosine) are distinct peaks for the avidin. The intensities of biotin-$(PEG)_{12}$-NHS characteristic ions found at m/z 183, 209, 211, 225, 267, 311, 325 and 339 decrease notably after the addition of avidin (Figure V-2(b)). As shown in the schematic Figure V-1(b), the lower yields of biotin-$(PEG)_{12}$-NHS peaks in the mass spectra are attributed

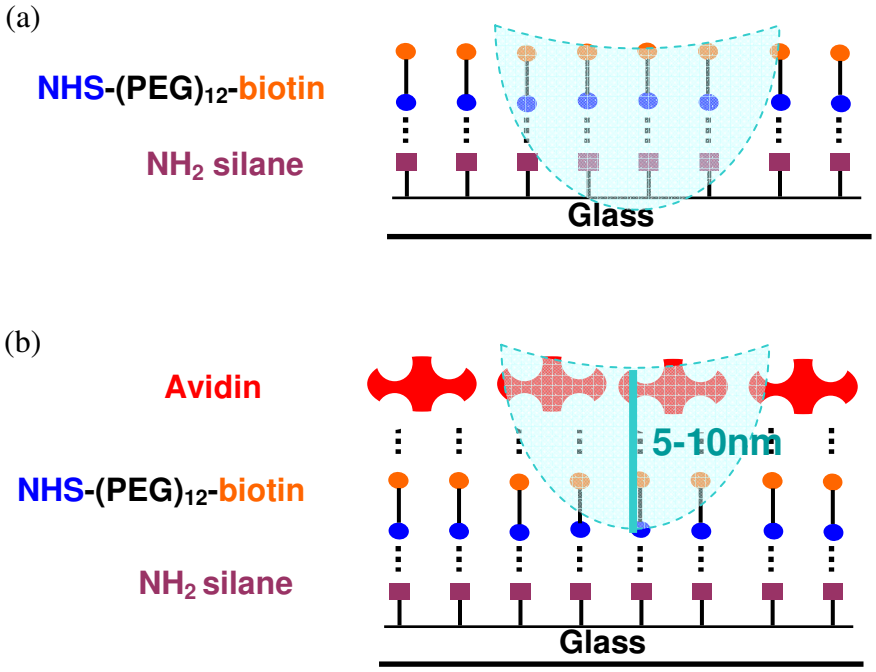

Figure V-1 Depth of emission of individual C_{60} projectiles impacts on: (a) NHS-$(PEG)_{12}$-biotin modified on NH_2 silane surface; (b) avidin immobilized on NHS-$(PEG)_{12}$-biotin modified NH_2 silane surface.

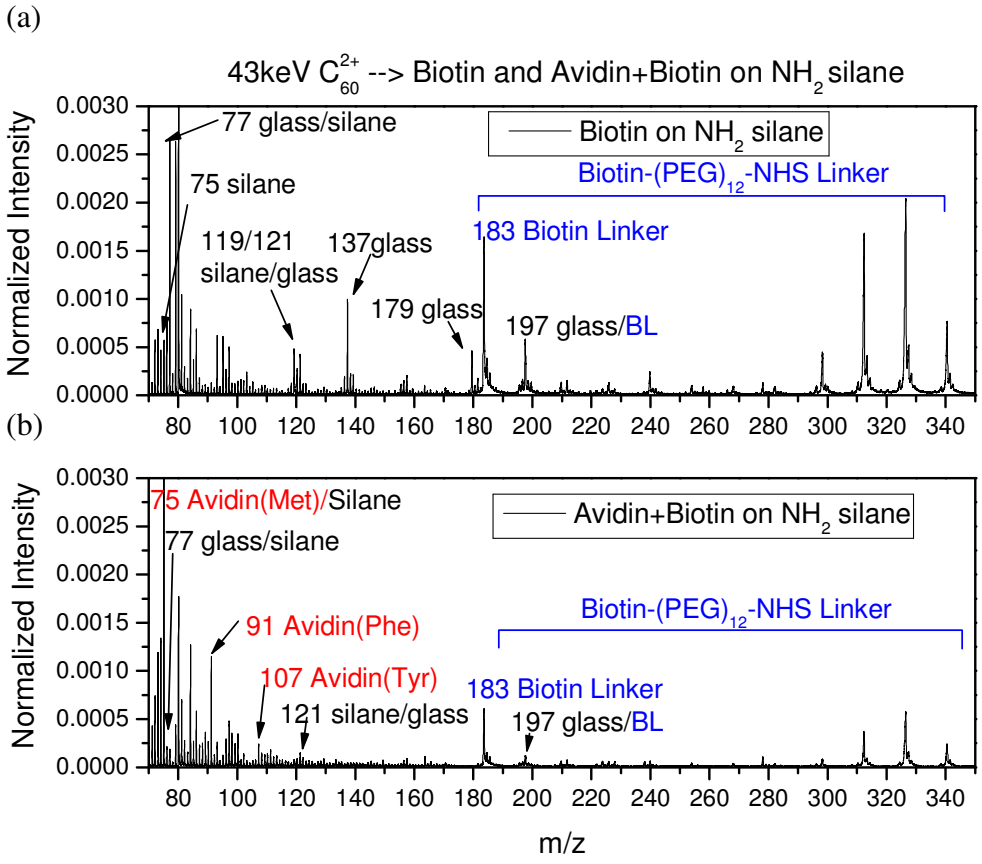

Figure V-2 Secondary ion mass spectra: (a) biotin immobilized on the amino silane modified glass surface; (b) avidin attached on the biotin immobilized amino silane modified glass surface.

to the thick layer of avidin (5-7nm), which reduces secondary ion emission from the underlying biotin-$(PEG)_{12}$-NHS layer.

In addition, Figure V-2(b) shows lower glass and silane-related peaks at m/z 77 $(SiO_2)OH^-$, 121 $(SiO_2)_2H^-$, 137 $(SiO_2)_2OH^-$, and 197 $(SiO_2)_3OH^-$. After adding avidin, the low glass-related signals indicate that the entire surface was covered with avidin, thus reducing emission of SI from the underlying glass substrate. In contrast, Figure V-1(a) shows that the thickness of biotin and silane layers is smaller than the depth of projectile impact which resulted in the higher intensities of biotin, silane, and glass correlated peaks.

The data can be assessed in a quantitative manner with the SI yield, $Y_A(\%)$ which is described in the Eq. II-10 of Chapter II. Table V-1 lists the SI yields of characteristic fragments for avidin and biotin complexes on various silanes. The doubly charged C_{60} (total energy 43 keV) shows significantly higher yields than the singly charged C_{60} (total energy 26 keV).[33] The higher molecular ion yields facilitate the identification of specific ions from bio-complexes. In particular, they enhance the coincidental secondary ion signals and hence the higher probability of co-emission of secondary ions with a selected ion.

The SI yields for the avidin-related fragment ions at m/z 91 and 107 are listed for the assemblies immobilized with different silanes (Table V-1). The corresponding mass spectra (Figure V-3) show that the abundance of the fragment ions of the phenylalanine (Phe) and tyrosine (Tyr) correlates with that of the glass-related signals. Lower substrate signals (Figure V-3) signify better covalent binding between NH_2 silane and biotin-

Table V-1 SI yields (%) of avidin+ biotin on various silanes run with 26 keV C_{60}^{+} and 43 keV C_{60}^{+2} bombardment

43 keV C_{60}^{2+} Avidin Biotin on Various Silanes			
m/z	NH_2 Silane	Acryl Silane	Mixed NH_2&Acry
26	35.8	42.4	26.3
42	14.6	15.0	10.3
50	6.8	8.0	5.0
75	5.2	4.0	3.5
77	0.6	0.9	0.6
91	1.9	1.5	1.3
107	0.5	0.3	0.3
121	0.4	0.5	0.4
137	0.1	0.5	0.1
183	2.2	0.8	3.2
311	1.4	0.8	1.7

26 keV C_{60}^{+} Avidin Biotin on Various Silanes				
m/z	NH_2 Silane	Acryl Silane	Mixed NH_2&Acry	Avidin Glass
26	8.3	12.5	7.0	6.8
42	5.1	5.5	3.3	3.9
50	1.1	1.9	0.9	0.9
75	0.7	1.3	0.3	0.6
77	0.1	0.2	0.3	0.2
91	0.4	0.6	0.2	0.4
107	0.1	0.2	0.1	0.2
121	0.1	0.1	0.1	0.1
137	<0.1	0.1	0.1	0.1
183	0.4	0.2	1.0	--
311	0.3	0.1	0.8	--

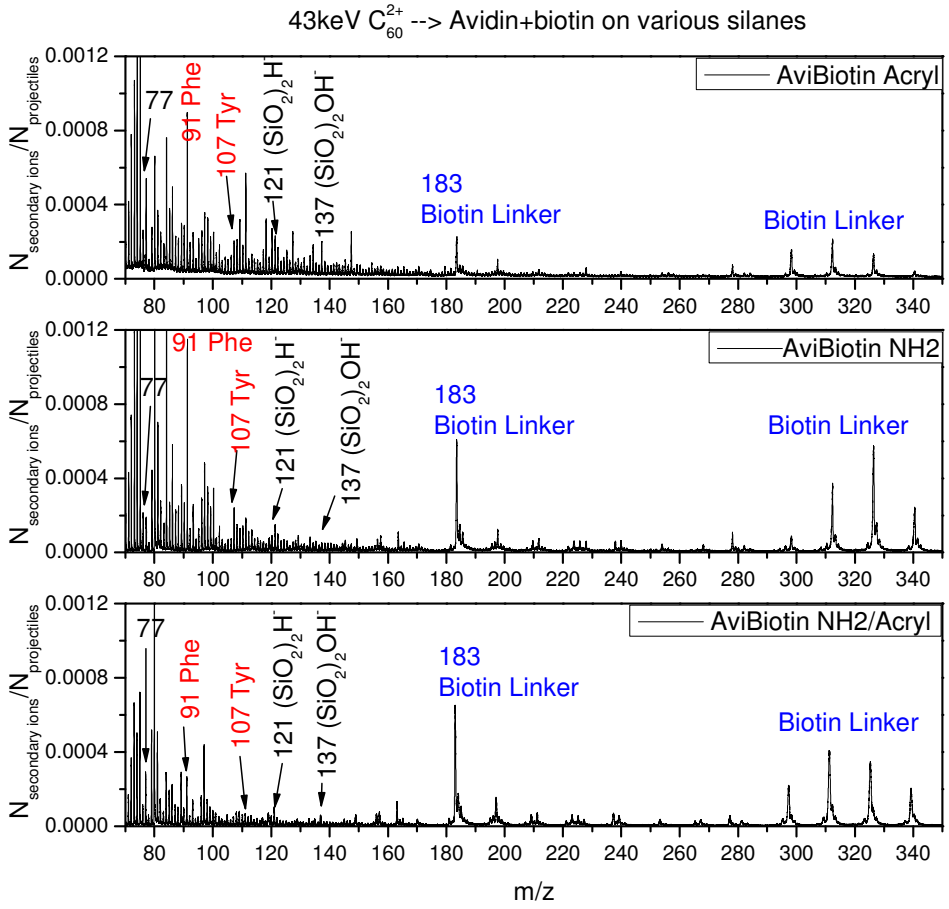

Figure V-3 Secondary ion mass spectra of avidin and biotin linker attached, respectively, on acryl, amino, and amino/acryl mixed silanes.

$(PEG)_{12}$-NHS that yields higher avidin intensity. A more reactive NH_2 silane and biotin-$(PEG)_{12}$-NHS interface thus provides a better binding performance with avidin.

The low intensity of glass/silane fragments (Figure V-3) in the mass spectrum of NH_2 silane case is attributed to the small amount of avidin defects on the entire surface. The reactivity variation by the types of silanes influences the biotin immobilization performance between silanes and biotin. In both test cases of avidin and biotin immobilized on acryl silane and mixed (acryl and NH_2) silane, the higher signals of glass-related peaks at m/z 121 $(SiO_2)_2H^-$ and 137 $(SiO_2)_2OH^-$ indicate a large amount of defects in avidin immobilization resulting in the enhanced possibility of SI emission from the substrate. Also, in the test case of acrylated silane, signals corresponding to the biotin-$(PEG)_{12}$-NHS fragments at m/z 183 and 311, 325, and 339 are lower than those on NH_2 and mixed (NH_2 and acrylated) silanes. This observation is reasonable given the higher density of NH_2 groups available in the monofunctional silane layer for reaction with NHS moieties on biotin. In contrast, interaction of biotin-$(PEG)_{12}$-NHS with acrylated silane resulted in a weak signal suggesting that only a limited number of biotins were physically bound on this silane layer. Subsequent incubation of the surface with avidin resulted in a low protein signal. These studies highlight the benefits of covalent attachment in creating a dense avidin layer on the surface.

However, the relative SI yields cannot be directly correlated with the degree of surface coverage because of the inhomogeneous surfaces as sketched in Figure V-4. The irregular coverage of avidin and biotin results in unequal impacts/emissions from the same sample. Table V-1 shows similar yields in avidin (at m/z 91 and 107) for all test

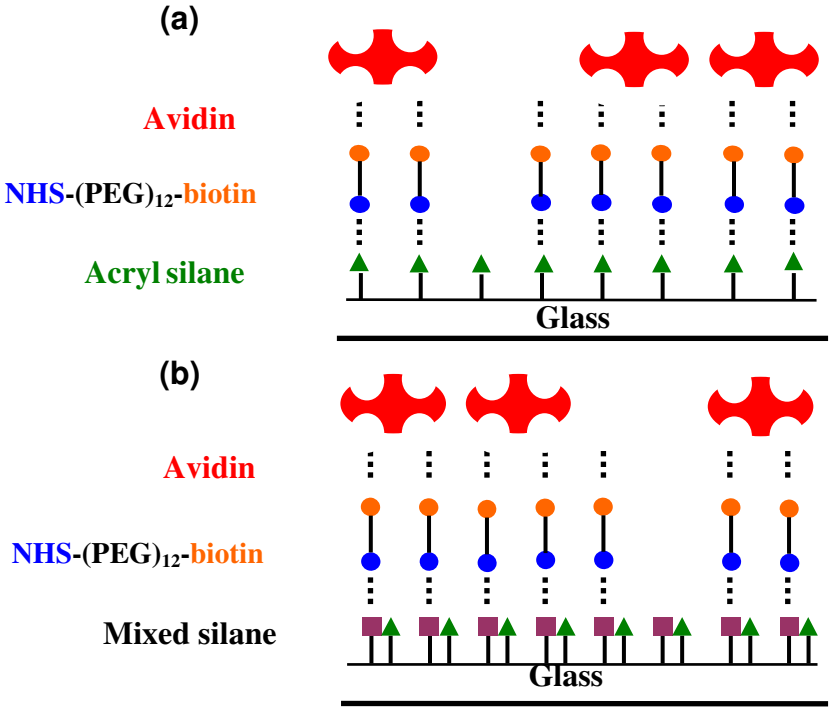

Figure V-4 Schematic of irregular coating of avidin and biotin on: (a) acryl silanized glass surface; (b) mixed (acryl and amino silanes) silanized surface.

cases. The apparent higher yields at m/z 137 (glass), 183 and 311 (biotin-$(PEG)_{12}$-NHS) of the avidin biotin on acrylated silane implicate the presence of avidin defects.

The SI yields provide a rough comparison of the attachment of the complexes. A quantitative method for determining their binding densities which takes into account the fractional coverage of the immobilized amounts of avidin and biotin is described below.

As noted at the outset, the event-by-event ToF-SIMS method allows one to select a specific ion and to identify the coemitted SIs which originate from molecules colocated in the nanovolume with the selected ion. Figure V-5 show the secondary ions co-emitted with m/z 422 from the biotin-$(PEG)_{12}$-NHS linker and hence the molecular ions colocated in the nano-domain. Peaks related to the biotin-$(PEG)_{12}$-NHS linker at m/z 183 and 325 were both observed (Figure V-5(a) and (b)). In comparison, Figure V-5(b) shows the characteristic peaks of avidin at m/z 91 (Phe) and 107 (Tyr).

The absence of glass-related peaks at m/z 121 $(SiO_2)_2H^-$ and 137 $(SiO_2)_2OH^-$ (seen in Figure V-5(b)) indicates that the layers of avidin (5-7 nm) and biotin-$(PEG)_{12}$-NHS linker (~5 nm) limit the SI emission from the underlying glass substrate. It may be recalled that the emission nanovolume of secondary ions is about 5-10 nm in depth. Thus, the majority of chemical signals shown in Figure V-5(b) are from avidin and biotin conjugates. Nevertheless, the inhomogeneous surface generates various types of projectile impacts/emissions. Thus, the single coincidence spectrum of ions coemitted with m/z 422 may contain ions at m/z 75 from both avidin and silane. Figure V-6 sketches the types of impacts on a complex surface. Overlapping ions at m/z 75 can be resolved via double coincidence, i.e., by selecting events of coemission of specific ions

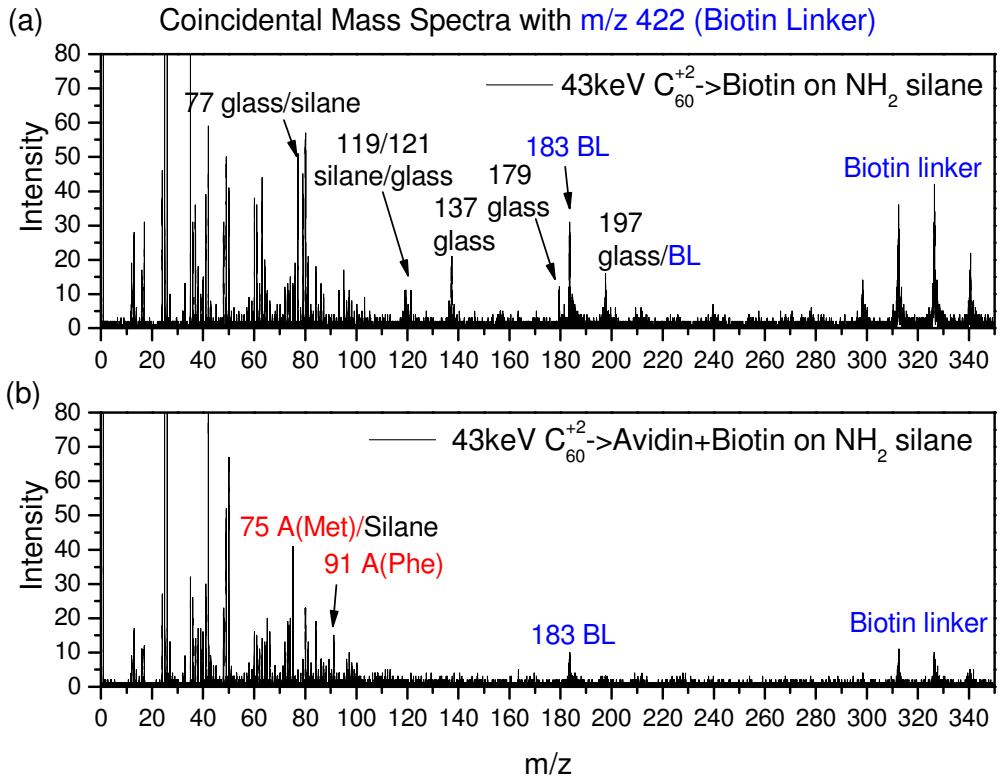

Figure V-5 Coincidental spectra with coemitted secondary ions with ion at m/z 422 from biotin-$(PEG)_{12}$-NHS linker. (a) Biotin-$(PEG)_{12}$-NHS on NH_2 silane; (b) Avidin+biotin-$(PEG)_{12}$-NHS on NH_2 silane.

from avidin and biotin.[95]

Figure V-7 shows the comparison of single coincidence and double coincidence ion mass spectra. In the double coincidence spectrum, the ratio of the peaks at m/z 75 and 74 is lower than that in the single coincidence spectrum and original mass spectrum. Secondary ions at m/z 75 could originate from both silane ($CH_3SiO_2^-$) and avidin (Methionine, Met), respectively. Two coincidence windows were set with ions from biotin-$(PEG)_{12}$-NHS at m/z 183 and avidin at m/z 91 (Figure V-7(b)). Only those ions coemitted with both ions at m/z 183 and 91 can be present in the double coincidence spectrum; impacts yielding interfering ions at m/z 75 from silane were eliminated. Other interfering ions at m/z 197 observed in original mass spectra were determined as ions related to both biotin-$(PEG)_{12}$-NHS linker and glass. The double coincidence methodology with coemitted ions of avidin and biotin layer has removed the interfering glass-related peaks. The double coincidental ion mass spectra arise for a specific chemical distribution of the ligand and protein molecules residing on the topmost layer of the biointerface. The event-by-event bombardment/detection mode allows one to deconvolute signals emanating from complex inhomogeneous biointerfaces and to extract a spatially distributed mass spectrum originating from avidin and biotin conjugates.

A further application of the coincidence mode is to quantify the fractional surface coverage of avidin. As described above, differences in silane composition affect attachment of the biotin-$(PEG)_{12}$-NHS molecules, and ultimately determine the quality of the topmost avidin layer. We noted earlier the absence of glass-related peaks in the

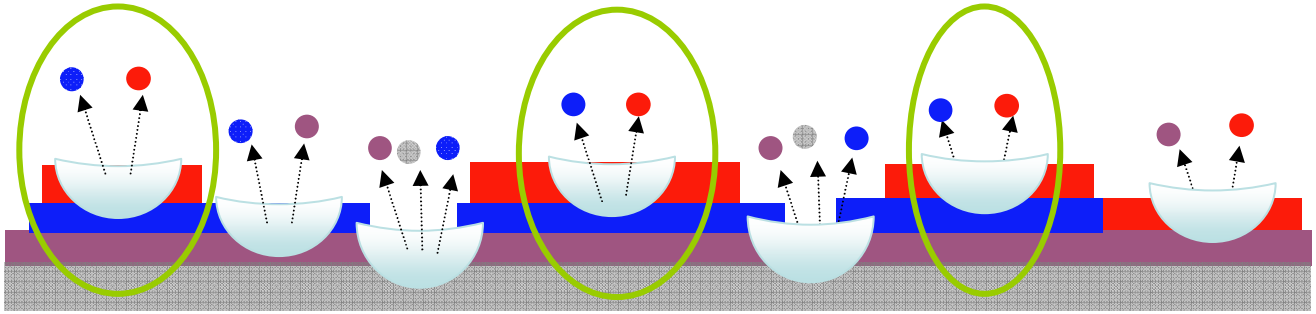

Figure V-6 Diagram of coemitted secondary ions from an avidin+biotin-$(PEG)_{12}$-NHS+NH_2 silane on glass surface. (Red: avidin; blue: biotin-$(PEG)_{12}$-NHS; purple: NH_2 silane; gray: glass)

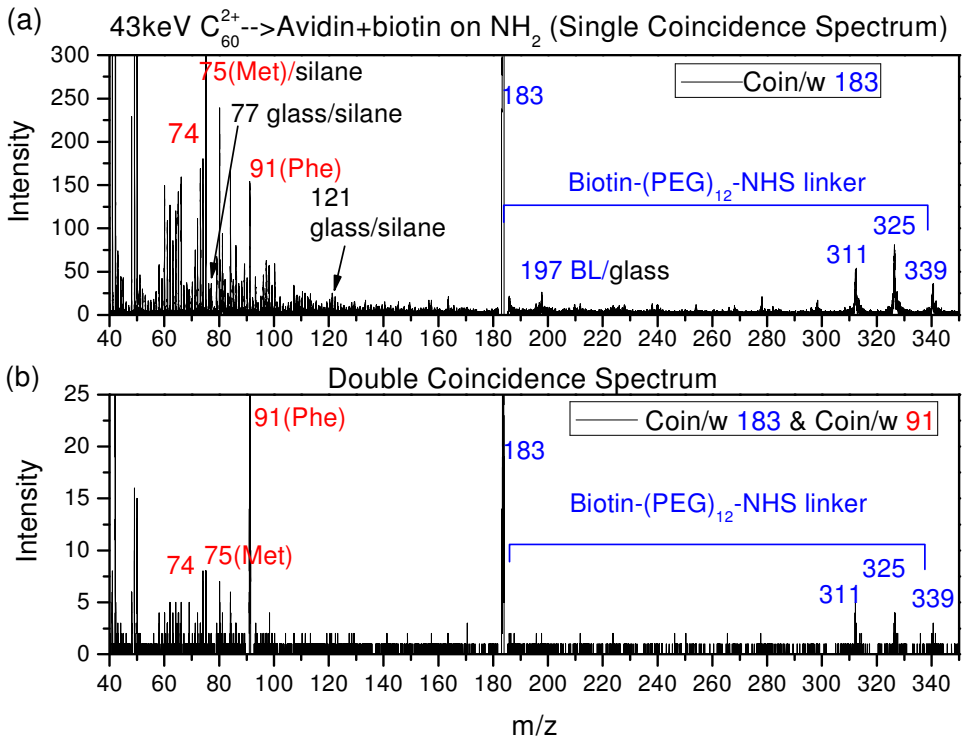

Figure V-7(a) Single coincidental ion mass spectrum with ion at m/z 183 from the biotin-$(PEG)_{12}$-NHS linker of sample avidin+biotin linker on NH_2 silane. (b) Double coincidental ion mass spectrum with two selected coincidental ions at m/z 183 (biotin linker) and m/z 91 (avidin) originate from sample avidin + biotin linker on NH_2 silane.

NH_2 silane and the presence of prominent glass peaks in acrylated silane, suggesting different degrees of immobilization for avidin. The hypothesis is that the avidin coverage on the NH_2 silane is greater than acrylated silane. The ability to test the avidin surface density will in turn allow us to assess the quality and quantity of protein immobilization.

The surface density can be expressed as the fractional coverage, which is computed from the ratio between the numbers of effective impacts on an immobilized specimen to that of total primary ions sent to bombard a target surface.[29-30] The derivation of the number of effective impacts is described in the following paragraphs.

The fractional coverage $K(\%)$ of a specimen can be obtained as the number of effective impacts (N_{eff}) divided by the total number of projectile sent to bombard on the sample target (N_0) as described in the Eq. II-17 of Chapter II. In the present case, two coemitted secondary ions are used to calculate the effective number of impacts on either biotin-$(PEG)_{12}$-NHS linker or avidin (Eq. II-16 in Chapter II). For example, the coincidental intensity of ions at m/z 183 and 325 from biotin and ions at m/z 91 coemitted with ions at m/z 107 from avidin were used. The fractional surface coverage $K(\%)$ is calculated using Eq. II-17 (seen in Chapter II).

Table V-2 lists the quantitative results of the degree of biotin-$(PEG)_{12}$-NHS and avidin densities of immobilization on various silanes. An immobilization density of ~82% was obtained for the biotin-$(PEG)_{12}$-NHS linker on NH_2 silanes. The corresponding numbers are 83% for the mixed (NH_2 and acryl) silane and 61% for the acryl silane. Interestingly, the density of avidin attachment on NH_2 silane is ~100%. We noted earlier the absence of glass-related peaks in these samples, indeed due to the high

avidin immobilization density. In the test case of acryl silane, the avidin density is of ~39% while it is ~54% for mixed silanes. The low degree of avidin attachment on acryl silane may be explained by the lower density of biotin molecules mentioned earlier but also by the disoriented physical adsorption of these molecules which makes for less effective avidin-biotin conjugation. As shown by our data, mixed silanes containing acrylate and amine functionalities had intermediate coverage of avidin suggesting once again that covalent attachment to amine moieties is an important determinant of the quality of the avidin layer.

Tests with biotin-$(PEG)_{12}$-NHS only on various silanes gave similar results from the acrylated silane. Only 22% of biotin linker was attached on the acrylated silane functionalized surface whereas the biotin binding densities were of 84% and 82% for the NH_2 and mixed silane, respectively.

In addition, we compared the binding density of avidin on different silanes as listed in the last column (Table V-2). While avidin attached on the silanized surface without a biotin linker, it shows better attachment with NH_2 silanes in comparison to acrylated and mixed silanes. Nevertheless, the avidin densities are lower than those mediated with the biotin linker. The quantitative results demonstrate the importance of the biotin linker in the layer-by-layer assemblies. Also, various functionalities of silanes influence the biotin linker binding performance that changes the binding densities of attached avidin.

Conclusion

This work shows the feasibility of applying cluster C_{60} ToF-SIMS with the event-by-event bombardment/detection mode to differentiate the characteristic peaks for intact

avidin-biotin complex. The qualitative information shows the effect of novel bifunctional silanes on the density of avidin-biotin immobilization. The double coincidence enhances the accuracy of identifying distinct peaks of avidin-biotin biointerface. Also, the capability of quantifying the biocomplexes enables to evaluate the effect of various silane compositions on the density of avidin-biotin attachment. This label-free mass spectrometric methodology offers both qualitative and quantitative means of investigating the amounts of biomolecules immobilized on silanized surfaces. The double coincidence label-free detection might further contribute to ToF-SIMS imaging of avidin-biotin complexes.

Table V-2 The comparison of the binding densities of complex from samples: avidin with biotin-$(PEG)_{12}$-NHS linker, biotin-$(PEG)_{12}$-NHS linker, and avidin on various silanes.

Samples / Silanes	Avidin + Biotin Linker on various silanes		Biotin linker on silanes	Avidin on silanes
	Biotin Linker Density (183,325)	Avidin Density (107,91)	Biotin Linker Density (183,325)	Avidin Density (107,91)
NH_2 Silane	82%	100%	84%	61%
Acryl Silane	61%	39%	22%	54%
Mixed Silane (NH_2: Acryl=1:1)	83%	54%	82%	44%

CHAPTER VI

CONCLUSIONS

The goal of this work was to develop cluster-secondary ion mass spectrometry (SIMS) for the quantification of complex biological surfaces. The operation of cluster-SIMS in the event-by-event bombardment/detection mode allows the examination of secondary ion (SI) co-emissions recorded from each individual projectile impact. The feasibility to reveal co-localized molecules within nanodomians of single projectile impacts facilitates the development of cluster-SIMS quantitative methodology. The use of efficient cluster projectiles with high impact energy (43 keV C_{60}^{2+} and 520 keV Au_{400}^{4+}) enhances SI emission and molecular ions, reduces fragmentation of molecular ions, and lowers the damage cross-section compared to bombardment with atomic primary ions or primary ions with lower impact energy.

The experimental values of the symmetrically prepared microstrips were compared with theoretical ones. The event-by-event cluster-SIMS allowed the quantification of micropatterns with a sensitivity corresponding to few nanometers. The ability to determine the quantity of incubated biomolecules on the micropatterns provided a means to evaluate the quality of micropatterns and hence establish a suitable manufacturing process for immobilization of molecules.

The quantitation process was also applied for measuring the number of antibody-Au nanoparticle (AuNP) conjugates on a cell. The number of specific attachment of antiCD4 to the antigen reflects a disease-related progress or status. Limitations arise in the SEM

imaging of small sizes of nanoparticles labeled/attached in the biological system. Our approach provides an alternative and complement to SEM imaging as demonstrated with the determination of the number of antiCD4-AuNPs per cell.

The ability to identify analyte-specific ions and co-emissions of those, provides the basis for a label-free approach for quantifying the fractional coverage of analytes. The methodology was validated with a study of the avidin-biotin interface. The quantification of stepwise prepared biointerfaces revealed the fractional coverage as a function of the compositions of silane substrates.

The novel concept of the double coincidence mass spectrometry was demonstrated with the inspection of co-emissions from avidin and biotin layers. The result showed that the background signals from the underlying substrate could be eliminated. The feasibility to extract a specific stratum of the two biotin-avidin layers was demonstrated. This methodology contributes to enhance the accuracy of SI identification and the quality of analytical information for mass spectrometry.

The ultimate limits of quantitative nanoscale surface characterization with cluster-SIMS in the event-by-event bombardment/detection mode remain to be explored. Put differently, at what size of a NP, is the quantitative methodology demonstrated in this study no longer applicable?

Indeed, at some point, the emission volume from a single impact will be larger than the size of nano-object. We don't at present know the emission volume, thus we will need first to assess this parameter as a function of projectile and target characterization. Pertinent data are a prerequisite for adapting the quantitative methodology for the

accurate assay of nano-object and –domain of a few nm. Such methodology will also be critical for studying the chemical composition of nanometric interfaces. At issue is a more refined understanding of the physical-chemical processes operating in the hypervelocity particle-solid interaction. Many experimental challenges remain, foremost high resolution, localization of individual projectile impacts, and highly sensitive detection as well as highly accurate identification of ionized ejecta.

REFERENCES

(1) Evans Analytical Group: Sunnyvale, CA, 2011, p (Reprinted permission date: Feb.11 2011).

(2) Bearinger, J. P.; Stone, G.; Christian, A. T.; Dugan, L.; Hiddessen, A. L.; Wu, K. J. J.; Wu, L.; Hamilton, J.; Stockton, C.; Hubbell, J. A. *Langmuir* **2008**, *24*, 5179.

(3) Cheng, F.; Gamble, L. J.; Castner, D. G. *Analytical Chemistry* **2008**, *80*, 2564.

(4) Zhou, C.; Qi, K.; Wooley, K. L.; Walker, A. V. *Colloids and Surfaces B-Biointerfaces* **2008**, *65*, 85.

(5) Gronlund, F.; Moore, W. J. *Journal of Chemical Physics* **1960**, *32*, 1540.

(6) Rol, P. K.; Fluit, J. M.; Kistemaker, J. *Physica* **1960**, *26*, 1000.

(7) Appelhans, A. D.; Delmore, J. E. *Analytical Chemistry* **1989**, *61*, 1087.

(8) Blain, M. G.; Dellanegra, S.; Joret, H.; Lebeyec, Y.; Schweikert, E. A. *Physical Review Letters* **1989**, *63*, 1625.

(9) Wucher, A. *Applied Surface Science* **2006**, *252*, 6482.

(10) VanStipdonk, M. J.; Harris, R. D.; Schweikert, E. A. *Rapid Communications in Mass Spectrometry* **1996**, *10*, 1987.

(11) Wong, S. C. C.; Hill, R.; Blenkinsopp, P.; Lockyer, N. P.; Weibel, D. E.; Vickerman, J. C. *Applied Surface Science* **2003**, *203*, 219.

(12) Weibel, D.; Wong, S.; Lockyer, N.; Blenkinsopp, P.; Hill, R.; Vickerman, J. C. *Analytical Chemistry* **2003**, *75*, 1754.

(13) Verkhoturov, S. V.; Rickman, R. D.; Guillemier, C.; Hager, G. J.; Locklear, J. E.; Schweikert, E. A. *Applied Surface Science* **2006**, *252*, 6490.

(14) Locklear, J. E.; Guillermier, C.; Verkhoturov, S. V.; Schweikert, E. A. *Applied Surface Science* **2006**, *252*, 6624.

(15) Tempez, A.; Schultz, J. A.; Della-Negra, S.; Depauw, J.; Jacquet, D.; Novikov, A.; Lebeyec, Y.; Pautrat, M.; Caroff, M.; Ugarov, M.; Bensaoula, H.; Gonin, M.; Fuhrer, K.; Woods, A. *Rapid Commun Mass Sp* **2004**, *18*, 371.

(16) Bouneau, S.; Della-Negra, S.; Depauw, J.; Jacquet, D.; Le Beyec, Y.; Mouffron, J. P.; Novikov, A.; Pautrat, M. *Nucl Instrum Meth B* **2004**, *225*, 579.

(17) Fernandez-Lima, F. A.; Post, J.; DeBord, J. D.; Eller, M. J.; Verkhoturov, S. V.; Della-Negra, S.; Woods, A. S.; Schweikert, E. A. *Anal Chem* **2011**.

(18) Dellanegra, S.; Jacquet, D.; Lorthiois, I.; Lebeyec, Y.; Becker, O.; Wien, K. *International Journal of Mass Spectrometry and Ion Processes* **1983**, *53*, 215.

(19) Rademann, K. *Berichte Der Bunsen-Gesellschaft-Physical Chemistry Chemical Physics* **1989**, *93*, 653.

(20) Masuoka, T.; Koyano, I. *Journal of Chemical Physics* **1991**, *95*, 909.

(21) Imamura, T.; Brion, C. E.; Koyano, I.; Ibuki, T.; Masuoka, T. *Journal of Chemical Physics* **1991**, *94*, 4936.

(22) Zha, Q. M.; Nishimura, T.; Bertrand, M. J.; Meisels, G. G. *International Journal of Mass Spectrometry and Ion Processes* **1991**, *107*, 515.

(23) Thissen, R.; Hubinfranskin, M. J.; Furlan, M.; Piette, J. L.; Morin, P.; Nenner, I. *Chemical Physics Letters* **1992**, *199*, 102.

(24) Masuoka, T.; Doi, H. *Physical Review A* **1993**, *47*, 278.

(25) Park, M. A.; Gibson, K. A.; Quinones, L.; Schweikert, E. A. *Science* **1990**, *248*, 988.

(26) Rickman, R. D.; Verkhoturov, S. V.; Parilis, E. S.; Schweikert, E. A. *Physical Review Letters* **2004**, *92*.

(27) Guillermier, C.; Della-Negra, S.; Schweikert, E. A.; Dunlop, A.; Rizza, G. *Int J Mass Spectrom* **2008**, *275*, 86.

(28) Schenkel, T.; Wu, K. J. *Int J Mass Spectrom* **2003**, *229*, 47.

(29) Raiagopalachary, S.; Verkhoturov, S. V.; Schweikert, E. A. *Analytical Chemistry* **2009**, *81*, 1089.

(30) Pinnick, V. T.; Verkhoturov, S. V.; Kaledin, L.; Bisrat, Y.; Schweikert, E. A. *Anal Chem* **2009**, *81*, 7527.

(31) Pinnick, V.; Rajagopalachary, S.; Verkhoturov, S. V.; Kaledin, L.; Schweikert, E. A. *Analytical Chemistry* **2008**, *80*, 9052.

(32) Rajagopalachary, S.; Verkhoturov, S. V.; Schweikert, E. A. *Nano Lett.* **2008**, *8*, 1076.

(33) Fernandez-Lima, F. A.; Eller, M. J.; Verkhoturov, S. V.; Della-Negra, S.; Schweikert, E. A. *Journal of Physical Chemistry Letters* **2010**, *1*, 3510.

(34) Eller, M. J.; Verkhoturov, S. V.; Della-Negra, S.; Schweikert, E. A. *Journal of Physical Chemistry C* **2010**, *114*, 17191.

(35) Verkhoturov, S. V.; Eller, M. J.; Rickman, R. D.; Della-Negra, S.; Schweikert, E. A. *Journal of Physical Chemistry C* **2010**, *114*, 5637.

(36) Simon, M.; Lebrun, T.; Martins, R.; Desouza, G. G. B.; Nenner, I.; Lavollee, M.; Morin, P. *Journal of Physical Chemistry* **1993**, *97*, 5228.

(37) Lee, C. Y.; Harbers, G. M.; Grainger, D. W.; Gamble, L. J.; Castner, D. G. *Journal of the American Chemical Society* **2007**, *129*, 9429.

(38) Hainfeld, J. F. *Science* **1987**, *236*, 450.

(39) Jung, L. S.; Nelson, K. E.; Stayton, P. S.; Campbell, C. T. *Langmuir* **2000**, *16*, 9421.

(40) Belu, A. M.; Yang, Z. P.; Aslami, R.; Chilkoti, A. *Analytical Chemistry* **2001**, *73*, 143.

(41) Hainfeld, J. F. *Ultramicroscopy* **1992**, *46*, 135.

(42) Hainfeld, J. F.; Foley, C. J.; Maelia, L. E.; Lipka, J. J. *J. Histochem. Cytochem.* **1990**, *38*, 1787.

(43) Lee, C. Y.; Gong, P.; Harbers, G. M.; Grainger, D. W.; Castner, D. G.; Gamble, L. J. *Analytical Chemistry* **2006**, *78*, 3316.

(44) May, C. J.; Canavan, H. E.; Castner, D. G. *Analytical Chemistry* **2004**, *76*, 1114.

(45) Kim, Y. P.; Hong, M. Y.; Shon, H. K.; Chegal, W.; Cho, H. M.; Moon, D. W.; Kim, H. S.; Lee, T. G. *Applied Surface Science* **2008**, *255*, 1110.

(46) DeBord, J. D., Personal communication with DeBord. Schematic illustration of Au-LMIS instrument is reprinted with permission from DeBord, 2011.

(47) Locklear, J. E. *Ph. D. Dissertation,Chemistry, Texas A&M University, College Station, TX* **2006**.

(48) Li, Z. *Ph. D. Dissertation,Chemistry, Texas A&M University, College Station, TX* **2007**.

(49) Wiza, J. L. *Nucl Instrum Methods* **1979**, *162*, 587.

(50) Rickman, R. D. *Ph. D. Dissertation,Chemistry, Texas A&M University, College Station, TX* **2004**.

(51) Knoll, G. F. *Radiation Detection and Measurement*; 2nd ed. ed.; Wiley: New York, 1989.

(52) Li, Z.; Verkhoturov, S. V.; Schweikert, E. A. *Analytical Chemistry* **2006**, *78*, 7410.

(53) Chen, L.-J.; Shah, S. S.; Verkhoturov, S. V.; Revzin, A.; Schweikert, E. A. *Surface and Interface Analysis* **2011**, *43*, 555.

(54) West, J.; Becker, M.; Tombrink, S.; Manz, A. *Anal. Chem.* **2008**, *80*, 4403.

(55) Vilkner, T.; Janasek, D.; Manz, A. *Analytical Chemistry* **2004**, *76*, 3373.

(56) Folch, A.; Toner, M. *Annu. Rev. Biomed. Eng.* **2000**, *2*, 227.

(57) Tourovskaia, A.; Barber, T.; Wickes, B. T.; Hirdes, D.; Grin, B.; Castner, D. G.; Healy, K. E.; Folch, A. *Langmuir* **2003**, *19*, 4754.

(58) Shah, S. S.; Lee, J. Y.; Verkhoturov, S.; Tuleuova, N.; Schweikert, E. A.; Ramanculov, E.; Revzin, A. *Langmuir* **2008**, *24*, 6837.

(59) VanStipdonk, M. J.; Schweikert, E. A. *Nuclear Instruments & Methods in Physics Research Section B-Beam Interactions with Materilas and Atoms* **1996**, *112*, 68.

(60) Li, Z.; Verkhoturov, S. V.; Locklear, J. E.; Schweikert, E. A. *International Journal of Mass Spectrometry* **2008**, *269*, 112.

(61) Hainfeld, J. F.; Furuya, F. R. *J. Histochem. Cytochem.* **1992**, *40*, 177.

(62) Liang, C. H.; Wang, C. C.; Lin, Y. C.; Chen, C. H.; Wong, C. H.; Wu, C. Y. *Anal Chem* **2009**, *81*, 7750.

(63) Depanfilis, G.; Manara, G. C.; Ferrari, C.; Torresani, C. *J Invest Dermatol* **1988**, *91*, 547.

(64) Wang, S. T.; Chen, K. J.; Wu, T. H.; Wang, H.; Lin, W. Y.; Ohashi, M.; Chiou, P. Y.; Tseng, H. R. *Angew Chem Int Edit* **2010**, *49*, 3777.

(65) Depanfilis, G.; Soligo, D.; Manara, G. C.; Ferrari, C.; Torresani, C. *J Invest Dermatol* **1989**, *93*, 60.

(66) Cho, E. C.; Liu, Y.; Xia, Y. A. *Angew Chem Int Edit* **2010**, *49*, 1976.

(67) Das, R.; Jagannathan, R.; Sharan, C.; Kumar, U.; Poddar, P. *J Phys Chem C* **2009**, *113*, 21493.

(68) Cho, E. C.; Au, L.; Zhang, Q.; Xio, Y. *Small* **2010**, *6*, 517.

(69) Wang, S. F.; Zhang, X.; Mao, X.; Zeng, Q. X.; Xu, H.; Lin, Y. H.; Chen, W.; Liu, G. D. *Nanotechnology* **2008**, *19*.

(70) Wu, H.; Liu, G. D.; Wang, J.; Lin, Y. H. *Electrochem Commun* **2007**, *9*, 1573.

(71) Jokerst, J. V.; Floriano, P. N.; Christodoulides, N.; Simmons, G. W.; McDevitt, J. T. *Lab Chip* **2008**, *8*, 2079.

(72) Hager-Braun, C.; Tomer, K. B. *Biochemistry-Us* **2002**, *41*, 1759.

(73) Crise, B.; Rose, J. K. *Journal of Biological Chemistry* **1992**, *267*, 13593.

(74) Wang, J. H.; Yan, Y. W.; Garrett, T. P. J.; Liu, J. H.; Rodgers, D. W.; Garlick, R. L.; Tarr, G. E.; Husain, Y.; Reinherz, E. L.; Harrison, S. C. *Nature* **1990**, *348*, 411.

(75) Zhang, H. D.; Williams, P. S.; Zborowski, M.; Chalmers, J. J. *Biotechnology and Bioengineering* **2006**, *95*, 812.

(76) Sekine, K.; Revzin, A.; Tompkins, R. G.; Toner, M. *J Immunol Methods* **2006**, *313*, 96.

(77) Zhu, H.; Macal, M.; Jones, C. N.; George, M. D.; Dandekar, S.; Revzin, A. *Anal Chim Acta* **2008**, *608*, 186.

(78) Shah, S. S.; Howland, M. C.; Chen, L. J.; Silangcruz, J.; Verkhoturov, S. V.; Schweikert, E. A.; Parikh, A. N.; Revzin, A. *Acs Applied Materials & Interfaces* **2009**, *1*, 2592.

(79) Zhu, H.; Stybayeva, G.; Silangcruz, J.; Yan, J.; Ramanculov, E.; Dandekar, S.; George, M. D.; Revzin, A. *Analytical Chemistry* **2009**, *81*, 8150.

(80) Davis, K. A.; Abrams, B.; Iyer, S. B.; Hoffman, R. A.; Bishop, J. E. *Cytometry* **1998**, *33*, 197.

(81) Wang, L.; Abbasi, F.; Gaigalas, A. K.; Hoffman, R. A.; Flagler, D.; Marti, G. E. *Cytom Part B-Clin Cy* **2007**, *72B*, 442.

(82) Osterfeld, S. J.; Yu, H.; Gaster, R. S.; Caramuta, S.; Xu, L.; Han, S. J.; Hall, D. A.; Wilson, R. J.; Sun, S. H.; White, R. L.; Davis, R. W.; Pourmand, N.; Wang, S. X. *P Natl Acad Sci USA* **2008**, *105*, 20637.

(83) Gunnarsson, A.; Sjovall, P.; Hook, F. *Nano Letters* **2010**, *10*, 732.

(84) Tiefenauer, L.; Ros, R. *Colloid Surf. B-Biointerfaces* **2002**, *23*, 95.

(85) Pei, R. J.; Cheng, Z. L.; Wang, E. K.; Yang, X. R. *Biosens Bioelectron* **2001**, *16*, 355.

(86) Afonso, C.; Fenselau, C. *Anal Chem* **2003**, *75*, 694.

(87) Dubey, M.; Emoto, K.; Takahashi, H.; Castner, D. G.; Grainger, D. W. *Advanced Functional Materials* **2009**, *19*, 3046.

(88) Dubey, M.; Emoto, K.; Cheng, F.; Gamble, L. J.; Takahashi, H.; Grainger, D. W.; Castner, D. G. *Surface and Interface Analysis* **2009**, *41*, 645.

(89) Revzin, A.; Tompkins, R. G.; Toner, M. *Langmuir* **2003**, *19*, 9855.

(90) Lee, J. Y.; Shah, S. S.; Yan, J.; Howland, M. C.; Parikh, A. N.; Pan, T. R.; Revzin, A. *Langmuir* **2009**, *25*, 3880.

(91) Lee, K. B.; Jung, Y. H.; Lee, Z. W.; Kim, S.; Choi, I. S. *Biomaterials* **2007**, *28*, 5594.

(92) Rickman, R. D.; Verkhoturov, S. V.; Parilis, E. S.; Schweikert, E. A. *Physical Review Letters* **2004**, *92*.

(93) Hermanson, G. T. *Bioconjugate techniques*; 2nd ed.; Elsevier Academic Press: Amsterdam ; Boston, 2008.

(94) Eller, M. J.; Verkhoturov, S. V.; Della-Negra, S.; Rickman, R. D.; Schweikert, E. A. *Surface and Interface Analysis* **2011**, *43*, 484.

(95) Ray, K. B.; Park, M. A.; Schweikert, E. A. *Nucl Instrum Meth B* **1993**, *82*, 317.

APPENDIX

EXAMINATION AND QUANTIFICATION OF MICROSTRIPS

Introduction

Photoresists (PR) have been extensively used in the micro-lithographic fabrication to create patterned surfaces with wide applications in semiconductors, microarrays, and electronics. PR, a photosensitive polymer, is composed of the m/p-cresol novolak resin.[1] A remaining challenge of PR lithographic approach is to fabricate small width of microstrips without the occurrence of the PR residual tails in the transition area between PR strips. The PR residue can inhibit the immobilization of biomolecules and proteins on the desired surfaces. Thus, a high sensitive analytical tool at molecular level is needed for the characterization of micropatterns.

The profilometer and scanning electron microscope (SEM) have been used to determine the topography and shape of microstrips. However, these analyses cannot provide detailed chemical information for the PR residue in the transition area between the PR and the silicon (Si) wafer substrate at the nanometric level.

We examine here the performance of microstrips by using cluster ToF-SIMS with the event-by-event bombardment/detection mode to quantify the fractional surface coverage of PR and Si strips respectively. By analyzing the secondary ion (SI) co-emissions originating from the PR and Si and utilizing the quantitative methodology as

described in Chapter II, it allows for the determination of nanometrically thin PR tails remaining in the transition areas.

Our hypothesis is that the number of coincidental impacts should be correlated with the length of the PR tail with a thickness less than 10nm. A comparison of the number of effective impacts on the PR and Si should allow for the quality-control of the microstrips. The correlation of the length of the tails and the height of the strips with different etching procedures is described below.

Experimental section

a. Preparation of PR microstrip patterns

Micrometer size PR strips were fabricated on a Si wafer with thickness of ~1 and 4 μm and width of 500, 100 and 50 μm. To perform microstrips pattern with thickness of ~ 5 μm and width of 500 μm, the slide was placed under a film mask printed with 500 μm symmetrical microstrips. Then 3 droplets of photoresists (SC 1827, MicropositTM SCTM) were added on the top of a pure Si wafer (1in x 1 in). The chip was placed on spin coater at speed of 2000 rpm for 2 mins. The slide was baked at temperature of 90 □ for 1 min and followed by a second baking at 120 □ for 2 mins. After the chip is cooled down to atmospheric temperature, the mask was aligned and exposed to a UV lamp (440W, wavelength: 200 nm) for 30 s. Then PR pattern were developed with commercial developer (MicropositTM MFTM-321) and rinsed with distilled water. Different thickness of PR microstrips films were prepared by changing the amount of PR, the spin coating speed, and the baking period. Negative ions originate from PR which is composed of m/p-cresol novolak resin were observed in the secondary ion mass spectra.

Results and Discussion

a. Examination of microstrips using C_{60}^{+}-ToF SIMS

The area bombarded with primary ions was ~ 0.5 to 0.8 mm in diameter. The data from the PR strips with widths of 500, 100, and 50 μm to ensure are shown in Figure 1. The negative ion spectrum (Figure 1(a)) shows that the distinct negative ions of PR are F^- at m/z = 19, $CH_2C_6H_4OH^-$ at m/z =107, $CH_2CH_3C_6H_3OH^-$ at m/z =121, and $C_{15}H_{13}(OH)_2^-$ at m/z =227. Figure 1(b) shows the characteristic ions of Si wafer as SiO_2OH^- at m/z =77, $(SiO_2)_2H^-$ at m/z =121, and $(SiO_2)_2OH^-$ at m/z =137. Figure 2 shows the optical image of symmetrical micropattern of PR on a supporting Si wafer with width of 100 μm. Also, distinct peaks of microstrips from both PR and Si were observed in Figure 1(c). As noted earlier, the co-emitted SIs originating from individual Si and PR strips, and co-localized PR and Si molecules at the nanometric level allows for the calculation of the surface fractional coverage and the identification of remaining PR in the transition area.

b. Correlation Coefficients

Figure 3 presents the correlation coefficients (Q) of selected ions at various thicknesses and widths. $CI_{77(Si),137(Si)}$ represents that ions at m/z =77 are co-emitted simultaneously with ions at m/z =137. The results show that the correlation coefficients ($Q_{77,\,137}$) from Si wafer are about 2 at the test case of widths in 500, 100 and 50 μm. The explanation of the two times large coefficient in this test case is below. The projectiles sent to stochastically bombard the microstrip surface impact on one half of PR and Si. Thus, the experimental number of primary impacts (N_e) on PR and Si wafer is only one

half of the total number of projectile impacts (N_0) sent to bombard on the microstrips. When the total number of projectile impacts is applied to the N_e in the Eq. II-12 as described in Chapter II, there is a two times overestimation for the effective number of projectile impacts in the equation. Consequently, the correlation coefficient $Q_{77,\ 137}$ of symmetrical patterned microstrips is equal to 2 while the emissions of ions 77 (SiO_2OH^- and 137 $(SiO_2)_2OH^-$ are uncorrelated. A further analysis of co-emitted ions at m/z =19 (F^-) and 227 ($C_{15}H_{13}(OH)_2^-$) from PR is done as shown in Figure 5. Compared to $Q_{77,\ 137}$ of ~2, the $Q_{19,\ 227}$ for PR is small than 2 and the values vary with different widths. The explanation is that the small abundance of remaining PR in the transition area can influence the effective number of impacts. Various widths of microstirp samples result in different Q values for PR, which is attributed to different extent of remaining PR on the microstrip surfaces. Also, consistent Q values were observed for the flat Si wafer surface. In which, less topographic variation and extremely thin layer (< 10nm) of remaining PR create consistent emissions of Si related SI that contributes to the consistency of surface fractional coverage of Si wafer substrate as described below.

c. Effective Number of Impacts and fractional coverage of PR or Si

The first test case to calculate the effective number of impacts was carried out with symmetrical microstrips. Our assumption was that N_e on PR should be similar to Si. The quantitative methodology (Eq. II-16 in Chapter II) is used to examine the fractional coverage and the presence of PR in the transition area between Si wafer and PR strips with a nanovolumetric sensitivity. Figure 4 shows the values of PR fractional coverage are larger than that of Si in the test cases of 4.6 μm thick microstrips. But for the test

case of 0.9 and 0.4 μm thick PR, the PR defects lead to a larger effective number of impacts on Si. An interesting result is that the values of fractional coverage for Si wafer are consistent in each test case. It demonstrates that the flat Si substrate and thin PR layer results in similar numbers of effective impacts on Si. Also, the PR tail in the transition area and the presence of defects leads to inconsistent surface coverage of PR with different widths and thicknesses.

Figures 5 show the profilometer results of microstrips. In the test case of 500 μm, wide microstrips result in a better cut-off edge of microstrips. Compared to the calculated fractional coverage of microstrips, ~62% of the entire surface is covered with PR while ~49% of the entire surface is covered by Si supported substrate. The total surface fractional coverage of PR and Si larger than 100% is attributed to the thin layer of PR remaining on the surface. It also demonstrates that the thickness of PR retention tail is small enough (<10nm) for the projectile impact and SI emission process that contributes to the SI coemissions originating from the co-localized PR and Si molecules. Figure 5(a) shows the morphology of 500 μm microstrips characterized by profilometer. The rectangular grooves depth is ~4.6 μm and the distance between grooves is ~500 μm. The non-perfect rectangular morphology fits the calculated fractional coverage. Figure 5(b) and (C) show the morphologies of 100 μm and 50 μm wide microstrips are triangular grooves. Compared to 500 μm microstrips, narrower microstrips represent a triangular surface that is attributed to the remaining PR tails in the transition area. The profilometry results are also in agreement with the calculated fractional coverage results. For test cases of 100 and 50μm, PR are of 70% and 82% while Si are of 37% and 52%

respectively. Also, the smaller width of groove gaps than expected size was observed in Figure 5(b) which fits the calculated fraction coverage: ~37% of the entire surface is covered with Si. It also concludes that the etching process did not completely remove PR that causes a portion of the Si wafer is hidden under the PR film (>10nm thick). In the test case of 50 μm, almost 30% of thin PR layer (<10 nm thick) overlaps with the Si wafer in the transition area that results in an 82% PR coverage of entire surface.

Conclusion

We validate the feasibility of using the cluster C_{60}^{+}-SIMS operated in the event-by-event bombardment/detection mode to: a) quantify the fractional surface coverage of PR microstips and Si substrate, b) examine the fabrication quality of PR microstrips on the Si supported substrate. The extent of the PR residuals to different width and thickness relying on different etching procedures was evaluation with the correlation coefficients and the developed methodology. The quantitative approach is a high surface sensitive analysis and simultaneously provides chemical information compared to other analyses by using microscope and profilometer.

REFERENCE (APPENDIX)

(1) Bogan, L. E. *Polymeric Materials Encyclopedia* CRC Press, 1996; Vol. 6(M-O).

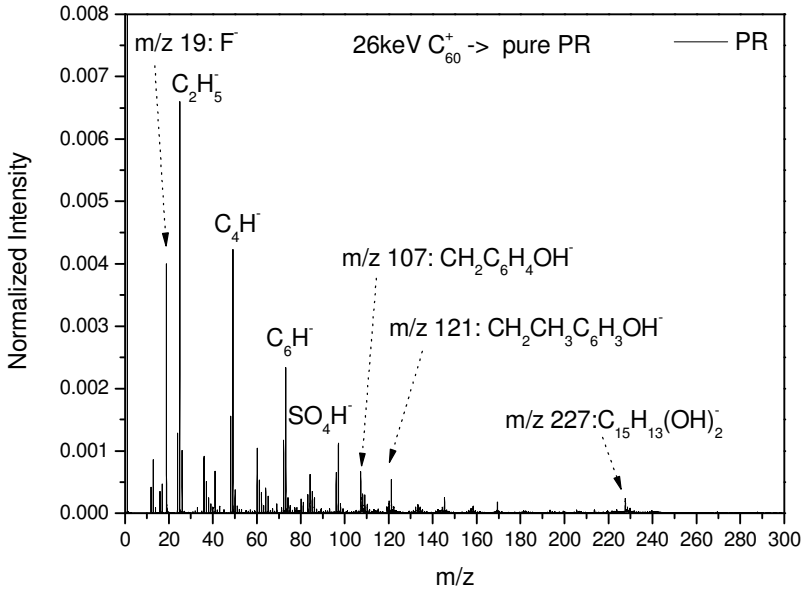

Figure 1 (a)

Figure 1 Negative ion mass spectra of pure PR (a), pure Si wafer (b), and PR microstrips with width of 100μm on Si wafer substrate (C).

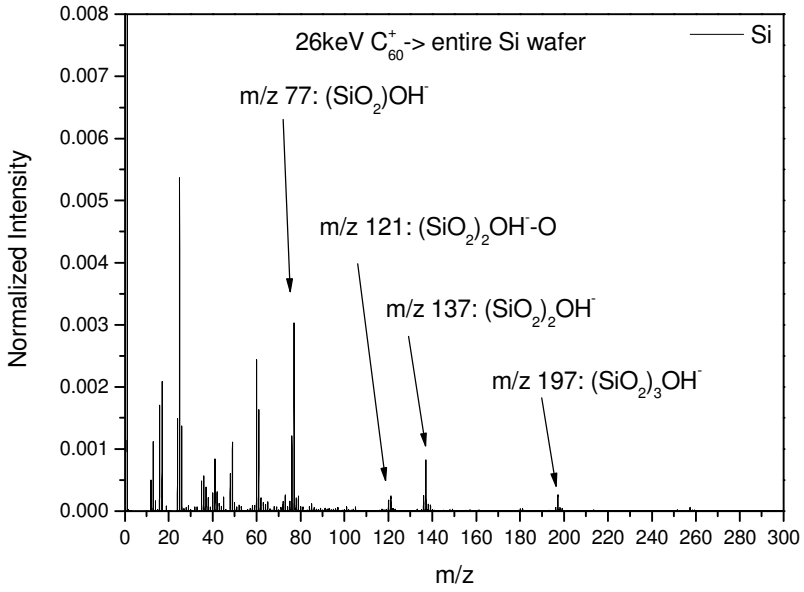

Figure 1 (b)

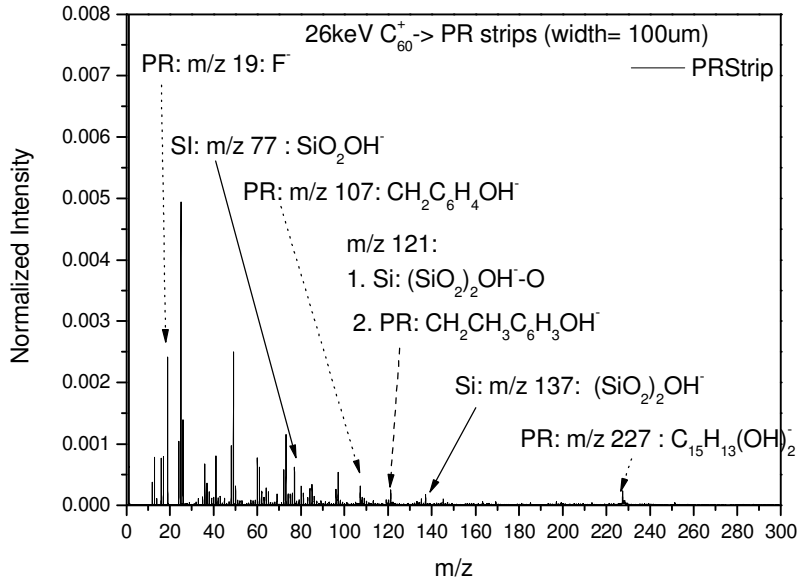

Figure 1 (c)

Figure 1 Continued

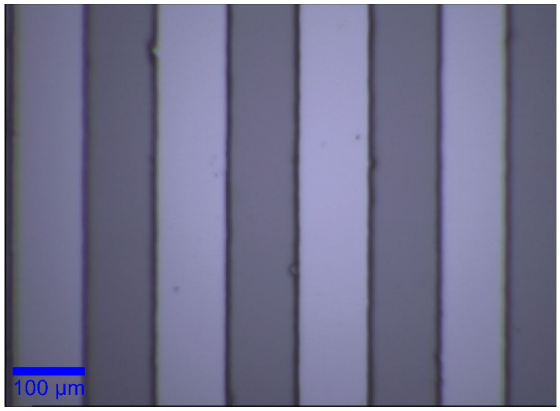

Figure 2 Optical imaging of PR microstrips on supported Si wafer with width of 100µm.

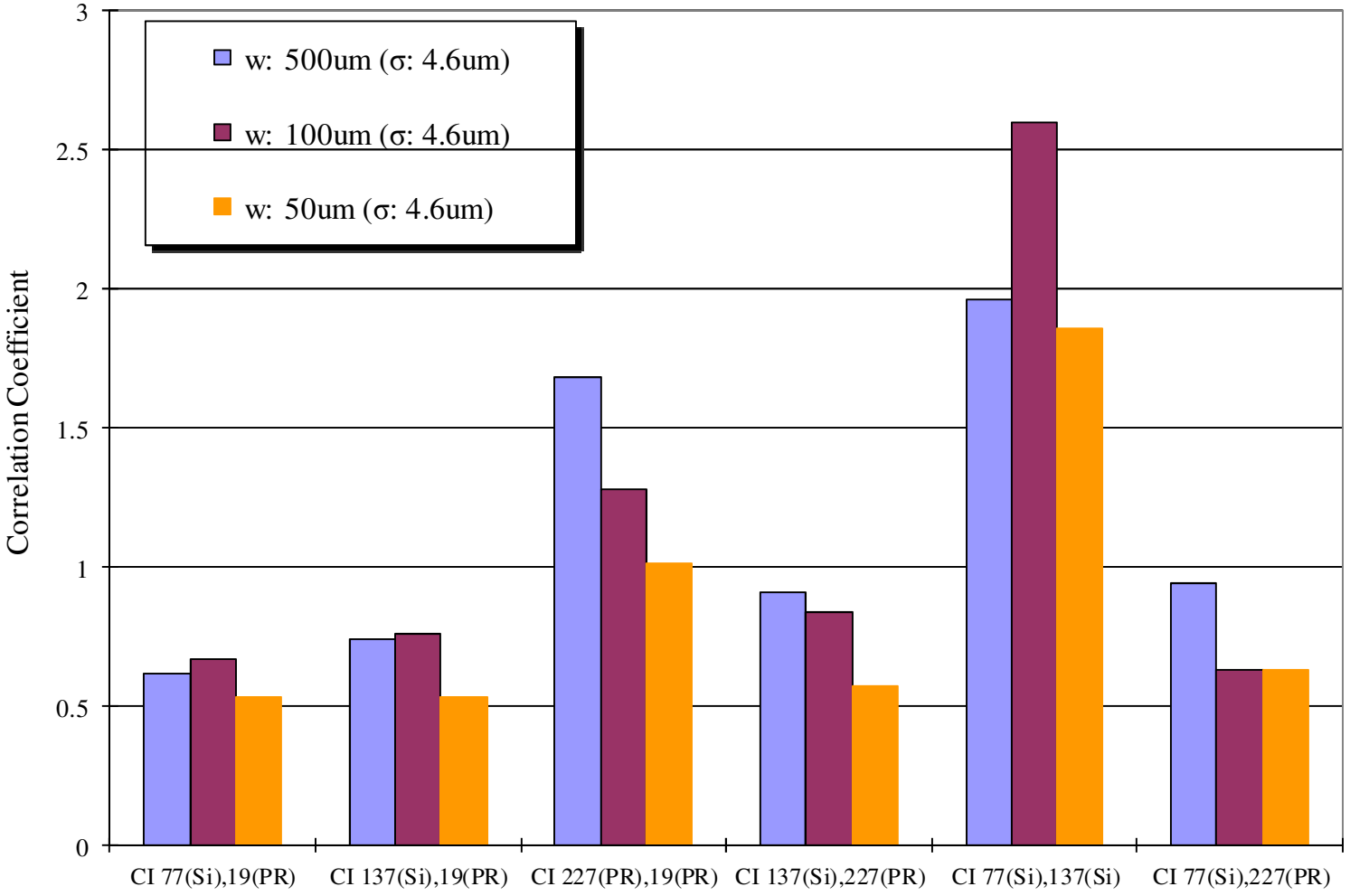

Figure 3 The correlation coefficients for the coincidental ions at m/z = 19 and 227 from PR and at m/z =77 and 137 from Si.

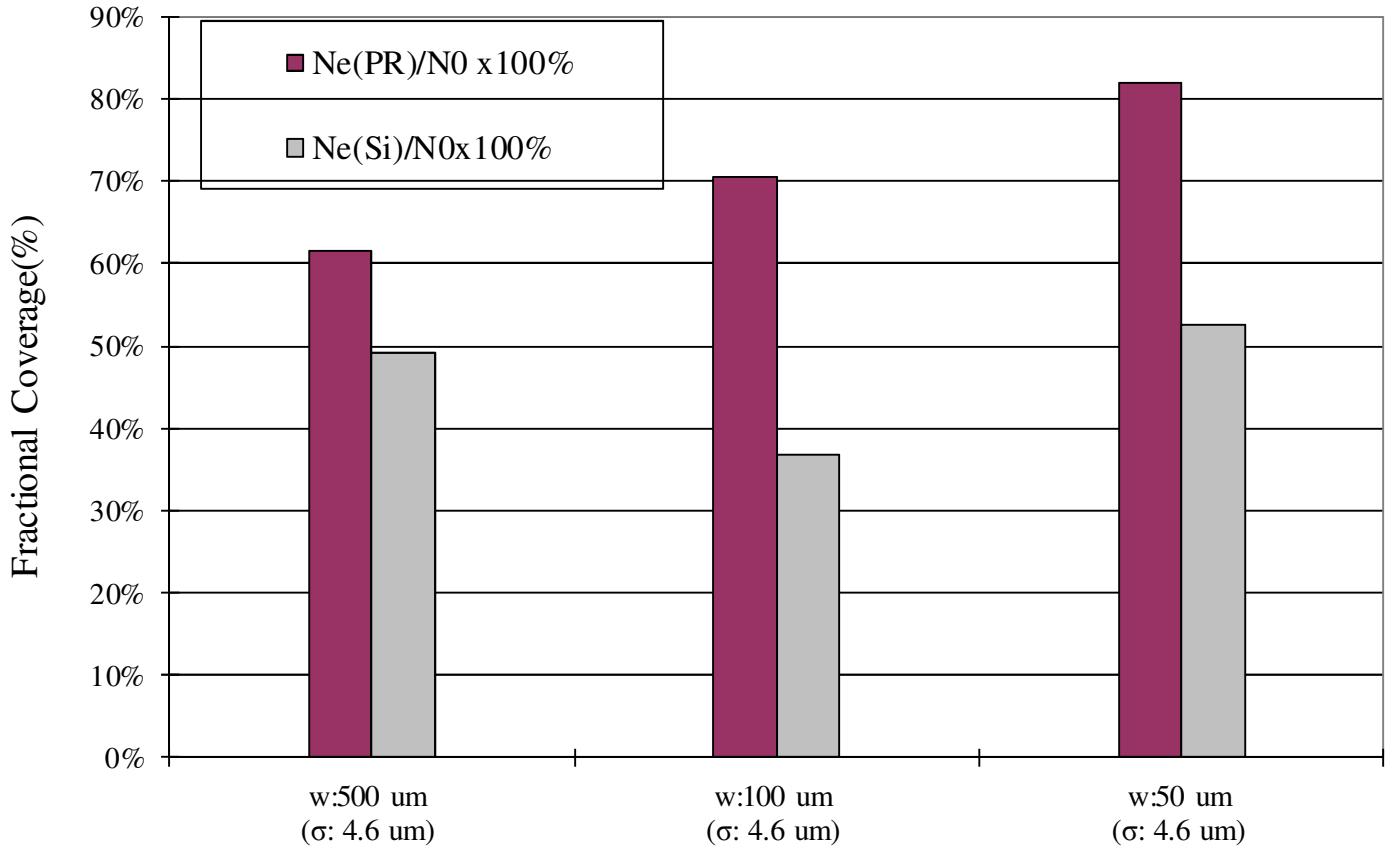

Figure 4 The fractional coverage of PR and Si on the micro-strip surface with different widths.

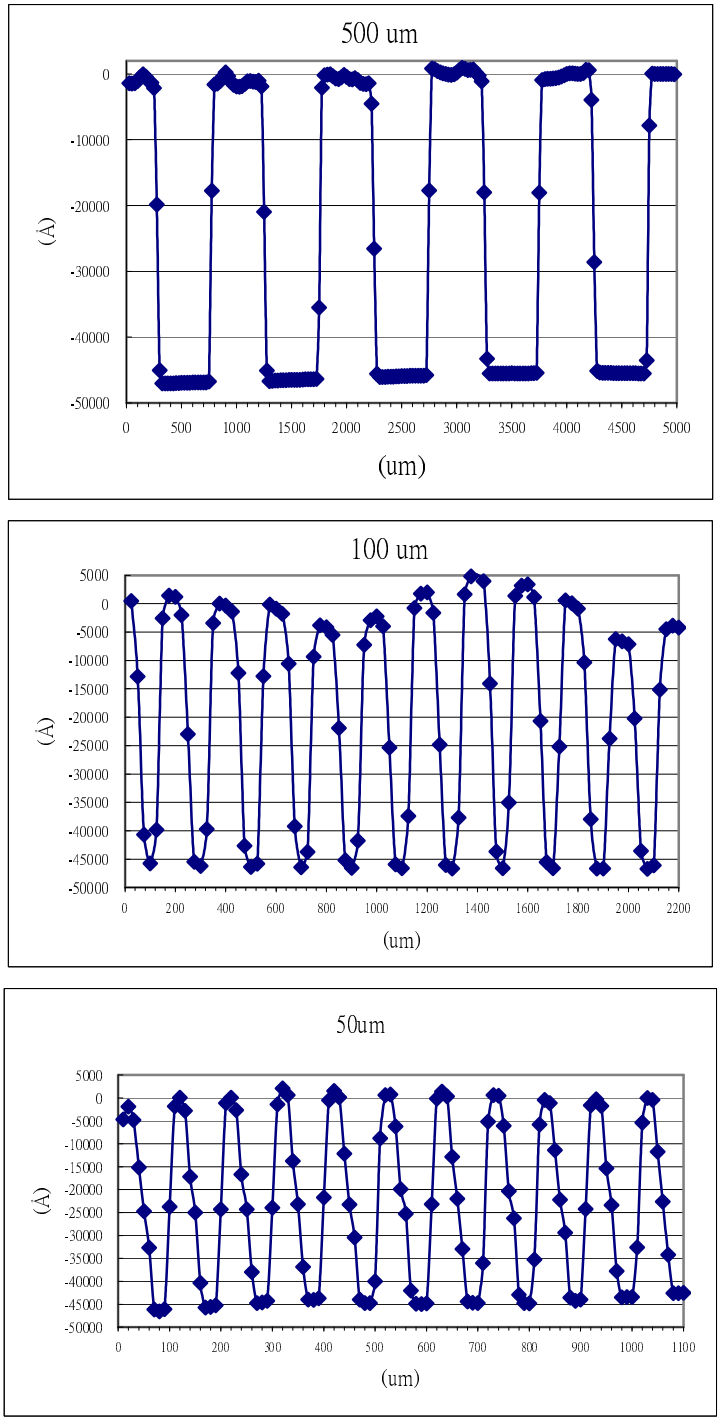

Figure 5 The profilometry results of microstirps.

VITA

Li-Jung Chen received her Bachelor of Science degree in applied chemistry from National Chiao Tung University (Hsinchu, Taiwan) in June, 2002. She enrolled in the Department of Chemical Engineering at National Tsing Hua University in September 2002 and received her Master's degree in June 2004. The title of her master's thesis is "The synthesis of palladium nanoparticle in ethylene glycol system under room temperature and its applications to electroless copper deposition". In September of 2006, she enrolled in the Department of Chemistry at Texas A&M University to pursue a Ph.D. degree. In November of 2006, she joined Dr. Emile A. Schweikert's laboratory at Texas A&M University. Ms. Chen may be reached at: lijung.chen@gmail.com. The departmental address is: Department of Chemistry, Texas A&M University, PO Box 20012, College Station, TX 77842-3012.